Computational Modeling and Control for Personalized Neuroprosthetics and Rehabilitation

Mitsuhiro Hayashibe

ACADÉMIE DE MONTPELLIER

UNIVERSITÉ DE MONTPELLIER

- SCIENCES ET TECHNIQUES DU LANGUEDOC -

École Doctorale : Information, Structures et Systèmes
Spécialité : SYstèmes Automatiques et Microélectronique

Habilitation à Diriger des Recherches

présentée et soutenue publiquement par

Mitsuhiro Hayashibe

le 12 Octobre 2015

Computational Modeling and Control for Personalized Neuroprosthetics and Rehabilitation

JURY :

Franck Multon	Professeur, Univ. Rennes 2, IRISA - Rennes	Rapporteur
Agnès Roby-Brami	Directrice de Recherche, INSERM, ISIR - Paris	Rapporteur
Auke Ijspeert	Professeur, EPFL, Biorobotics Laboratory - Switzerland	Rapporteur
Philippe Souères	Directeur de Recherche, CNRS, LAAS - Toulouse	Examinateur
Philippe Fraisse	Professeur, Univ. Montpellier, LIRMM - Montpellier	Examinateur
Stéphane Perrery	Professeur, Univ. Montpellier, M2H - Montpellier	Examinateur
David Guiraud	Directeur de Recherche, INRIA, LIRMM - Montpellier	Examinateur

CONTENTS

Curriculum Vitae

0.1 Personal Data

NAME:	Mitsuhiro Hayashibe
PLACE AND DATE OF BIRTH:	Nagano, Japan | 24 March 1977
WORK ADDRESS:	860 Rue Saint Priest - 34095 Montpellier, France
PHONE:	+33 (0)4 67 41 85 22
EMAIL:	hayashibe@lirmm.fr
WEB:	`http://www.lirmm.fr/~hayashibe/`

0.2 Work Experience

Current JAN 2012	Research Scientist (permanent, CR 1st class) INRIA Sophia-Antipolis DEMAR team and LIRMM, Universite dé Montpellier
SEP 2008-DEC 2011	Research Scientist (permanent, CR 2nd class) INRIA Sophia-Antipolis DEMAR team and LIRMM, Universite dé Montpellier
JAN 2007-AUG 2008	Postdoctral Fellow INRIA Sophia-Antipolis DEMAR team and LIRMM, Universite dé Montpellier
APR 2001-JUN 2006	Assistant Professor Jikei University School of Medicine, Department of Medicine, Research Center for Medical Sciences, Tokyo, Japan

0.3 Diplomas

MAR 2005	Ph.D. - Industrial Mechanical Engineering, **University of Tokyo** Advisor: Prof. Mamoru Mitsuishi and Prof. Yoshihiko Nakamura
MAR 2001	M.Sc. Engineering - Mechano-Informatics, **University of Tokyo** Advisor: Prof. Yoshihiko Nakamura
MAR 1999	B.Sc. Engineering - Mechano-Aerospace, **Tokyo Institute of Technology**

0.4 Awards and Fellowships

APR 2008	JSPS Postdoctoral Fellowship for Research Abroad (declined for tenured position)
NOV 2005	CAS Young Investigator Award, Gold Prize (Hitachi Medical Systems Award) " Intraoperative navigation system with volume data of mobile C-arm CT"
NOV 2005	Best Paper Award, Journal of Japanese Society for Computer-aided Surgery, "Development of Data Fusion System for Robotics Surgery (da Vinci)"
OCT 2005	Good Design Award 2005 prize in the category of the new frontier design, Designer for High-Tech Navigation Operating Room `http://www.g-mark.org/award/describe/31858?token=HJehsZSdvw` (certified by JIDPO (Japan Industrial Design Promotion Organization)
JAN 2003	MMVR (Medicine Meets Virtual Reality) Conference Best Poster Award

0.5 Qualification

- Class I Information Technology Engineer
  (Authorized by IPA Information-Technology Promotion Agency, Japan)
- Pre-1st Grade of the STEP Test in Practical English Proficiency (Authorized by the Japanese Ministry of Education, Culture, Sports, Science and Technology)
- EIT (Engineer In Training Authorized by National Society of Professional Engineers(Oregon State, USA)

0.6 Patent

- Registered: JP,4148763,B (JP,2004-180781,A) Endoscopic Surgery Robot
  (Apply 2002.11.29)(Opening 2004.7.2)(Registration 2008.7.4) N. Suzuki, S. Suzuki, **M. Hayashibe**, Y. Otake, A. Hattori
- Opened: (JP,2006-158722,A) Artificial Femoral Head for Measuring Pressure Distribution, Measuring Instrument, and Intraoperative Evaluation Method of Artificial Joint Installation Situation
  (Apply 2004.12.08)(Opening 2006.6.22) N. Suzuki, Y. Otake, A. Hattori, **M. Hayashibe**, S. Suzuki, N. Sugano, H. Miki, Z. Yamamura, S. Yonenobu, T. Ochi
- Opened: (JP,2004-186824,A) Time-Spatial Multiplex Image Apparatus and Method Therefor
  (Apply 2002.11.29)(Opening 2004.7.2) N. Suzuki, S. Suzuki, **M. Hayashibe**, Y. Otake, A. Hattori

Scientific Responsibilities (2010-)

- Editor
  - Guest Associate Editor, Frontiers in Neuroscience, Biosignal processing and computational methods to enhance sensory motor neuroprosthetics with David Guiraud, Dario Farina, and Jose L. Pons
    This special issue was recently closed (19papers 101 authors, 59,581 Views as of 30th Sep. 2015)
  - Editorial Board of the International Journal of Advanced Robotic Systems (IF=0.82), Rehabilitation Robotics
- Program committe and organizer
  - IEEE BIOROB2010 Exective program committe and associate editor
  - France-Japan Meeting on Technologies for Helping People with Physical Disabilities, Thursday, September 30th, 2010, Embassy of France in Japan, Tokyo. Moderator
  - ICIRA2011 Program committee
  - Organizer for Workshop on Robotics for Neurology and Rehabilitation, September 30th, 2011, IEEE IROS, San Francisco, California
  - Organizer for Workshop on Human Motion Modeling and Human-inspired Motor Control together with Philippe Fraisse, Emel Demircan, Oussama Khatib (Stanford Univ.) at IEEE HUMANOIDS 2014, Madrid, Spain.
  - Co-Chair of **IEEE Technical Committee on Human Movement Understanding** at Robotics and Automation Society with E. Demircan (Univ. of Tokyo), D. Kulic (Univ. of Waterloo) and D. Oetomo (Univ. of Melbourne). https://sites.google.com/site/ieeehmu/
- Collaborative Technical Experience
  - Visiting Researcher at RIKEN Brain Science Institute - TOYOTA Collaboration Center (2012-present)
  - Member of SimTK Projects (Simbios, the National NIH Center for Biomedical Computing focusing on Physics-based Simulation of Biological Structures) https://simtk.org/home/fes
- Research projects (Contrats de recherche)
  - Inria Project-Lab: BCI-LIFT (Brain Computer Interfaces: Learning, Interaction, Feedback, Training) 2015-2018
  - Coordinator of STIC-South America scientific-technological cooperation program 2012-2013 with UnB (University of Brasilia) and PCUP (Pontifical Catholic University of Peru) CARAT Computer-Aided Rehabilitation Algorithms and Toolsfor Telerehabilitation
  - ANR french national project SoHuSim for modeling and simulation of soft interaction between humans and objects (2011-2014) in charge of partner organization

- Collaborative project with Robotics Lab, Stanford Univ. (visit on April 2010) in @WALK (ArTificial WALKing) Project (2010-2012) supported by INRIA
- French side leader of Japan-France Integrated Action Program " SAKURA and AYAME Junior" supported by JSPS and INRIA 2010-2011 Modele Neuromusculaire du Corps Humain et ses Applications pour la Rehabilitation par la Stimulation Electrique Fonctionnelle"
- 2 PhD grants from China Scholarship Council (CSC) (2009,2011)
- 1 PhD grant from CNRS handicap (2011)
- 1 PhD grant from EU INRIA CORDIS program (2011)

Academic Supervision and Teaching

- Doctorate level
  - Qin Zhang (PhD, University of Montpellier II) 2009.1-2011.12
    (accepted for JSPS postdoc program, since 1.1.2013 Associate Professor at Huazhong University of Science and Technology)
    " Evoked EMG-based torque prediction for muscle fatigue tracking and closed-loop torque control in FES"
    3 journal papers published, including 2 IEEE Transactions
    Advisors : M. Hayashibe (Principal), P. Fraisse
    (supported by China Scholarship Council (CSC))
  - Zhan Li (PhD, University of Montpellier II) 2011.10- 2014.12
    (since 1.3.2015 Assistant Professor at University of Electronic Science and Technology of China)
    " Real-time EMG-Feedback Torque Prediction and Muscle Activation Control toward New Modality in FES"
    2 journal papers published, including 1 IEEE Journal and 1 IEEE Magazine, one submitted for IEEE Transaction
    Advisors : M. Hayashibe (Principal), D. Guiraud
    (supported by China Scholarship Council (CSC))
  - Alejandro Gonzalez (PhD, University of Montpellier II) 2011.10- 2014.12
    (since 1.9.2015 Temporary Professor at Univ. of Montpellier, Euromov)
    "Versatile whole body center of mass identification for balance assessment in home rehabilitation"
    3 journal papers published, including 1 IEEE Journal
    Advisors : M. Hayashibe (Principal), P. Fraisse
    (supported by European Comission: INRIA-CORDIS)
  - Yacin Berranen (PhD, University of Montpellier II) 2011.10- present
    "Volumetric musculoskeletal modeling and simulation"
    1 journal paper to submit soon
    Advisors : M. Hayashibe (40 %), B.Gilles, D. Guiraud
    (supported by CNRS Handicap grant)
- Partial Participation in Supervision
  - Saugat Bhattacharyya (PhD internship) 2014.10- 2015.6
    " Study on Probabilistic nature of Motor Imagery Electroencephalography signals for control"
    (Svaagata.eu: experience Europe as an Indian Erasmus Mundus, Jadavpur University, Kolkata, India)
    PhD defense in Aug. 2015, to be continued with INRIA BCI-LIFT program
    Advisor : D.N. Tibarewala
  - Roberto Baptista (PhD internship) 2014.5- 2015.4
    " Framework for Automatic Assessment of Human Motion for Rehabilitation"
    (PhD internship bourse d'etudes du Gouvernement Bresilien, Fondation Capes, Universidade de Brasilia (UnB), Brasil) on-going study to defense in 2016
    Advisor : Antonio Bo

- Sourav Chandra (PhD internship) 2013.9- 2014.2
  "Dynamic modeling of fatigue induced hand tremor"
  (Svaagata.eu: experience Europe as an Indian Erasmus Mundus, Indian Institute of Technology Madras, India) on-going study to defense in 2016
  Advisor : T. Asokan
- Maria Papaiordanidou (PhD, Oct 2010, University of Montpellier I, EDM UFR STAPS, France)
  " Nature peripherique et centrale de la fatigue musculaire"
  (Since 2010.10, Maitre de conference at Aix-Marseille Universite (Assistant Professor)) Advisor : D. Guiraud, A. Varray
- Mourad Benoussaad (PhD, Dec 2009, University of Montpellier II, Department of Robotics LIRMM, France)
  " Identification protocol under FES and stimulation patterns synthesis for rehabilitation in spinal cord injured subject"
  (accepted for JSPS postdoc program, since 2014.9, Maitre de conference at l'Ecole Nationale d'Ingénieurs de Tarbes (Assistant Professor)) Advisor : P. Poignet, D. Guiraud

- Master level (only listing full stage basis, projet work is not counted)
  - Yacine Berranen, Master2 (University of Montpellier II, EEA, France)
    " Analyse des déformations de tissus mous actifs et passifs", 2011.3-7 Encadrement : M. Hayashibe, B. Gilles
  - Lizhi Pan (INRIA Master Internship, Shanghai Jiao Tong University)
    " Multi-functional EMG classification and control of muscle model", 2011.9-11 Encadrement : M. Hayashibe
  - Peng Yao (INRIA Master Internship, Shanghai Jiao Tong University)
    " Rehabilitation technology for patients with pathological tremor", 2011.9-11 Encadrement : M. Hayashibe
  - Yacine Berranen, Master1 (University of Montpellier II, EEA, France)
    " Modelisation du muscle electriquement stimule pour le calcul en ligne", 2010.4-7 Encadrement : M. Hayashibe
  - Floor Campfens, (ERASMUS Master Internship, University of Twente, Netherlands)
    " An Activation Model of Motor Response and H-Reflex under FES", 2008.2-6 Encadrement : M. Hayashibe, D. Guiraud

- Annual Teaching
  - I am responsible as a Master course coordinator, at University of Montpellier, Joint Module of Master STIC pour la Sante (http://www.tecsan.univ-montp2.fr/), PhyMed (http://www.phymed.fr/) and Institute Neuroscience Montpellier (http://www.inmfrance.com/inm/en/) , for Neuroprotheses I (Basic Neurophysiology, 50h) and II (NeuroRehabilitation, 50h) (2015)

- I am organizing the module“ NeuroprothesesI ”and“ NeuroprothesesII ”which are M1 and M2 course to teach the biosignal processing and its application for advanced Neuroprosthetics. (2012, 2013, 2014)
- I am organizing the module “ Modele et Regulation ” which is M2 1st semester course to teach the modeling, identification and control in biomechanics and neuroprosthetics. (2012, 2013, 2014)
- I make a lecture course for Univ. of Montpellier, Master STIC pour la Sante, (NeuroprothesesII), “ EMG and EEG signal processing and its use for rehabilitation ” (6h) (9 HTD) (2012, 2013, 2014)
- I make a lecture course for Univ. of Montpellier, Master STIC pour la Sante, (Modele et Regulation) “ Identification and Control in Biomechanics“ (6h) (9 HTD) (2012, 2013, 2014)

List of Journal Publications (since 2008)

- E. Demircan, D. Kulic, D. Oetomo, M. Hayashibe, " Human Movement Understanding", IEEE Robotics and Automation Magazine, vol.22, no.3, pp.22-24, 2015.

- A. Gonzalez, P. Fraisse, M. Hayashibe, " Adaptive Interface for Personalized Center of Mass Self-identification in Home Rehabilitation", IEEE Sensors Journal, vol.15, no.5, pp.2814-2823, 2015. (Chap.6)

- Z. Li, D. Guiraud, M. Hayashibe, " Inverse Estimation of Multiple Muscle Activations from Joint Moment with Muscle Synergy Extraction", IEEE Journal of Biomedical and Health Informatics, vol.19, no.1, pp.64-73, 2015. (Chap.5)

- M. Benoussaad, P. Poignet, M. Hayashibe, C. Azevedo-Coste, C. Fattal, D. Guiraud, " Synthesis of Optimal Electrical Stimulation Patterns for Functional Motion Restoration Applied to Spinal Cord Injured Patients", Medical & Biological Engineering & Computing, vol.53, pp.227-240, 2015.

- V. Bonnet, A. Gonzales, C. Azevedo-Coste, M. Hayashibe, S. Cotton, P. Fraisse, "Determination of subject specific whole-body centre of mass using the 3D Statically Equivalent Serial Chain", Gait & Posture, vol.41, no.1, pp.70-5, 2015.

- M. Hayashibe, S. Shimoda, " Synergetic Motor Control Paradigm for Optimizing Energy Efficiency of Multijoint Reaching via Tacit Learning", Frontiers in Computational Neuroscience, vol.8, 00021, 2014. (Chap.7, Annex)

- Z. Li, M. Hayashibe, C. Fattal, D. Guiraud, " Muscle Fatigue Tracking with Evoked EMG via Recurrent Neural Network: Toward Personalized Neuroprosthetics", IEEE Computational Intelligence Magazine, vol.9, no.2, pp.38-46, 2014. (Chap.3, Annex)

- A. Gonzalez, M. Hayashibe, V. Bonnet, P. Fraisse, "Whole Body Center of Mass Estimation with Portable Sensors: Using the Statically Equivalent Serial Chain and a Kinect", Sensors, vol.14, no.9, 16955-16971, 2014. (Chap.6)

- F. Bonnetblanc, G. Herbet, P. Charras, M. Hayashibe, D. Guiraud, H. Duffau, B. Poulin-Charronnat, " Asymmetric interhemispheric excitability evidenced by event-related potential amplitude patterns after "wide-awake surgeryöf brain tumours", Experimental Brain Research, vol.232, no.12, pp.3907-18, 2014.

- M. Papaiordanidou, M. Hayashibe, A. Varray, C. Fattal, D. Guiraud, " A new method for muscle fatigue assessment: Online model identification techniques", Muscle & Nerve, vol.50, no.4, pp.556-63, 2014. (Chap.2, Annex)

- Q. Zhang, M. Hayashibe, C. Azevedo-Coste, " Evoked Electromyography-Based Closed-Loop Torque Control in Functional Electrical Stimulation", IEEE Transactions on Biomedical Engineering, vol.60, no.8, pp.2299-2307, 2013. (Chap.4)

- M. Hayashibe, D. Guiraud, "Voluntary EMG-to-Force Estimation with a Multi-Scale Physiological Muscle Model", Biomedical Engineering Online, vol.12, no.86, 2013. (Chap.5)

- M. Benoussaad, P. Poignet, M. Hayashibe, C. Azevedo-Coste, C. Fattal, D. Guiraud, " Experimental parameter identification of a multi-scale musculoskeletal model controlled by electrical stimulation: application to patients with spinal cord injury", Medical & Biological Engineering & Computing, vol.51, pp.617-631, 2013.

- M. Hayashibe, D. Guiraud, P. Poignet, " In-vivo Identification of Skeletal Muscle Dynamics with Nonlinear Kalman Filter :Comparison between EKF and SPKF", ISRN Rehabilitation, vol.2013, 610709, 10 pages, 2013. (Chap.2)

- M. Hayashibe, Q. Zhang, D. Guiraud, C. Fattal, " Evoked EMG based Torque Prediction under Muscle Fatigue in Implanted Neural Stimulation", Journal of Neural Engineering, vol.8, 064001,2011. (Chap.3, Annex)

- Q. Zhang, M. Hayashibe, P. Fraisse, D. Guiraud, " FES-Induced Torque Prediction with Evoked EMG Sensing for Muscle Fatigue Tracking", IEEE/ASME Transactions on Mechatronics, Focused Section on Biosignal sensing, vol.16, no.5, pp.816-826, 2011. (Chap.3)

- H. El Makssoud, D. Guiraud, P. Poignet, M. Hayashibe, P.B. Wieber, K. Yoshida, C. Azevedo-Coste, " Multiscale modeling of skeletal muscle properties and experimental validations in isometric conditions", Biological Cybernetics, vol.105, no.2, pp.121-38, 2011. (Chap.2)

CHAPTER 1

Introduction

1.1 Summary of Past Research Activity

I obtained my scientific background at Department of Mechano-Aerospace Engineering, Tokyo Institute of Technology in 1999. In Master degree, I majored in automatic control, and robotics in Department of Mechano-Informatics, University of Tokyo and was supervised by Prof. Yoshihiko Nakamura. I started the research which applies the technology of robotics and computer science to the medical field. The work of " Laser Pointing Endoscope for Intraoperative Geometric Acquisition and Operational Support of Surgical Robot ”was my first experience for the medical application. I started the collaboration with surgeons and performed in-vivo experiment on pigs. After master course, I was involved in the environment that would provide a close contact with clinical medicine and hospital. I moved to Jikei University School of Medicine working as assistant professor for 5.5 years since 2001. My research covered the interdisciplinary area of medical imaging and computer science for biomedical information. I have done many collaborative works with radiologists and surgeons. I designed the operating room and related parts to the surgical apparatus built at the Jikei University Hospital. The High-Tech Navigation Operating Room received the Good Design Award 2005 prize. For the new operating room, I developed Data-Fusion Display System with Volume Rendering of Intraoperatively Scanned CT Images. The 3D volumetric data that reflects a patient's inner structure is directly displayed on the monitor through video images of the surgical field. It was challenging for the system that the surgical navigation data was intraoperatively obtained and was not based on preoperative images. The data-fusion display system received the Gold Prize of the CAS Young Investigator Award granted by Hitachi Medical Systems Co. PhD degree was obtained at Univ. of Tokyo in 2005. For Laser pointing endoscope, its function was extended to instantaneously acquire and visualize shape and texture of the area of interest under minimal invasive surgery for the application of surgical navigation during thesis period in Japan. This work is now cited by relevant researchers and introduced in recent technical review for Methods for 3D Reconstruction from images in Minimal Invasive Surgery in IEEE magazine.

From 2007, I sought the experience of researching abroad and joined DEMAR project as post-doc. From 2008, I work as CR2 tenured researcher. My work is related to computational modeling and identification of skeletal muscle under Functional Electrical Stimulation. The main research theme has been changed from surgical robotics to rehabilitation robotics. However, it is still in the same area in global point of view to enhance the functionality of biomedical system. For surgical robotics, it is little far from human system itself because it supports mainly the surgeons' interface. In rehabilitation robotics, the technology should accompany with human system more internally. That was my point where I was attracted by the topic of DEMAR project. An identification method for biomechanical parameters of nonlinear muscle model has been proposed and developed. This method is based on the in-vivo experimental data acquisition. It could contribute for the prediction of the nonlinear force of stimulated muscle under FES. The comparison of experimental muscle force and the simulated force shows the feasi-

bility of the identification. After we confirmed the performance on animal experiment, it was applied for spinal cord injured patient. Especially, Phd student from Faculty of sports science used the program to identify the patient-specific parameters in muscle model and to track the fatigue phenomena by stimulation. The program could be used independently from my presence and could be used for her fatigue analysis work. Normally, force measurement chair was used to obtain the measured torque for fatigue analysis. However, it is not usable for the daily life of spinal cord injured patient, then I have started the muscle force prediction only from evoked EMG signals. For the patient mobility, it is very meaningful to use such portable type sensors to enhance FES control. As the identification code itself can automatically update the new parameters from incoming biosignals, it is possible to implement the identification computation together with a wireless FES module to update the control input in the stimulator. This kind of intelligent computation and realtime performance should be the key to enhance FES and also for advanced Neuroprosthetics. I am eager to continue the research to support and understand complex human system with the technology of computational modeling and control. This HDR manuscript contents are synthetic summary of the research activity after I joined INRIA, France in 2008.

1.2 Social Demand for Personalized Rehabilitation

Patients in need of rehabilitation, assistance and neuroprosthetics are increasing in our aging society all over the world. The United Nations expects that by 2015, 16% of the world's population will have become 65 years old. As the world's population continues to age, there is an increased need for systems that can monitor and improve motor rehabilitation standards for the elderly as well as for other motor impaired subjects like post-stroke patients.

Regarding another category of the motor impaired, spinal cord injured (SCI) patients, 90 million people currently suffer world wide. In Europe, there are approximately 300,000 paraplegics, the average of whom is 31 years old, while in the United States 250,000 people suffer from spinal cord injuries (10,000 people each year). In two-thirds of cases, road accidents are the cause of injury, with sporting accidents making up another 10 percent of the total. Advances in treatment have resulted in increasing number of people with spinal cord injuries surviving and living decently with their disability. 85 thousand people each year survive a traumatic spinal cord injury and prepare to spend an average of 40 years or more in a wheelchair. Patients in need of rehabilitation, prosthetics and assistance are usually supported by social welfare and have difficulties in reintegrating a normal life after their accident. Reducing the expected cost for the health care of SCI survivors and the aging society is really a critical social problem. The social benefit that could be derived from advanced computational methods in motor rehabilitation would be quite important to improve the quality of life for motor-impaired patients during their daily activities. The concept of human-centric systems can potentially contribute to this objective, especially by providing personalized modeling and control of the patient-specific motor property toward tailored neuroprosthetics and rehabilitation.

1.3 Thesis Organization

Human motor function consists of different levels of components from peripheral to central mechanism. This HDR thesis focuses on the computational modeling aspects, however it is oriented to contribute to modeling and control of these different levels from peripheral to central: From local neuroprosthetic muscle control to central motor learning control. Our INRIA Demar team is specialized first for neuroprosthetics and functional electrical stimulation (FES). I have been in charge of modeling aspects for personalized identification of stimulus-evoked neuromuscular dynamics as in Chap.2. It is extended into personalized neuroprosthetics as in Chap.3 to predict subject-specific torque estimation by means of evoked electromyography (eEMG) even under muscle fatigue, which is fundamental problem over FES. The EMG Feedback Predictive Muscle Control in FES is archieved including real-time performance together with wireless portable stimulator as in Chap.4. Physiological muscle modeling under FES as in Chap.2 is extended also for volitional motor actions. The work of inversed muscle activation solution using muscle synergy extraction is also proposed in Chap.5 envisaging for finding redundant muscle activation patterns in multi-channel neuroprosthetics. Chap.6 is regarding personalized home rehabilitation, especially focusing on the development of personalized balance measure considering subjectspecific differences by adaptive identification. The rehabilitation in general is indeed a re-learning process under the given dynamics constraints. Chap.7 deals with developing a novel computational motor control/learning paradigm to understand how redundancy is managed in human central nervous system.

The configuration of the HDR thesis is as follows:

- Chap.2 Personalized Identification of Evoked Neuromuscular Dynamics
- Chap.3 Personalized Neuroprosthetics -Torque Estimation under Muscle Fatigue
- Chap.4 EMG Feedback Predictive Muscle Control in FES
- Chap.5 Personalized Modeling for Volitional Motor Actions
- Chap.6 Personalized Home Rehabilitation
- Chap.7 Synergetic Motor Learning Control

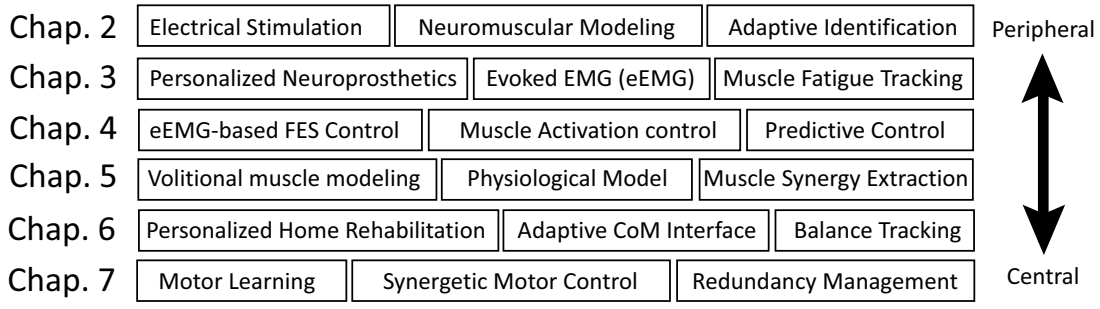

FIGURE 1.1: Thesis Organization.

CHAPTER 2

Personalized Identification of Evoked Neuromuscular Dynamics

2.1 Introduction

One of the challenging issues in computational neuroprosthetics control is that there is a large variety of patient situations depending on the type of neurological disorder. To improve the performance of motor neuroprosthetics beyond the current limited use of such system, subject-specific modeling would be essential. In addition, human characteristics are basically time variant, for instance, neuromuscular dynamics may vary according to muscle fatigue. In order to correspond to such time-varying characteristic, a robust bio-signal processing and a model-based control which can manage the nonlinearity and time variance of the system, would bring break-through and new modality in rehabilitation. The social benefit coming from advanced computational methods in motor function rehabilitation would be quite huge all over the world. There is a significant meaning for the technology of computer science and robotics to be applied more actively to general rehabilitation framework.

For example, heart pacemaker is one of the most successful neuroprosthetic systems which uses electrical impulses to regulate the beating of the heart. The local dynamics regarding the control of heart pacemaker is always similar between the patients. That is why it could get excellent results for many numbers of patients. There is no strong variety between patients and normally they have static settings in time domain. In contrast, in the case of motor neuroprosthetics, the local dynamics of neuromuscular system is quite different from patient to patient. This is a reason why motor neuroprosthetics have not reached the level of standard and vastly worldwide uses like pacemaker and cochlear implant. In my opinion, the difficulty for motor prosthetics is coming from these conditions:

1. The system is complex and there are many parameters to be considered.
2. The characteristic of the system is largely different depending on each person.
3. The parameters of the system are not static and time-variant.
4. The dynamics of the system is nonlinear and cannot be controlled with linear approximation.

In order to correspond to time-varying characteristics, a robust bio-signal processing and a model-based control which can manage the nonlinearity and time variance of the system, would bring break-through and new modality in rehabilitation. This thesis introduces some recent results regarding subject-specific modeling and adaptive identification which can correspond to muscle property variation in clinical situation.

2.2 Muscle Modeling and FES

Functional electrical stimulation (FES) is an effective technique to evoke artificial contractions of paralyzed skeletal muscles. It has been employed as a general method in modern rehabilitation to partially restore motor function for patients with upper neural lesions [Kobetic et al., 1997]. Recently, the rapid progress in microprocessor technology provided the means for computer-controlled FES systems [Donaldson et al., 1997, Kobetic et al., 1999, Guiraud et al., 2006]. A fundamental problem concerning FES is how to handle the high complexity and nonlinearity of the neuro-musculo-skeletal system [Durfee, 1993, Riener, 1999]. In addition, there is a large variety of patient situations depending on the type of neurological disorder. To improve the performance of motor neuroprosthetics beyond the current limited use of such system, subject-specific modeling is essential. The use of a mathematical model can improve the development of neuroprosthetics by optimizing their functionality for individual patients.

A mathematical model makes it possible to describe the relevant characteristics of the patient's skeletal muscle and to accurately predict the force as a function of the stimulation parameters. Indeed, synthesis of stimulation sequences or control strategies to achieve movement can be efficiently computed and optimized using numerical models. Therefore, it can contribute to enhancing the design and function of controls applied to FES. Over the years, a great variety of muscle models has been proposed, differing in their intended application, mathematical complexity, level of structure considered and their fidelity to the biological facts. Some of them have attempted to exhibit the microscopic or macroscopic functional behavior, for instance Huxley [Huxley, 1957] and Hill [Hill, 1938]. The distribution-moment model [Zahalak, 1981] constitutes a bridge between the microscopic and macroscopic levels. It is a model for sarcomeres or whole muscle which has been extracted via a formal mathematical approximation from Huxley cross-bridge models. Models integrating geometry of the tendon and other macroscopic consideration can be found in [Zajac, 1989]. A study by Bestel-Sorine [Bestel and Sorine, 2000], based on both microscopic Huxley and macroscopic Hill type model, proposed an explanation of how the beating of cardiac muscle is achieved through a chemical control input. It integrated the calcium dynamics in muscle cells that stimulate the contractile element of the model. Starting with this concept, we adapted it for striated muscle [El Makssoud et al., 2011]. We proposed a musculotendinous model which considered the muscular masses and viscous frictions in muscle-tendon complex. This model is represented by differential equations where the outputs are the muscle's active stiffness and force. The model input represents the actual electrical signal as provided by the stimulator in FES.

2.3 *In-vivo* Identification for Subject-specific Parameters

In actual FES system, the appropriate tuning is achieved empirically by intensively stimulating the patient's muscle for each task. If this adjustment could be calculated in the simulation, and if we could find the best signal pattern using virtual skeletal muscle, such method would be very helpful for movement synthesis for spinal cord injured (SCI) patients. However,

in order to perform the simulation, an accurate skeletal muscle model is required to reproduce a well-predicted force for each muscle corresponding to the patient-specific characteristics.

For any biological systems, identification is a difficult problem due to the fact that: i) measurements must be as non-invasive, particularly on humans, ii) some entities can not be directly measured, iii) an experimental setup and protocol have to be designed and certified, iv) inter-subject variations can be large, v) the large non-linearity and complexity of the models cause some optimization algorithms to fail. Thus, few papers address biomechanical parameters identification in FES context, and they used macroscopic model for global force production [Riener et al., 2000]. Consequently, we described an approach for coupling the model with *in-vivo* measurements, i.e. using a multi-scale muscle model in an estimation procedure in order to perform the identification of the parameters, hence giving access to physiologically meaningful parameters of the muscle. Preliminary result was reported in [Hayashibe et al., 2008].

The skeletal muscle dynamics are in particular highly nonlinear, and we need to identify many unknown physiological parameters if a multiscale model is applied. The main objective of this paper is to develop an experimental computational method to identify unknown internal parameters from the limited information. In this work, a Sigma-Point Kalman Filter (SPKF) was applied to the *in-vivo* experimental data to identify internal states in the nonlinear dynamics of multiscale skeletal muscle model. SPKF has higher accuracy and consistency for nonlinear estimation than EKF theoretically. The feasibility of the both identification is verified by comparison. The computational performance is discussed.

The outline of the paper is as follows. The next section presents the formulation of the skeletal muscle model controlled by FES. The following section is devoted to the experimental identification of the model for isometric contraction, including the identification protocol. The experimental measurement was performed *in-vivo* on rabbits. Then, we present detailed results of the parameter estimation, the comparison with EKF and cross-validation which illustrates the pertinence of the identification. Finally, we present some discussion, conclusions and perspective in the last sections.

2.4 Functional Skeletal Muscle Model

Muscle modeling is complex, in particular when the model is based on biomechanics and physiological realities. Most of the muscle models have been based on phenomenological models derived from Hill's classic work [Hill, 1938] and well summarized by Zajac [Zajac, 1989]. Hill macroscopic model is standard muscle model for practical use. Recent work [Perreault et al., 2003] performed the validation of Hill model during functionally relevant conditions. They concluded that model errors are large for different firing frequencies and largest at the low motor unit firing rates relevant to normal movement. They pointed out that the reason may come from the Hill model assumption to consider muscle activation, force-length and force-velocity properties independently. It was suggested that more physiological coupling between activation and force-velocity properties can be demonstrated in microscopic crossbridge models incorporating a dependence between physiologically based activation and cross-bridge attachment [Perreault et al., 2003]. Thus, our approach is to provide a multiscale physiology-based model on the both micro and macro scale fact to obtain meaningful internal parameters.

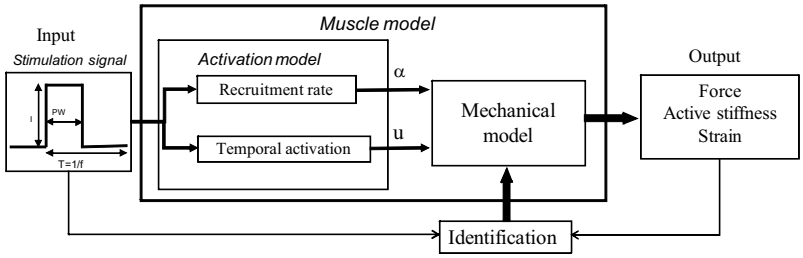

FIGURE 2.1: Outline of skeletal muscle model and its identification.

Our muscle model is composed of two elements of different nature: i) an activation model which describes how an electrical stimulus generates an action potential (AP) and initiates the contraction, and ii) a mechanical model which describes the dynamics in force (Fig. 2.1). For details of the muscle model, refer to the previously published article [El Makssoud et al., 2011]. Here, a brief summary of the model and the information necessary for the identification are given.

2.5 Activation Model

The activation model describes the electrical activity of muscle which represents the excitation-contraction phenomena. In muscle physiology, it is known that two input elements dominate muscle contraction: fiber recruitment rates and temporal activation [Riener and Quintern, 1997]. The recruitment rates determine the percentage of recruited motor units. In Hill model, it has only one input which corresponds to this recruitment rate. Hill model is mainly applied for voluntary contraction where temporal activation is not dominant. However, in FES, since all muscle fibers are synchronously activated. This temporal activation which occurs by every stimulation pulse, is important. The recruitment rates can be determined on the pulse width (PW) and pulse amplitude of signal I, generated by the stimulator [Durfee and MacLean, 1989]. The recruitment rate $\alpha(PW, I)$ can be assumed to be a constant value when PW and I remain constant.

The temporal activation can be considered as the underlying physiological processes which describes the chemical input signal, u, that brings muscle cells into contraction as shown in Fig. 2. Muscle contraction is initiated by an AP along the muscle fiber membrane, which goes deep into the cell through the T-tubules. It causes calcium releases that induce the contraction process when its concentration rises above a threshold and is sustained till the concentration drops back below this threshold once again. Hatze [Hatze, 1977] gives an example of calcium dynamics $[Ca^{2+}]$ modeling. Since we focus on the mechanical response in this paper, we choose a simple model that renders the main characteristics of the dynamics. The contraction-relaxation cycle is triggered by the $[Ca^{2+}]$ associated with two phases: i) contraction and, ii) relaxation as in Fig. 2.2. We use a delayed (τ) model to take into account the propagation time of the AP and an average time delay due to the calcium dynamics. The frequency of the chemical input, u, can be defined from the stimulation frequency. The time delay and the contraction time can be obtained from a twitch test by single stimulation pulse. A contraction takes place

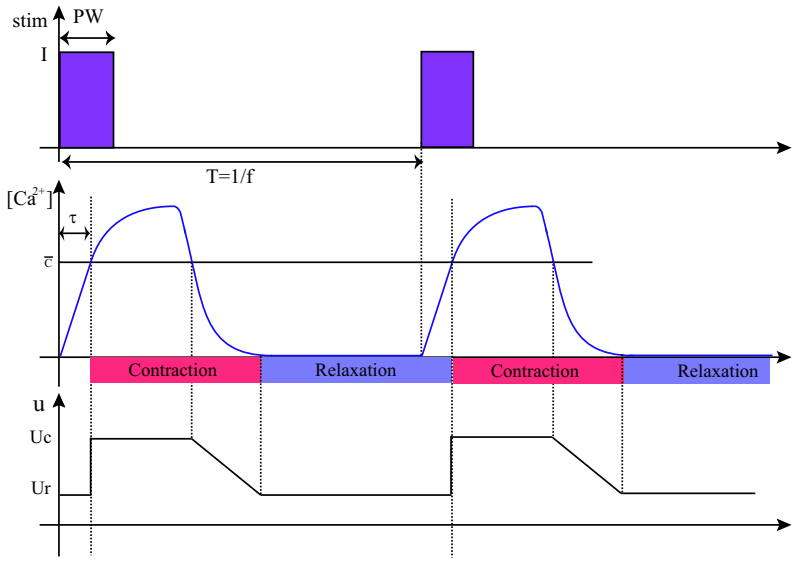

FIGURE 2.2: Chemical control input u for temporal activation.

with a kinetics U_c then, if no other AP has been received in the mean time, an active relaxation follows indefinitely with a kinetics U_r. U_c is linked to the rate of actine-myosine cycle whereas U_r is related to the rate of crossbridge breakage. Finally u can be written as follows, where $\Pi_c(t)$ is a trapezoidal switching function which connects relaxation and contraction state from 0 to 1.

$$u = \Pi_c(t)U_c + (1 - \Pi_c(t))U_r \tag{2.1}$$

2.5.1 Mechanical Model

The model is based on the macroscopic Hill-Maxwell type model and the microscopic description of Huxley [Huxley, 1957]. For cross-bridge modeling, Huxley proposed an explanation of the interaction cross-bridge in a sarcomere. A sarcomere model can be used to represent a whole muscle which is assumed to be a homogeneous assembly of identical sarcomeres. The distribution-moment model of Zahalak [Zahalak, 1981] is a model for sarcomeres or whole muscle which is extracted via a formal mathematical approximation from Huxley cross-bridge models. This model constitutes a bridge between the microscopic and macroscopic levels. Based on Huxley and Hill-type models, Bestel-Sorine [Bestel and Sorine, 2000] proposed an explanation of how the beating of cardiac muscle may be performed, through a chemical control input, connected to the calcium dynamics in muscle cell, that stimulates the contractile element of the model.

The model is composed of macroscopic passive elements and a contractile element E_c controlled by input commands: the chemical input, u, as suggested by Bestel-Sorine [Bestel and Sorine, 2000] for the cardiac muscle on the sarcomere scale, and the recruitment rate, α, on the fiber scale as shown in Fig. 2.3. In order to express isometric contractions, whereas the skeleton is not actuated, our muscle model is introduced with masses m (kg) and linear viscous dampers λ_{s1}, λ_{s2} (Ns/m) to ensure energy dissipation. On both sides of E_c, there

are elastic springs, k_{s1}, k_{s2} (N/m), and viscous dampers to express the visco-elasticity of the muscle-tendon complex. The parallel element, K_p, mainly represents surrounding tissues, but it can be omitted in isometric contraction mode. We assume the symmetric form with the two masses and passive elements identical. Here, $\varepsilon_s = \varepsilon_{s1} = \varepsilon_{s2}$, $k_s = k_{s1} = k_{s2}$, and $\lambda = \lambda_{s1} = \lambda_{s2}$. L_{c0} and L_{s0} (m) are the lengths of E_c and k_s in the rest state. Initially, we can define the relative length variation ε as positive when the length increases, as in (2.2). In particular, in the case of isometric contraction, the following relationship exists (2.3):

$$\varepsilon_s = \frac{L_s - L_{s0}}{L_{s0}} \qquad \varepsilon_c = \frac{L_c - L_{c0}}{L_{c0}} \tag{2.2}$$

$$2L_{s0}\varepsilon_s + L_{c0}\varepsilon_c = 0 \tag{2.3}$$

The dynamical equation of one of the masses is given by (2.4). F_c and k_c express the force and the stiffness of E_c, respectively. The force F_e at the output of this muscle model is the sum of the spring force F_s and the damping force F_d. When we measure the tension of skeletal muscle under *in-vivo* conditions, the experimentally measured force is equivalent to F_e. When we take the ratio of F_c and F_e, L_{s0} is offset and can be written as in (2.6). (2.7) is the relational equation in Laplace transform. From this relationship, the differential equation (2.8) can be obtained.

$$mL_{s0}\ddot{\varepsilon}_s = F_c - k_s L_{s0}\varepsilon_s - \lambda L_{s0}\dot{\varepsilon}_s \tag{2.4}$$

$$F_e = F_s + F_d = k_s L_{s0}\varepsilon_s + \lambda L_{s0}\dot{\varepsilon}_s \tag{2.5}$$

$$\frac{F_c}{F_e} = \frac{m\ddot{\varepsilon}_s + \lambda\dot{\varepsilon}_s + k_s\varepsilon_s}{\lambda\dot{\varepsilon}_s + k_s\varepsilon_s} \tag{2.6}$$

$$\frac{\mathcal{L}[F_c]}{\mathcal{L}[F_e]} = \frac{ms^2 + \lambda s + k_s}{\lambda s + k_s} \tag{2.7}$$

$$m\ddot{F}_e + \lambda\dot{F}_e + k_s F_e = \lambda\dot{F}_c + k_s F_c \tag{2.8}$$

Finally, in isometric contraction, the differential equations of this model can be described as follows:

$$\dot{k}_c = -k_c u + \alpha k_m \Pi_c U_c - k_c|\dot{\varepsilon}_c| \tag{2.9}$$

$$\dot{F}_c = -F_c u + \alpha F_m \Pi_c U_c - F_c|\dot{\varepsilon}_c| + L_{c0}k_c\dot{\varepsilon}_c \tag{2.10}$$

$$\ddot{F}_e = -\frac{\lambda}{m}\dot{F}_e - \frac{k_s}{m}F_e + \frac{\lambda}{m}\dot{F}_c + \frac{k_s}{m}F_c \tag{2.11}$$

$$\ddot{\varepsilon}_c = -\frac{2F_c}{mL_{c0}} - \frac{k_s}{m}\varepsilon_c - \frac{\lambda}{m}\dot{\varepsilon}_c \tag{2.12}$$

The dynamics of the contractile element correspond to (2.9) and (2.10). The terms k_m and F_m are the maximum values for k_c and F_c, respectively. From (2.3) and (2.4), the differential equation for ε_c is obtained as in (2.12). The internal state vector of this system should be set as $\mathbf{x} = \begin{bmatrix} k_c & F_c & F_e & \dot{F}_e & \varepsilon_c & \dot{\varepsilon}_c \end{bmatrix}$.

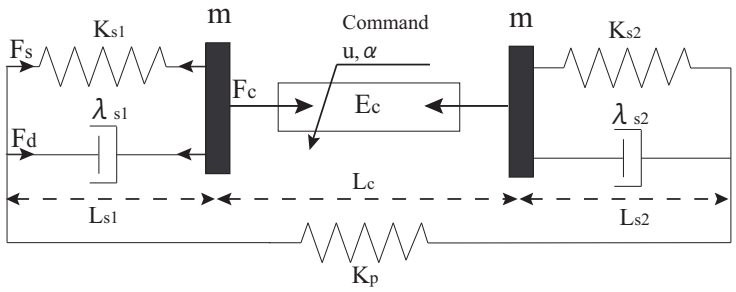

FIGURE 2.3: Macroscopic mechanical configuration of the muscle model.

2.6 Experimental Identification

In this study, we have developed a method to identify the parameters in the mechanical part of a skeletal muscle model. The input controls of the model are set as the static recruitment rate α and the chemical control input u from the activation model. These two controls are computed from the FES input signal. Note that the identification was performed with constant FES parameters for pulse width and intensity of electrical stimulation so that the recruitment rate is constant. The amplitude and pulse width were selected to recruit 90% of the maximum muscular force, then α can be set as 0.9 for the fiber recruitment. In addition, the calcium dynamics in our model induce a time delay and an on/off control which represents contraction/relaxation so that correct data processing can avoid the detailed calcium dynamics. The trigger for signal u can be calculated from the timing of the electrical stimulation. U_c and U_r are set as 20 and 15 respectively, as in [El Makssoud, 2005].

In isometric contraction, the differential equations of skeletal muscle dynamics are straightly given in (2.9)-(2.12). In this case, K_c, F_c, F_e and ϵ_c are unknown time-varying values and m, λ_s and L_{c0} are unknown static parameters to be estimated. For the identification of this model, it is a nonlinear state-space model, and many state-variables are not measurable. Moreover, *in-vivo* experimental data include some noise. Hence we need an efficient recursive filter that estimates the state of a dynamic system from a series of noisy measurements.

2.6.1 Sigma-Point Kalman Filter

For this kind of nonlinear identification, extended Kalman filter (EKF) is the well-known standard method. In EKF, the nonlinear equation should be linearized to first order with partial derivatives (Jacobian matrix) around a mean of the state. The optimal Kalman filtering is then applied to the linearized system. When the model is highly nonlinear, EKF may give particularly poor performance and diverge easily. In skeletal muscle dynamics, its state-space is dramatically changed between the contraction and relaxation phases. At this time, partial derivatives would be incorrect due to the discontinuity. Therefore, we introduced the sigma-point Kalman filter (SPKF). The initial idea was proposed by Julier [Julier and Uhlmann, 1997], and has been well described by Merwe [van der Merwe and Wan, 2003]. SPKF uses a deterministic sampling technique known as the unscented transform to pick a minimal set of sample points (called sigma points) around the mean. These sigma points are propagated through the true

nonlinearity. This approach results in approximations that are accurate to at least second order in a Taylor series expansion. In contrast, EKF results in only first order accuracy.

An outline of the SPKF algorithm is described. For details, the reader should refer to [van der Merwe and Wan, 2003][Julier and Uhlmann, 2004]. The general Kalman framework involves estimation of the state of a discrete-time, nonlinear dynamic system,

$$\mathbf{x}_{k+1} = \mathbf{f}(\mathbf{x}_k, \mathbf{v}_k) \tag{2.13}$$

$$\mathbf{y}_k = \mathbf{h}(\mathbf{x}_k, \mathbf{n}_k) \tag{2.14}$$

where $\mathbf{x}_k$ represents the internal state of the system to be estimated and $\mathbf{y}_k$ is the only observed signal. The process noise $\mathbf{v}_k$ drives the dynamic system, and the observation noise is given by $\mathbf{n}_k$. The filter starts by augmenting the state vector to L dimensions, where L is the sum of dimensions in the original state, model noise and measurement noise. The corresponding covariance matrix is similarly augmented to an L by L matrix. In this form, the augmented state vector $\hat{\mathbf{x}}_k^a$ and covariance matrix $\mathbf{P}_k^a$ can be defined as in (2.15)(2.16).

$$\hat{\mathbf{x}}_k^a = E[\mathbf{x}_k^a] = \begin{bmatrix} \hat{\mathbf{x}}_k^T & \bar{\mathbf{v}}_k^T & \bar{\mathbf{n}}_k^T \end{bmatrix}^T \tag{2.15}$$

$$\begin{aligned} \mathbf{P}_k^a &= E[(\mathbf{x}_k^a - \hat{\mathbf{x}}_k^a)(\mathbf{x}_k^a - \hat{\mathbf{x}}_k^a)^T] \\ &= \begin{bmatrix} \mathbf{P}_{\mathbf{x}_k} & 0 & 0 \\ 0 & \mathbf{Q}_{\mathbf{v}_k} & 0 \\ 0 & 0 & \mathbf{R}_{\mathbf{n}_k} \end{bmatrix} \end{aligned} \tag{2.16}$$

where $\mathbf{P}_\mathbf{x}$ is the state covariance, $\mathbf{Q}_\mathbf{v}$ is the process noise covariance and $\mathbf{R}_\mathbf{n}$ is the observation noise covariance.

In the process update, the 2L+1 sigma points are computed based on a square root decomposition of the prior covariance as in (2.17), where $\gamma = \sqrt{L + \lambda}$, and λ is found using $\lambda = \alpha^2(L+\kappa) - L$. α is chosen in $0 < \alpha < 1$ which determines the spread of the sigma-points around the prior mean and κ is usually chosen equal to 0. The augmented sigma-point matrix is formed by the concatenation of the state sigma-point matrix, the process noise sigma-point matrix, and the measurement noise sigma-point matrix, such that $\mathcal{X}^a = \begin{bmatrix} (\mathcal{X}^x)^T & (\mathcal{X}^v)^T & (\mathcal{X}^n)^T \end{bmatrix}^T$. The sigma-point weights to be used for mean and covariance estimates are defined as in (2.18). The optimal value of 2 is usually assigned to β.

$$\mathcal{X}_{k-1}^a = \begin{bmatrix} \hat{\mathbf{x}}_{k-1}^a & \hat{\mathbf{x}}_{k-1}^a + \gamma\sqrt{\mathbf{P}_{k-1}^a} & \hat{\mathbf{x}}_{k-1}^a - \gamma\sqrt{\mathbf{P}_{k-1}^a} \end{bmatrix} \tag{2.17}$$

$$\begin{aligned} \omega_0^m &= \lambda/(L+\lambda) \\ \omega_0^c &= \omega_0^m + (1 - \alpha^2 + \beta) \\ \omega_i^c = \omega_i^m &= 1/(2(L+\lambda)) \quad (for \quad i = 1, ..., 2L) \end{aligned} \tag{2.18}$$

And these sigma-points are propagated through the nonlinear function. Predicted mean and

covariance are computed as in (2.20)(2.21) and predicted observation is calculated as in (2.23).

$$\mathcal{X}^x_{k|k-1} = \mathbf{f}(\mathcal{X}^x_{k-1}, \mathcal{X}^v_{k-1}) \tag{2.19}$$

$$\hat{\mathbf{x}}^-_k = \sum_{i=0}^{2L} \omega^m_i \mathcal{X}^x_{i,k|k-1} \tag{2.20}$$

$$\mathbf{P}^-_{\mathbf{x}_k} = \sum_{i=0}^{2L} \omega^c_i (\mathcal{X}^x_{i,k|k-1} - \hat{\mathbf{x}}^-_k)(\mathcal{X}^x_{i,k|k-1} - \hat{\mathbf{x}}^-_k)^T \tag{2.21}$$

$$\mathcal{Y}_{k|k-1} = \mathbf{h}(\mathcal{X}^x_{k|k-1}, \mathcal{X}^n_{k-1}) \tag{2.22}$$

$$\hat{\mathbf{y}}^-_k = \sum_{i=0}^{2L} \omega^m_i \mathcal{Y}_{i,k|k-1} \tag{2.23}$$

The predictions are then updated with new measurements by first calculating the measurement covariance and state-measurement cross correlation matrices, which are then used to determine the Kalman gain. Finally, the updated estimate and covariance are determined from this Kalman gain as below.

$$\mathbf{P}_{\tilde{\mathbf{y}}_k} = \sum_{i=0}^{2L} \omega^c_i (\mathcal{Y}_{i,k|k-1} - \hat{\mathbf{y}}^-_k)(\mathcal{Y}_{i,k|k-1} - \hat{\mathbf{y}}^-_k)^T \tag{2.24}$$

$$\mathbf{P}_{\mathbf{x}_k\mathbf{y}_k} = \sum_{i=0}^{2L} \omega^c_i (\mathcal{X}^x_{i,k|k-1} - \hat{\mathbf{x}}^-_k)(\mathcal{Y}_{i,k|k-1} - \hat{\mathbf{y}}^-_k)^T \tag{2.25}$$

$$\mathbf{K}_k = \mathbf{P}_{\mathbf{x}_k\mathbf{y}_k} \mathbf{P}^{-1}_{\tilde{\mathbf{y}}_k} \tag{2.26}$$

$$\hat{\mathbf{x}}_k = \hat{\mathbf{x}}^-_k + \mathbf{K}_k(\mathbf{y}_k - \hat{\mathbf{y}}^-_k) \tag{2.27}$$

$$\mathbf{P}_{\mathbf{x}_k} = \mathbf{P}^-_{\mathbf{x}_k} - \mathbf{K}_k \mathbf{P}_{\tilde{\mathbf{y}}_k} \mathbf{K}^T_k \tag{2.28}$$

These process updates and measurement updates should be recursively calculated in $k = 1, ..., \infty$ until the end point of the measurement.

2.6.2 Experimental measurement for identification

Stimulation experiments were performed on two New-Zealand white rabbits at Aarhus University Hospital in Aalborg, Denmark, as depicted in Fig. 2.4. Anesthesia was induced and maintained with periodic intramuscular doses of a cocktail of 0.15mg/kg Midazolam (DormicumR, Alpharma A/S), 0.03mg/kg Fetanyl and 1 mg/kg Fluranison (combined in HypnormR, Janssen Pharmaceutica) [El Makssoud et al., 2011].

The left leg of the rabbit was anchored at the knee and ankle joints to a fixed mechanical frame using bone pins placed through the distal epiphyses of the femur and tibia. A tendon of the medial gastrocnemius (MG) muscle was attached to the arm of a motorized lever system (Dual-mode system 310B Aurora Scientific Inc.). The position and force of the lever arm were recorded. An initial muscle-tendon length was established by flexing the ankle to 90°. A bipolar cuff electrode was implanted around the sciatic nerve, allowing the MG muscle to be stimulated. Data acquisition was performed at a 4.8 kHz sampling rate. The muscle force against the electrical stimulation was measured under isometric conditions.

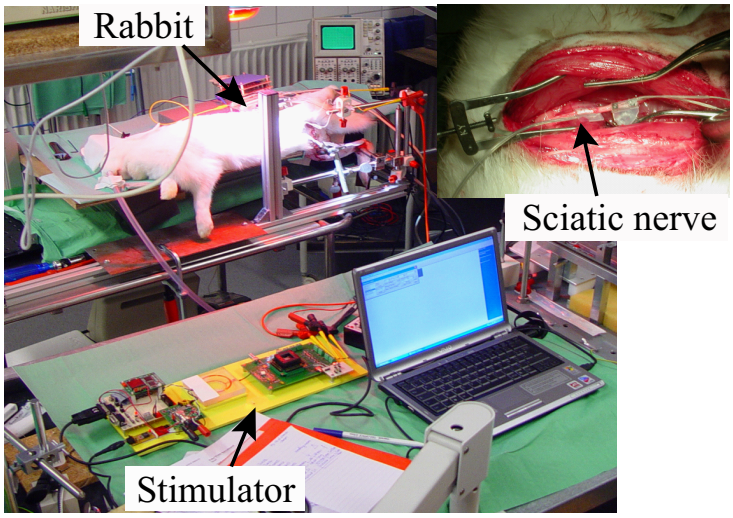

FIGURE 2.4: Overview of the rabbit experiment.

2.7 Result of Identification

In order to facilitate the convergence of the identification, the estimation process has been split into two steps. In the first step, we only estimate geometrical parameter L_{c0}. In the second step, we estimate the dynamic parameters: m and λ. The biomechanical muscle model to be identified is presented as (2.9)-(2.12). We define the state vectors for geometric and dynamic estimations in SPKF as follows:

$$\mathbf{x_g} = \begin{bmatrix} k_c & F_c & F_e & \dot{F}_e & \varepsilon_c & \dot{\varepsilon}_c & L_{c0} \end{bmatrix}$$
$$\mathbf{x_d} = \begin{bmatrix} k_c & F_c & F_e & \dot{F}_e & \varepsilon_c & \dot{\varepsilon}_c & m & \lambda \end{bmatrix}$$

2.7.1 Parameter estimation

Parameter estimation was performed using two rabbit experimental data. The stimulation signal input used for the estimation is composed of two successive pulses (doublet) at 16 Hz and 20 Hz with amplitude 105μA and pulse width 300μs. The stiffness k_s has been estimated separately, using the experiments performed on the isolated muscle. The isolated muscle was pulled with the motorized lever. The stiffness is taken as equal to the slope of the straight line of the passive length versus force relationship. The k_s obtained was 4500 N/m. F_m and k_m can be obtained knowing the force response of muscle to a stimulation pattern with maximum signal parameter values (frequency, amplitude, pulse width). In this case, k_m=1000 N/m and F_m=15 N were obtained from the measurement.

The experimental muscle force against the doublet stimulation (20 Hz) was used for parameter estimation during measurement updates for F_e in SPKF. The evolutions of estimated internal states for k_c and ε_c are obtained as shown in Fig. 2.5. From these behaviors, we can confirm that the contractile element of the model is successfully tracking the contraction represented by the dynamics of differential equations under the estimation process. Fig. 2.6 shows

the estimated parameter L_{c0} and the error covariance. The fact that the error covariace is being decreased during identification process shows stable convergence of the estimation. Even with the different initial values setting, parameter estimation results converged into a particular value in SPKF as shown in Fig. 2.6 (top). We tested the estimation from 7 different initial values with an interval of 5mm from 55mm to 85mm. The color is changed from magenta to cyan in the plot.

As can be seen from the resultant computational behavior on the graphs, the internal state vectors of the muscle model converged well to stationary values even with different initial values. After the complete estimation process for geometric and dynamic parameters, the estimated values are summarized in Table 2.1. Normalized RMS errors between measured and estimated force were also computed for each case. Moreover, the estimated length of the contractile element with each stimulation showed values close to the actual measured lengths of the extracted muscle. The border between the contractile element and tendon is not so clear visually, but it was approximately 7 cm for both rabbit GM muscles. The sizes of two rabbits were similar, in particular, the estimated length of L_{c0} had good correspondence with the measured length for both rabbits and with different frequency stimulations. Physical parameters are impossible to make visual verification, but the estimated intrasubject property is maintained among the parameters obtained by different frequency stimulations from Table 2.1.

TABLE 2.1: Parameter Estimation

	Rabbit 1		Rabbit 2	
Parameters	16Hz	20Hz	16Hz	20Hz
$L_{c0}(cm)$	7.1	7.4	7.4	6.8
$m(g)$	16.5	19.8	36.5	39.8
$\lambda(Ns/m)$	19.7	19.4	19.7	19.2
$NRMS(\%)$	0.60	0.46	1.02	0.82
Measured				
Length of contractile element	7cm		7cm	
Body weight	4.5kg		4.2kg	

2.7.2 Comparison with the Extended Kalman Filter

The Extended Kalman Filter is generally chosen for nonlinear system identification. However, in EKF, first order partial derivatives are used for the computation, which means that a matrix of partial derivatives (Jacobian) is computed around the estimate for each step. The detail of EKF is summarized in Appendix A. When the process and measurement functions $\mathbf{f}$ and $\mathbf{h}$ are highly non-linear, EKF can give particularly poor performance and diverge easily [van der Merwe and Wan, 2003]. The estimate can have a bias due to the linear approximation especially for discontinuous systems.

Using the same computational conditions, such as initial values for states, parameters and covariance matrices, parameter estimation was also performed with EKF to compare the

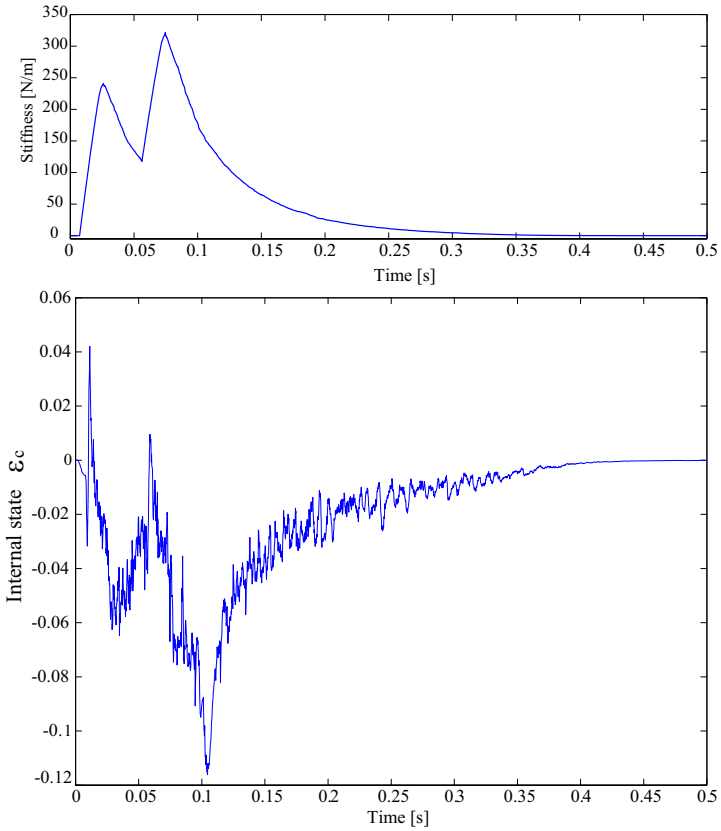

FIGURE 2.5: Estimated state of the stiffness K_c (top) and the strain ε_c (bottom) for the contractile element with SPKF.

estimation quality for this nonlinear system. The estimation results with EKF are shown in Figs. 2.7-2.8. The numerical comparison for SPKF and EKF in 7 different initial conditions is summarized in Table 2.2 both for rabbit1 and rabbit2. With the observation noise covariance $R = 2.5 \times 10^{-3}$, the same as with SPKF, the result with EKF converged computationally as shown at the error covariance of EKF1 in the table. However, the matched result in force level doesn't mean directly that the estimated internal state and parameter are correct. The internal state ε_c in EKF estimation was not well estimated as the contracted strain variation. The difference can be observed by comparing the plots of Figs. 9 and 6 for the EKF and SPKF estimates, respectively. In Fig. 2.5, the estimated state of ε_c has two sharp peaks which correspond to the strain of the contractile element induced by muscle contraction by doublet stimulation. Thus, this internal state reflects the expected phenomenon in muscle dynamics. However, the estimated state in Fig. 2.8 doesn't show sharp deformation induced by stimulation pulse.

The linear approximation in the EKF transformation matrix could be the cause of the lower quality of the state estimation. Finally, it resulted in a bias for parameter estimation. Thus, the converged value for L_{c0} under these conditions is not realistic. The EKF estimation was also performed with the observation noise covariance $R = 2.5 \times 10^{-2}$, giving more uncertainty to the measurement update. In this case, the estimated value became more realistic as did the

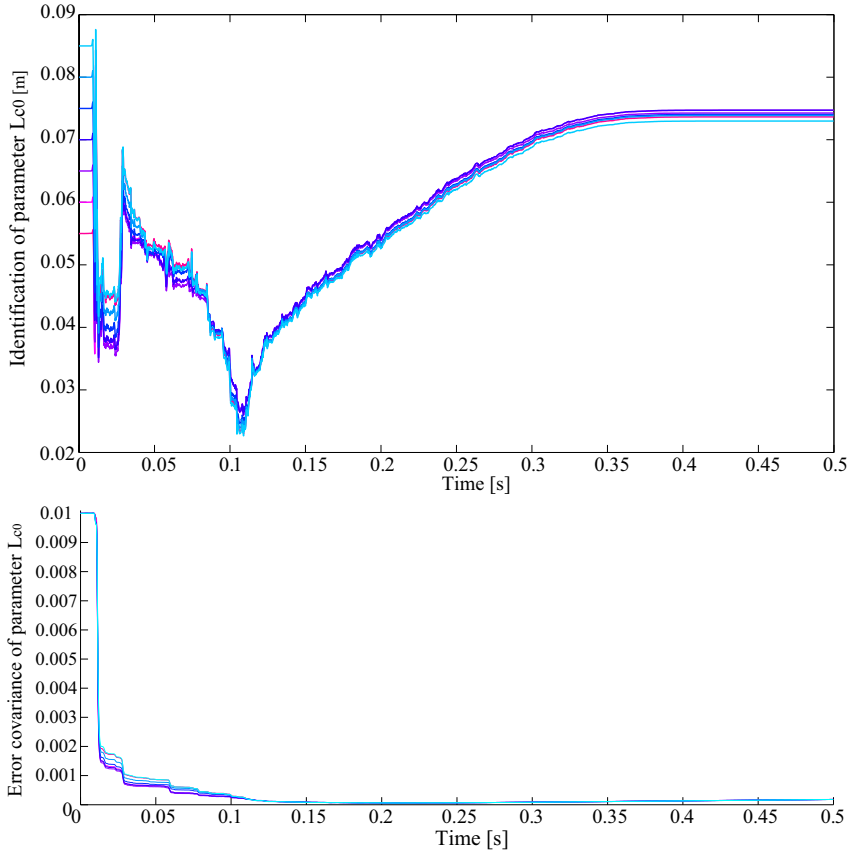

FIGURE 2.6: Estimated parameter for the original length of the contractile element L_{c0} (top) and its error covariance (bottom) with SPKF. The plot color is changed from magenta to cyan with 7 different initial values from 55mm to 85mm.

SPKF estimate. However, the convergence became poor as in Fig. 2.6(bottom) and it was highly dependent on the initial values as in Fig. 2.6(top).

2.7.3 Model Cross-validation

A cross-validation of the identified model was carried out to confirm the validity of this method. The resultant muscle force was calculated using the identified models with the control input generated by the stimulation frequency. Fig. 2.9 show the measured force response of the MG muscle of the rabbit and the simulated force with the identified model. The stimulation was three successive pulses in in I=105μA, PW=300μs, Freq=31.25Hz. The red line indicates the measured muscle force, the blue and green dotted lines are the plots by the identified model with SPKF and EKF1, respectively. The model identified by SPKF could predict the nonlinear force properties of stimulated muscle quite well in this cross-validation. Normally, the muscle property varies greatly, being dependent on the type of muscle, and the force response is highly subject-specific. Therefore, the muscle force prediction by cross-validation is quite difficult even for the approximate prediction especially when force production is predicted for each sti-

TABLE 2.2: Quantitative comparison on identification (SPKF vs EKF) in 7 different initial conditions

Rabbit 1	SPKF	EKF1	EKF2
$P\ for\ F_e$	1.61×10^{-4}	1.61×10^{-4}	4.51×10^{-4}
$P\ for\ L_{c0}$	1.81×10^{-4}	2.47×10^{-4}	2.9×10^{-3}
$mean\ L_{c0}(cm)$	7.4	4.7	7.5
$Deviation\ L_{c0}(cm)$	6.12×10^{-2}	7.67×10^{-3}	0.34
$Average\ errors(\%)$	5.7	33.6	6.9
Rabbit 2	SPKF	EKF1	EKF2
$P\ for\ F_e$	1.72×10^{-4}	1.61×10^{-4}	4.53×10^{-4}
$P\ for\ L_{c0}$	8.97×10^{-4}	3.93×10^{-4}	2.5×10^{-3}
$mean\ L_{c0}(cm)$	6.8	3.9	10.4
$Deviation\ L_{c0}(cm)$	8.92×10^{-2}	3.38×10^{-2}	6.49×10^{-2}
$Average\ errors(\%)$	2.9	44.9	47.9

EKF1 and EKF2 represent EKF estimation with the observation noise covariance $R = 2.5 \times 10^{-3}$ and $R = 2.5 \times 10^{-2}$, respectively. P represents steady-state error covariance.

mulation pulse. The identification based on experimental response would contribute strongly to realistic force prediction in electrical stimulation and FES controller development.

2.8 Discussion

The skeletal muscle model used in this identification protocol is based on both macroscopic and microscopic physiology which is unlike the black-box or other approaches using simple Hill muscle model. The structured model requires more parameters in highly nonlinear dynamics, which have to be estimated by experiment. However, the great advantage of our model is the insight which it can give to a muscle's biomechanical and physiological connections, where the parameters have a physical significance such as length and mass. This paper describes an identification method which uses experimental response and a nonlinear, physiological muscle model to obtain subject-specific parameters. The advantage of animal experiment is to have direct access to extracted muscle for confirmation of the obtained parameter after the experiment.

This work was performed for application of FES stimulated muscles, however, since many living systems have nonlinear dynamics and subject specificity, this kind of identification approach itself could be applied to other organ models and clinical situations. In this work, both SPKF and EKF algorithms were applied for muscle dynamics identification. EKF showed a high dependency on initial settings of the computation and it was difficult to find the effective range of initial states and covariances. In SPKF, the obtained result was more consistent and robust with respect to various initial conditions. Moreover, for SPKF, the computation of a Jacobian is not necessary, so it can easily be applied even to complex dynamics. SPKF results in approximations that are accurate to at least second order in Taylor series expansion. In contrast, EKF results in first order accuracy. Further, the identification accuracy is clealy improved,

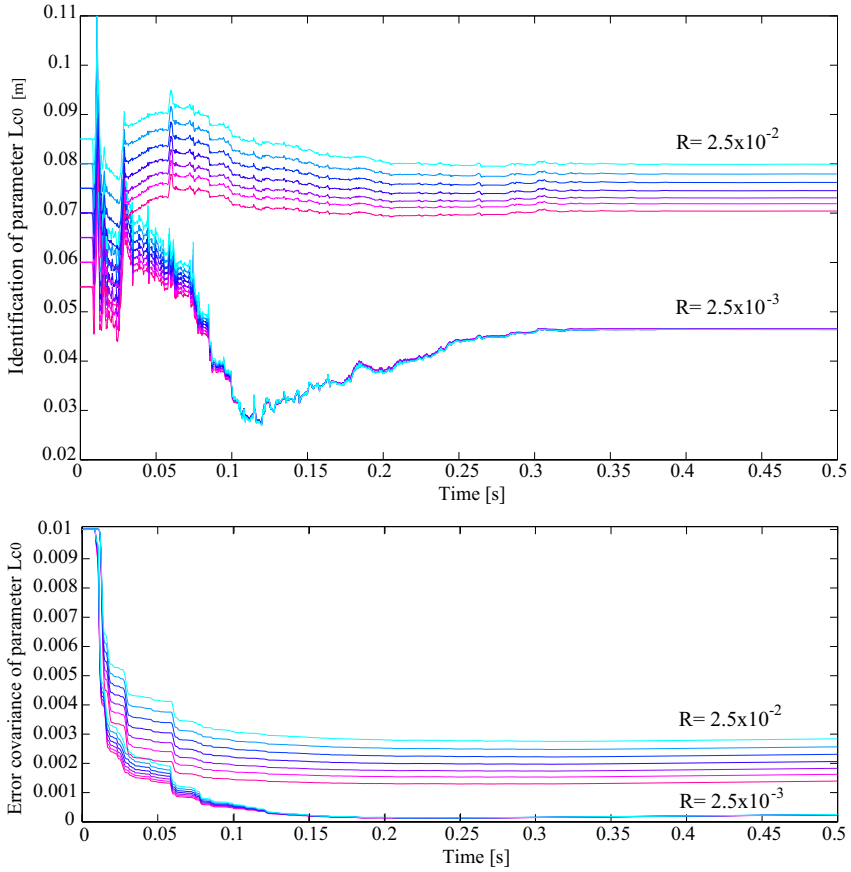

FIGURE 2.7: Estimated parameter for the original length of the contractile element L_{c0} (top) and its error covariance (bottom) with EKF. The plot color is changed from magenta to cyan with 7 different initial values from 55mm to 85mm. The results with two different settings for the observation noise covariance are shown.

especially for nonlinear systems but the computation cost still remains the same as for EKF. Advanced and robust system identification, including designing experimental protocols, has a very important role to improve the control issues in neuroprosthetics. In addition, the main difficulty in understanding human systems is caused by their time varying properties. The systems are not static and change over time. The function of a human being is not always the same, for example, muscle fatigue can easily change the expected force response. In order to deal with the time-varying characteristics of a human system, robust bio-signal processing and model-based control which corresponded to nonlinearity and time variance would provide a break-through in the development of neuroprosthetics [Hayashibe et al., 2011b].

2.9 Conclusion

We have developed an experimental identification method for subject-specific biomechanical parameters of a skeletal muscle model which can be employed to predict the nonlinear force properties of stimulated muscle. The mathematical muscle model accounts for the mul-

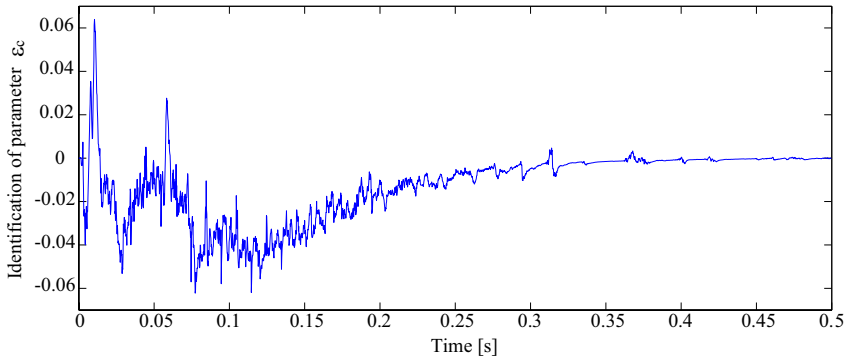

FIGURE 2.8: Estimated state of the strain of the contractile element ε_c with EKF.

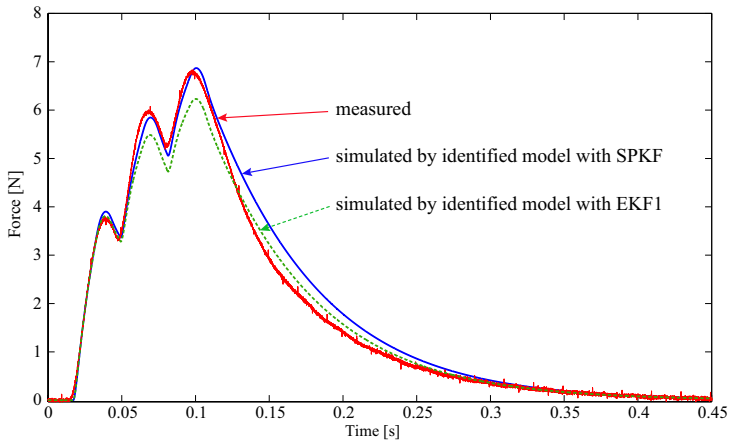

FIGURE 2.9: Measured and simulated isometric muscle force by the identified models with three successive stimulation pulses (in I=105μA, PW=300μs, Freq=31.25Hz).

tiscale major effects occurring during electrical stimulation. Thus, the identification method was required to deal with the high nonlinearlity and discontinous states between muscle contraction and relaxation phase. The identified model was evaluated by comparison with experimental measurements in cross-validation. There was good agreement between measured and simulated muscle force outputs. The result showed the performance which can contribute to the prediction of the nonlinear force of stimulated muscle under FES. The feasibility of the identification could be demonstrated by comparison between the estimated parameter and the measured value. In this study, the identification was performed by sigma-point Kalman filter and extended Kalman filter. The performance was compared and summarized under the same computational conditions. SPKF gives more stable performance than EKF. The internal state in EKF estimation was not well estimated as the contracted muscle strain. In SPKF estimation, keeping the realistic state transition and independence from initial conditions, it could realize converged solution for each identification trial.

SPKF is a Bayesian estimation algorithm which recursively updates the posterior density of the system state as new observations arrive on-line. This framework can allow us to calculate any optimal estimate of the state using newly arriving information. We believe that the

proposed identification method has also the advantage for human muscle identification while it provides not only better accuracy in nonlinear dynamics but also adaptability to time-varying systems. The preliminary result is reported as in [Hayashibe et al., 2010].

CHAPTER 3

Personalized Neuroprosthetics -Torque Estimation under Muscle Fatigue

3.1 Toward Personalized Neuroprosthetics

Muscle fatigue phenomenon and inadequacy of implantable force sensor limit the application of neuroprosthetics. In case of FES, muscle fatigue can drastically change the contraction dynamics and the maximum produced force even when the same set of stimulus parameters is applied. To perform adaptive FES closed-loop control of muscle contraction, the actual force or torque of muscle is preferred to be known accurately. It is thus essential to monitor muscle state and assess the generated force to personalize the patient muscle response and compensate for the fatigue. One of our final purposes is online monitoring muscle state and assessing the muscle force to achieve accurate FES control.

Evoked EMG (eEMG) offers a way of studying the myoelectric features of the neuromuscular activation associated with stimulated muscle contraction. The eEMG signal was found to be highly correlated with FES-induced muscular torque under various stimulation situations [Chesler and Durfee, 1997], and the similar phenomenon was found in the implanted FES SCI subject as well [Hayashibe et al., 2011c]. Moreover, Mwave extracted from the eEMG can be an effective detector for tracking potential muscle fatigue [Heasman et al., 2000]. Accordingly, the electrical stimulation configurations can be adaptively modulated by monitoring the recorded eEMG signals [Chesler and Durfee, 1997]. Exploiting EMG-based estimator for torque estimation could be feasible as well, since the muscle torque highly correlates with both voluntary EMG and eEMG. In non-volitional situations, a lot of evidences have revealed that the explicit relationship between eEMG and muscle torque is time-varying and highly nonlinear, which implies that adopting stationary type estimating approaches would not be enough for stimulated muscle state estimation.

Thus, the muscle response by FES is varying depending on subject's muscle and also changing over time depending on the muscle strength againt fatigue. It is very complicated to predict without having biosignal feedback from the muscle. This chapter tackles this challenge to predict muscle response under FES with personalized identification.

3.1.1 FES-Induced Muscle Fatigue

Muscle fatigue has been defined as a failure to maintain the required or expected force from a repeatedly activated muscle [Edwards, 1981]. In voluntary contraction, a variety of biological and motivational factors contribute to muscle fatigue [Gandevia et al., 1995], such as reduced motor drive by the Central Nervous System (CNS), failure of peripheral electrical transmission, and failure of the muscular contractile mechanism. Although the action potential activated by artificial stimulation is not distinguishable from the action potential activated by natural stimulation, the rate of muscle fatigue during Functional Electrical Stimulation (FES) is much greater than that seen during natural contractions [Binder-Macleod and Snyder-Mackler, 1993].

The exact reason for this fast fatigue phenomenon is complex and is not yet fully understood. The possible reasons can be summarized as: (1) the inverse size principle, according to which the artificial stimulation recruits the motor neurons from the largest to the smallest [Hamada et al., 2004], and the larger the motor neuron, the more fatigable the muscle fiber; (2) motor units are activated in synchronized manner with artificial stimulation, which is different from the asynchronous activation during natural contraction; and (3) the constant order of recruitment, with fast fatigable motor units activated first, then slow fatigue-resistant motor units. These opposite features of FES activation compared with natural contraction have motivated a number of researchers to find the optimal stimulation strategy, as similar to CNS as possible to improve FES performance. Another factor relating to fast fatigue with FES is that the fatigue resistance of the paralyzed muscle decreases after injury [Pelletier and Hicks, 2011].

For an able-bodied person, fatigue can be perceived and compensated by various strategies so that motor function is prolonged. However, for a paraplegic individual with little or even no sensory feedback, fatigue is not detected until the desired movement fails. Therefore, how to detect fatigue before the failure of movement and how force changes with fatigue are both meaningful issues. The ability to detect the muscle state and compensate the muscle changes are both significant for the future FES systems.

3.1.2 EMG and Its Application for Muscle Fatigue Analysis

When muscles contract, they exhibit both electrical and mechanical behaviors. The mechanical behavior can be estimated by muscle force/length, or joint torque/angle. The electrical behavior can be assessed by recording the electrical signals within the muscle, which is referred to as Electromyography (EMG). The EMG signal has been popularly applied in areas like ergonomics and occupational biomechanics for kinesiological or diagnostic purposes. The main applications include determining the activation onset and levels of a muscle, estimating the force produced by muscle, monitoring the rate of muscle fatigue, and analysis of Motor Unit Action Potential (MUAP)s.

The EMG system can be classified according to the interface, such as surface, intramuscular (needle or fine-wire), and implanted [Farnsworth et al., 2008], with the recording channel varying from single to high-density. A typical EMG recording system contains recording electrodes, an amplifier, an A/D converter and wires. The recording electrodes pick up electrical signals underneath them and send them to the amplifier. As the electrical signal is very small, an amplifier gain is selected to amplify the signals. Usually, the amplifier also involves signal processes such as filtering.

In all EMG interfaces, the commonly used surface EMG provides a noninvasive measurement of muscle electrical activities and can be easily implemented in practice. However, when using surface EMG, we should pay more attention to the recording artifacts, which may come from different sources. Accordingly, various measures should be taken to eliminate or reduce them. For instance, environmental artifacts from the surrounding electrical equipments can be removed by a notch filter. Movement artifacts from dynamic movement can be avoided by firmly adhering the electrodes on the muscle and fastening the wire cables. As some muscles are narrow and close to other muscles, the EMG signal may be affected by crosstalk, which is recorded from other muscles we are not interested in. Through careful placement and suffi-

cient interelectrode distance, it can be minimized to some extent [Solomonow et al., 1995]. In addition, some filters (software or hardware) can be used to remove the residual artifacts.

Compared with surface EMG, needle and implanted EMG provide more stable and reliable measurements, but their invasive nature limits their applications. Thus, if needle and implanted EMG are not available, surface EMG is still useful. In particular, the occurrence of multiple-channel and even high-density surface EMG has enhanced the application of surface EMG. High-density surface EMG produces a spatially filtered EMG channel that can have sufficient resolution to identify individual MUAPs. It is especially applied to observe the conduction velocity of MUAPs to better understand and analyze the mechanism of muscle fatigue [Farina and Roberto, 2000] [Merletti et al., 2008] [Holobar et al., 2009].

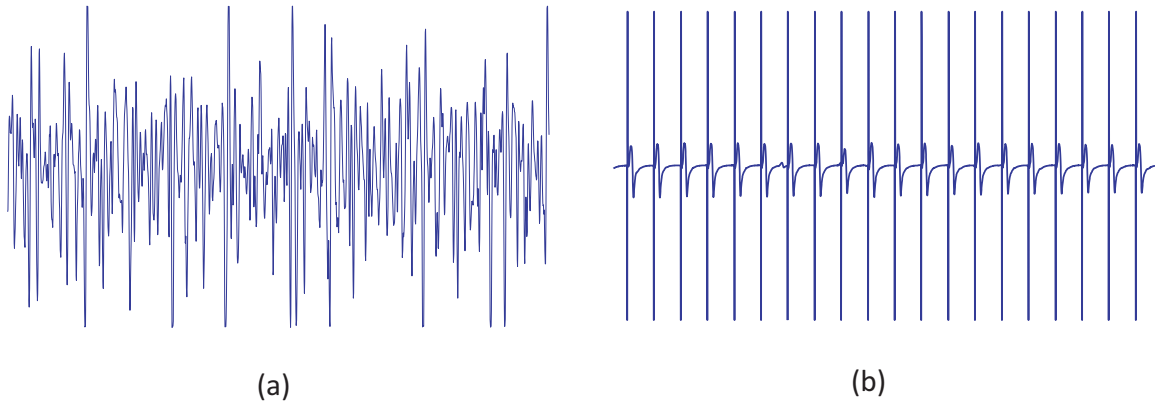

FIGURE 3.1: (a) Voluntary EMG signals represent asynchronous muscle activity; and (b) FES-evoked EMG signals consist of artifacts and Mwave. The Mwave is the summation of recruited MUAPs. It represents synchronous muscle activity compared with voluntary muscle contraction.

The EMG signal is a summation of the recruited MUAPs. Typical EMG signals from voluntary contraction and from FES-evoked muscle contraction are shown in Fig. 3.1. The active motor units during voluntary contraction have different firing frequencies and behave asynchronously, showing the so-called interference pattern. In contrast, the motor units with electrical stimulation have synchronous activity, showing the so-called Mwave in the EMG signal. When processing the FES-evoked EMG signals, one has to deal with stimulation artifacts, which appear at the onset of each stimulation impulse and are quite larger than Mwave. In order to retrieve the signal of interest, Mwave, suitable techniques should be employed to remove the stimulation artifacts. As seen from Fig. 3.1, the EMG signal is a complex spiky signal that is difficult to interpret. The various techniques generally represent either time-domain or frequency domain properties of EMG signals, as described in [Cifrek et al., 2009].

3.2 State of the Art in Muscle Fatigue study in FES

Muscle fatigue is not easy to effectively reduce despite the attempts to address this problem. Another meaningful study is how to detect fatigue and predict force production when muscle has been fatigued by stimulation. First, objective fatigue monitoring is especially important in paraplegic patients, who suffer from a lack of sensory feedback from their paralyzed

muscles, because it can be used to readjust stimulation to prevent failure. Second, force prediction is essential if the muscle force has to be used as feedback in closed-loop stimulation.

Various fatigue models have been established, based on physiological and mathematical interpretation or fitting from experimental measurements. A biomechanical model was developed to predict the shank motion induced by FES [Riener et al., 1996]. A five-element musculotendon model was developed to predict the force generation capacity of the activated muscle, and a fatigue recovery function, based on the metabolic profile, was introduced [Mizrahi et al., 1997b]. In [Cai et al., 2010], a Wiener-Hammerstein model was proposed to predict FES-induced muscle force in unfatigued and fatigued muscle, and this work was verified by stimulating Soleus in SCI patients. A computer model of activation dynamics was developed to interpret FES-induced muscle fatigue in [Lim et al., 2000]. It represented the reduction in muscle force and fatigue recovery from intermittent stimulation.

Some researchers have attempted to predict force/torque variations with fatigue based on evoked Electromyography (eEMG). An exponential function was proposed to predict force of the FES-activated quadriceps muscles from eEMG Peak-to-Peak (PTP) [Mizrahi et al., 1994b]. PTP was suggested as a fatigue index during constant cycling speed in [Chen and Yu, 1997]. A high correlation between EMG Mean Absolute Value (MAV) and knee torque was found under continuous stimulation in paraplegic subjects [Erfanian et al., 1996]. In their following work [Erfanian et al., 1998], they proposed a predictive model of muscle force production under an isometric percutaneous continuous FES system. After comparing the performance of force prediction from stimulation and from EMG, they suggested using measured EMG signals instead of stimulation signals to predict muscle torque. A metabolic model was presented to predict the force decline and recovery from EMG signals under intermittent condition [Levin and Mizrahi, 1999]. Second Phase Area (SPA) and Root Mean Squares (RMS) were suggested to monitor activation over a long fatigue period during isometric continuous stimulation in [Heasman et al., 2000].

All of these works suggest that EMG could be used to monitor the muscle fatigue during electrical stimulation. However, as [Mizrahi et al., 1994a] pointed out, the EMG-to-force relationship could be affected by different recruitment levels and muscle recovery in time-domain analysis.

Decreases in time-domain parameters (integrated sEMG, MAV, PTP and RMS) and frequency-domain parameters (Power Spectral Density (PSD), Mean Frequency (MNF) and Median Frequency (MDF)) with decreased force due to muscle fatigue were observed in [Tepavac and Schwirtlich, 1997]. They suggested combining time-domain parameters and frequency-domain parameters to track muscle fatigue. A simple combination was implemented to validate this proposal and showed some improvement in force prediction, but the accuracy was still far from the requirements for practical use. In [Mizrahi et al., 1997a], the authors reported that both MDF and Total Spectral Power (TSP) decreased with fatigue and were fit by an exponential function over time. However, when muscle fatigue increased, an extremely low correlation was found between force and MDF in one of the subjects. In another work [Chesler and Durfee, 1997], the authors attempted to track fatigue from RMS and MNF. Unfortunately, the results demonstrated that it is difficult to reliably track fatigue for practical FES applications.

In [Ziai and Menon, 2011], retraining the model was suggested to regain high estimation quality due to degraded estimation accuracy over time. Therefore, the online estimation method proposed in this work is preferable to characterize the muscle contraction dynamics for real-time FES control. However, the fatigue properties vary at different fatigue levels and recovery processes, which complicates the identification of a fatigue model. The fatigue model cannot work when the desired stimulation pattern is unknown in advance. The time-variant EMG-to-force relationship also challenges the identification method and the reliability of force prediction from EMG information.

3.2.1 Problem Formulation

Muscle fatigue is a complex phenomenon, and it is often a combination of excitation, contractile and ischemic fatigue [Erfanian et al., 1994]. Muscle fatigue is hence considered as a protocol-specific, muscle-specific, task-specific, and even subject-specific phenomenon. In addition, most Spinal Cord Injury (SCI) patients cannot perceive muscle fatigue as FES proceeds. Generally, the therapists manually adjust the stimulation pattern when they observe fatigue from the decay of motion performances in practice. In this context, accurate muscle force/torque information is important for FES control that adapts to the muscle variations.

3.3 Modeling of the Electrically Stimulated Muscle

On the basis of pioneering work [Erfanian et al., 1998], this work takes advantage of the eEMG signal from the stimulated muscle for torque prediction and the subsequent torque control. A Hammerstein with eEMG as the model input is adopted to correlate with the joint torque under isometric condition. In this context, the first problem is how eEMG relates to the torque generation that alters with muscle fatigue during different stimulation conditions.

3.3.1 Model Structure

A Hammerstein structure consists of a memoryless nonlinearity followed by a time-variant linear subsystem. In biomechanical modeling, it has been used to model the stretch reflex EMG signal [Dempsey and Westwick, 2004], and it has been shown to extend to dynamic conditions [Farahat and Herr, 2005], which is essential for developing stable adaptive controllers for future dynamic movement production.

It has been popularly applied to model the muscle contraction system in isometric condition because its nonlinearity represents the motor unit recruitment characteristics, and all the muscle dynamics are assumed to be linear [Riener, 1999]. These components are shown in Fig. 3.2.

To model muscle electrical-mechanical behavior, the eEMG signal from stimulated muscle and the isometric torque are considered as system input u(t) and output y(t), respectively, as [Erfanian et al., 1998] proposed. The memoryless nonlinear function maps the system input u(t), to the intermediate variable h(t), which represents the activation level of the stimulated muscle. It is traditionally modeled by an nth-order polynomial of u(t)

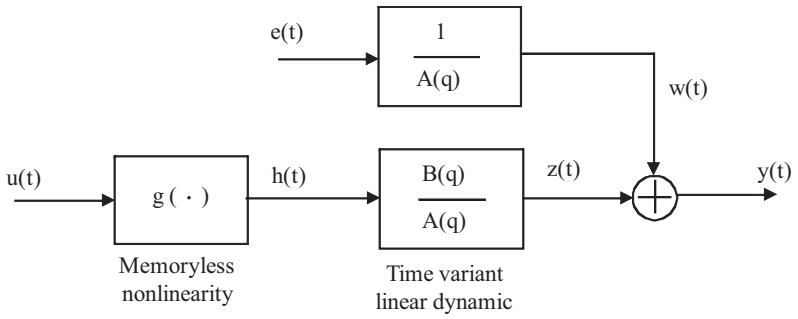

FIGURE 3.2: Hammerstein model structure.

[Dempsey and Westwick, 2004] as follows:

$$h(t) = g(u(t)) = \sum_{i=1}^{n} \gamma_i u^i(t) \tag{3.1}$$

where n is the polynomial order.

The linear time-variant system is described by an Autoregressive with External Input (ARX), which has been shown experimentally to yield good prediction of output torque/force in isometric situation [Bernotas et al., 1986]. It can be described as:

$$A(q)y(t) = B(q)h(t) + e(t) \tag{3.2}$$

where $A(q)$ and $B(q)$ are polynomials in the backward shift operator, q^{-1}, given by,

$$\begin{aligned} A(q) &= 1 + a_1 q^{-1} + a_2 q^{-2} + \cdots + a_l q^{-l} \\ B(q) &= b_1 q^{-1} + b_2 q^{-2} + \cdots + b_m q^{-m} \end{aligned} \tag{3.3}$$

where q^{-1} makes $q^{-1}y(t) = y(t-1)$, with l and m being the maximum time delay for the numerator and denominator dynamics, respectively. Term e(t) is zero mean and Gaussian white noise, which corrupts system (model) output and is statistically independent of h(t). Note that the h(t) is the output of the nonlinear element, and the input of the linear element as seen in Fig. 3.2. Dividing both sides of (3.2) by A(q) produces

$$y(t) = \frac{B(q)}{A(q)} h(t) + \frac{1}{A(q)} e(t) \tag{3.4}$$

The linear model and noise model thus have the same poles, with transfer function B(q)/A(q) and 1/A(q), respectively, as shown in Fig. 3.2. Next, substituting (3.1) and (3.3) into (3.2), the Polynomial Hammerstein Model (PHM) is parameterized by

$$\begin{aligned} y(t) =& f(u(t-i), y(t-i), \theta) \\ =& \sum_{i=1}^{l} a_i y(t-i) + \sum_{i=1}^{m} \sum_{j=1}^{n} \mu_{ij} (u(t-i))^j \end{aligned} \tag{3.5}$$

coefficient $\mu_{ij} = b_i \gamma_j$. The stimulated muscle model has $l + m \times n$ unknown parameters in all, which are contained in parameter vector θ. If we care about how torque and eEMG change with

fatigue, we can observe the changes of parameters in $\theta = [\theta_t \ \theta_e]$, where $\theta_t = [a_1 \ a_2 \ \cdots \ a_l]$ are the coefficients of the past system output and $\theta_e = [\mu_{11} \ \mu_{12} \ \cdots \ \mu_{21} \cdots \ \mu_{mn}]$ are the coefficients of the past system input.

The structure in (3.5) implies that the current output $\hat{y}(t)$ is predicted as a weighted sum of past output values plus past input values. The value of past torque y(t-i) has two versions — past measured torque $y_m(t-i)$ and past predicted torque $\hat{y}_p(t-i)$. When model identification is performed, the past measured torque is preferred, as the measurement represents the model output. For model validation, both can be employed, whereas from a practical point of view, the cross-validation based on predicted torque is more convincing to verify the model suitability for different data. Accordingly, two possible calculations of the past torque in (3.5) lead to two corresponding predicted output forms — $\hat{y}_m(t)$ and $\hat{y}_p(t)$, which are computed as a function of past measured eEMG, past measured torque or past predicted torque in this way:

$$\hat{y}_m(t|t-1) = f(u(t-i), y_m(t-i), \theta) \tag{3.6}$$

$$\hat{y}_p(t|t-1) = f(u(t-i), \hat{y}_p(t-i), \theta) \tag{3.7}$$

The second approach shown in (3.7) only uses measured eEMG signals to predict future torque, which implies the use of eEMG as a synthetic torque sensor for torque estimation when torque measurement is not available [Erfanian et al., 1998]. In this case, the predicted torque can be initialized at zero, $\hat{y}_p(0) = 0$, when no stimulation is delivered to the muscle.

3.3.2 Model Complexity Identification

The size of parameter vector θ in (3.5), depending on model complexity, needs to be identified. Increasing model complexity will decrease systematic error but increase the system variability [Ljung, 1999]. Therefore, the selection of model order (l,m,n) is a key step in the identification of the unknown parameters in θ. The nonlinearity — that is, the recruitment curve of the muscle — is modeled as a 3rd-order polynomial of instantaneous eEMG; that is, (n=3), as suggested in [Chia et al., 1991]. Linear model order is determined by comparing the Rissanen's Minimum Description Length (MDL) [Rissanen, 1978] obtained for different model order options, since the MDL principle provides a criterion for tradeoff between the simplicity of the model and the model's applicability to the data. The MDL is defined by the following equation under the hypothesis of Gaussian disturbances.

$$MDL = V * (1 + d * \frac{ln(N)}{N}) \tag{3.8}$$

where $d = dim(\theta)$ is the number of identified parameters, N is the length of data samples for this identification, and V is the loss function given by

$$V = \frac{1}{2} \ \epsilon^T(\hat{\theta}(k), k) \ \epsilon(\hat{\theta}(k), k)$$

where ϵ is a N-by-1 vector of the residuals between measurements and model estimates and $\hat{\theta}(k)$ is the identified model parameter at instant k. Using MDL to perform a relative comparison of the different model complexities, the smaller value of MDL indicates a better model.

3.4 Experimental Methods

3.4.1 Experimental Setup

FIGURE 3.3: Experimental set-up for electrical stimulation and EMG, torque acquisition.

The experiments of surface FES were conducted on five SCI subjects in the Propara Rehabilitation Center, Montpellier, France. All subjects were classified as American Spinal Injury Association (ASIA) A at different injury levels (see TABLE 3.1). The experimental set-up is depicted in Fig. 3.3. This study was approved by the ethical committee for person's protection of Nîmes, and all subjects signed informed consent forms.

TABLE 3.1: Patient configurations

subject	Age (years)	Weight (kg)	Height (cm)	Level of injury	Months post injury
S1(M)	39	50	169	T6	3
S2	22	54	172	C7	30
S3	26	64	192	T6	36
S4	32	61.5	177	C5	8
S5	48	76	177	T6	18

The subjects were seated on the chair with the ankle at 90^o, while the joint center was aligned with the axis of a calibrated dynamometer (Biodex 3, Shirley Corp., NY, USA). The shank was adjusted to be horizontal to the ground with the knee joint at approximately 40^o. The foot was strapped to the pedal to transmit ankle torque to the dynamometer, and to allow the optimal recording of isometric ankle torque. Electrical current pulses were delivered to the right Triceps Surae muscle group via surface electrodes (10 cm $\times$ 3 cm) to induce muscle contractions and to plantarflex the ankle joint as a result. One electrode was placed 5 cm beneath the popliteal cavity and the other beneath the insertion point of the Medial and Lateral Gastrocnemius

on the Achilles tendon. The muscle group was stimulated with amplitude modulation at a constant frequency (30 Hz) and constant Pulse Width (PW) (450 μs), under isometric condition, by a portable stimulator (Cefar physio 4, Cefar Medical, Lund, Sweden).

Evoked EMG activity of the soleus in the Triceps Surae muscle group was collected, amplified (gain 1000) by a bipolar differential amplifier (Biopac MP 100 Biopac Systems Inc., Santa Barbara, CA, USA), and sampled at 4 kHz. The bipolar Ag/AgCl EMG electrodes were positioned over the muscle belly in the direction of the muscle fiber with 20 mm interelectrode spacing. The reference electrode was placed on the patella of the other leg. Isometric ankle plantarflexion torque was measured using the dynamometer (Biodex 3), sampled at 2 kHz.

3.4.2 Experimental Protocol

The maximum stimulation amplitude (I_{max}) was found for each subject at the beginning, by gradually increasing stimulation amplitude until torque arrived at saturation. For each subject, the experiment consisted of three test sessions, as shown in Fig. 3.4.

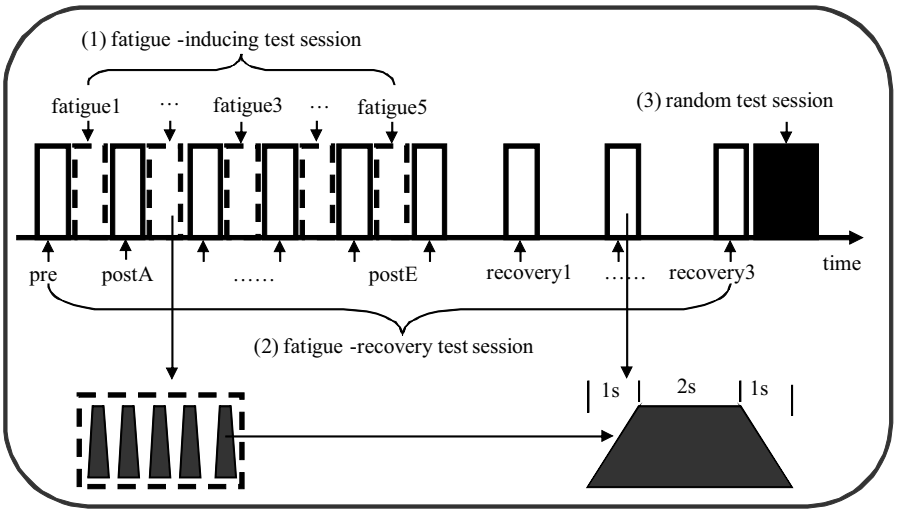

FIGURE 3.4: Schematic representation of the experimental sessions.

1. The fatigue-inducing session consists of several sequences (called fatigue1-fatigue5). Each sequence contains five trapezoidal trains with each trapezoidal train consisting of 4 s of stimulation (1-s ramp-up, 2-s plateau and 1-s ramp-down) and 2 s of rest. The stimulation amplitude during the plateau is chosen at 50% of the I_{max} with 30 Hz, 450 μs. In order to induce muscle fatigue, three such stimulation sequences are applied to subjects S1 and S2, four sequences to S3, and five sequences to S4 and S5.

2. The fatigue-recovery session consists of one trapezoidal train at I_{max}, which is delivered to the muscle just before and after each fatigue-inducing sequence. After the stimulation train postE, the same stimulation train is applied every 5 minutes, up to 15 minutes.

3. The random session delivered one stimulation sequence including several trapezoidal trains to the muscle. In this case, the stimulation amplitude in each train is increased

from zero to a randomly determined value ($\leq I_{max}$) and is then symmetrically decreased over two minutes in total.

3.4.3 Evoked EMG Signal Processing

Unlike in voluntary muscle contraction, artificially recruited motor units depolarize synchronously. Consequently, the eEMG is a synchronous summation of the recruited MUAPs, the so-called Mwave. Moreover, the surface eEMG signals are contaminated by stimulation artifacts which have quite larger magnitude than eEMG signals. Several works have proposed to remove the stimulation artifacts by software method [Sennels et al., 1997], hardware method [Erfanian et al., 1998] or both [Chesler and Durfee, 1997]. The blanking window or blanking circuit is useful as long as the Mwave is not overlapped with stimulation artifacts. Once the experimental setup is fixed for one subject, the duration of the stimulation artifacts is almost constant. Thus, we can estimate the duration of artifacts T_{arf} by pre-experiment. The software blanking window suppresses the stimulation artifacts by making the recording signal zero during T_{arf}. Various EMG variables can be used to represent EMG characteristics. MAV, a moving averageöf full-wave rectified EMG, is chosen in this work.

$$MAV = \frac{1}{T}\int_0^T |x(t)|dt \tag{3.9}$$

MAV is computed by (3.9), where x(t) is the eEMG signal at time t, and T is the length of data being used for calculation. Briefly, the collected eEMG and torque data are processed as following steps.

1. The stimulation artifact is removed from the raw eEMG signals by the blanking window method [Frigo et al., 2000], and the Mwave is consequently extracted.

2. The measured torque is offset with respect to the torque baseline to obtain the torque level. The torque baseline is the torque measurement when the muscle is at rest.

3. A lowpass filter is applied to the measured ankle torque (6th-order, cutoff frequency 100 Hz) and the measured eEMG (6th-order, cutoff frequency 300 Hz).

4. The filtered eEMG signals are divided into epochs with each epoch containing one Mwave, and the MAV of eEMG is calculated within five epochs. The average torque is calculated within the same time window.

5. The MAV and average torque are normalized with respect to their maximum values.

An example of the processed results is illustrated in Fig. 3.5, where T_{arf} =3 ms. Note that the normalized MAV of eEMG and normalized torque are prepared as system input and output.

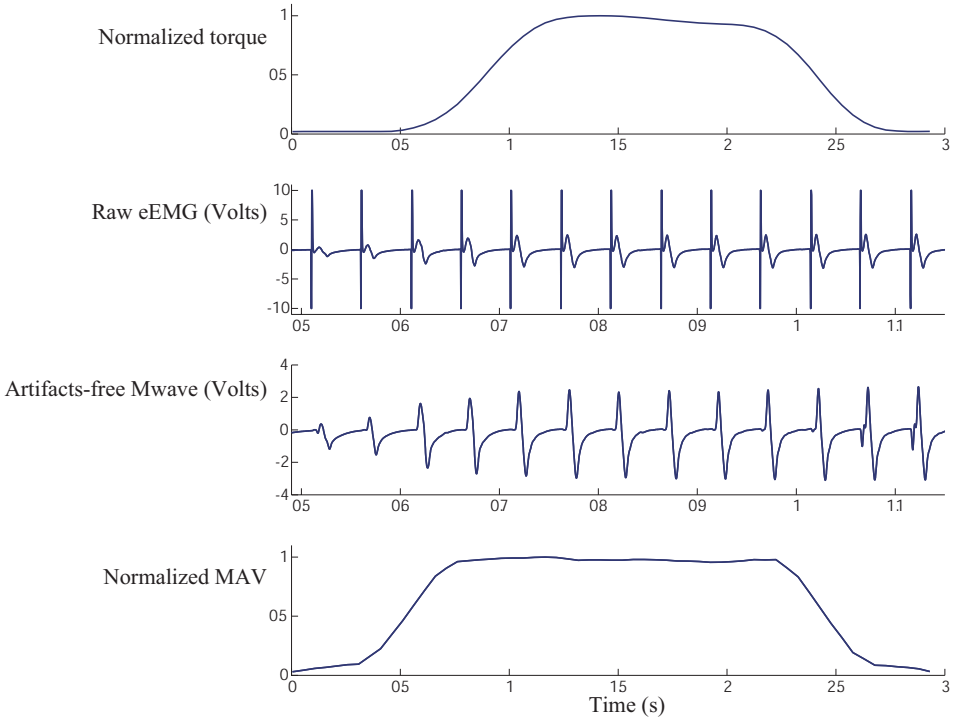

FIGURE 3.5: An example of processed eEMG and torque. The raw eEMG signal and Mwave are zoomed in (0.5 s $\sim$ 1.15 s) to show the details during stimulation increase. The raw eEMG was contaminated by stimulation artifacts. The blanking window is applied to remove artifacts so that the Mwave is effectively extracted. Note that the magnitudes of raw EMG and Mwave are quite different.

3.5 Results in Surface FES

3.5.1 Muscle Fatigue and Recovery Characteristics

In intermittent FES, the rest period is important to reduce muscle fatigue, and it is more practical when continuous stimulation is not necessary for a single muscle, such as walking. The muscle fatigue is represented as torque decline with the same stimulation. For example, the torque decrease over time in subject S3 is demonstrated in Fig. 3.6. Joint torque declines 19% of initial torque with 151 s of stimulation within 191 s of intermittent stimulation. We confirmed that the different fatigue behaviors of the subjects match the assumption that fatigue dynamics are subject-specific. Even for the same subject, the eEMG-to-torque relationship gradually varies over time, rather than remaining constant.

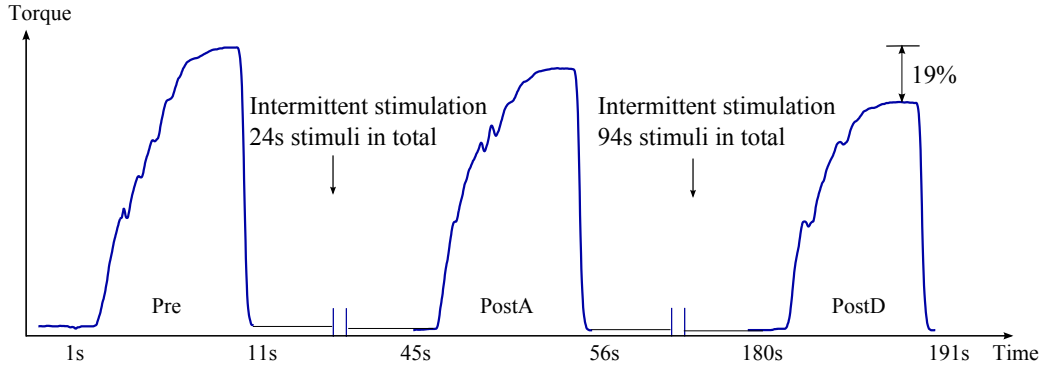

FIGURE 3.6: Demonstration of FES-induced muscle fatigue in subject S3. Joint torque declines 19% of initial torque with 151 s of stimulation within 191 s of intermittent stimulation.

3.5.2 Model Identification and Prediction

Before model identification, the model order is determined as described in Section 3.3.2. The nonlinear model order is fixed at 3, and the model order of the linear ARX model is identified using processed eEMG and torque data by comparing MDL values at different model-order options. Model order ranging from $2 \leq l \leq 6$, and from $2 \leq m \leq 6$ are considered. The MDL values for all five subjects in the fatigue-inducing test are shown in Fig. 3.7. Ultimately, model order $(l = 3, m = 4)$ was chosen with relatively less MDL value and a simpler model, and this choice is used for all subsequent analysis relating to this experiment.

Fig. 3.8 illustrates the prediction result in subject S5. The randomly modulated stimulation PW results in random muscle response, which is more realistic when performing some complex movements. Furthermore, the random FES protocol has never been investigated for fatigue analysis in previous works. Therefore, it is vital to predict torque levels from the eEMG signal for fatigue tracking. In Fig. 3.8, the torque reproduction before 68 s has high quality with available eEMG and torque measurements, and the prediction is still good (7.13% Normalized Root Mean Squares (NRMS) error) in the last 30 s prediction without using torque measurement.

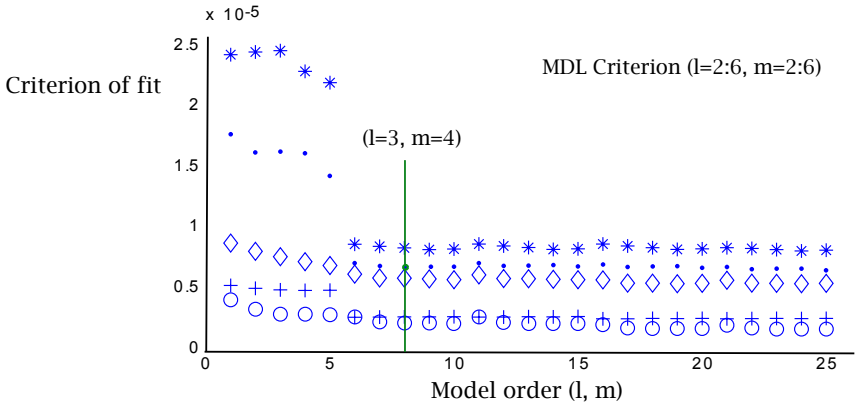

FIGURE 3.7: Criterion of fit for determining appropriate model complexity. '·'---S1, '*'---S2, 'o'---S3, '◇'---S4, '+'---S5. The vertical line indicates the selected model order $(3, 4)$.

3.6 Online Torque Prediction during Muscle Fatigue

This finding in previous sections indicates that the relationship between eEMG and torque is time-variant, and the parameters of the eEMG-to-torque model should be updated adaptively when eEMG is used to predict torque. In the proposed formulation, Kalman Filter (KF) is used for the online parameter identification of the muscle contraction model. KF is efficient for estimating the internal states and parameters of a discrete-time system from a series of noisy measurements.

3.6.1 State-Space Representation and Filter Configuration

State-space representation is basically required to implement the recursive algorithm for model estimation. It provides a convenient and compact way for estimation and control problems with its notational expression. The state-space form relates a set of input, output, and state variables by first-order differential equations, and permits us to track the internal state variables from input-output data sets, whether they are measurable or not.

Considering a time-variant PHM (l,m,n) as described in (3.5),

$$f(u(k-i), y(k-i), \theta(k)) = \sum_{i=1}^{l} a_i(k) y(k-i) + \sum_{i=1}^{m} \sum_{j=0}^{n} \mu_{ij}(k)(u(k-i))^j, \tag{3.10}$$

$\theta(k)$ is the vector containing the time-variant model parameters:

$$\theta(k) = [a_1(k), \cdots, a_l(k), \mu_{11}(k), \cdots, \mu_{1n}(k), \cdots, \mu_{m1}(k), \cdots, \mu_{mn}(k)]^T. \tag{3.11}$$

Consequently, a PHM (l,m,n) has (l+m*n) parameters. At a given time instant t, the computation of future joint torque estimates using (3.10) is straightforward, assuming a stationary or slowing varying system within the prediction horizon. Next, we will describe the chosen parameter model, the state space representation, and the measurement model.

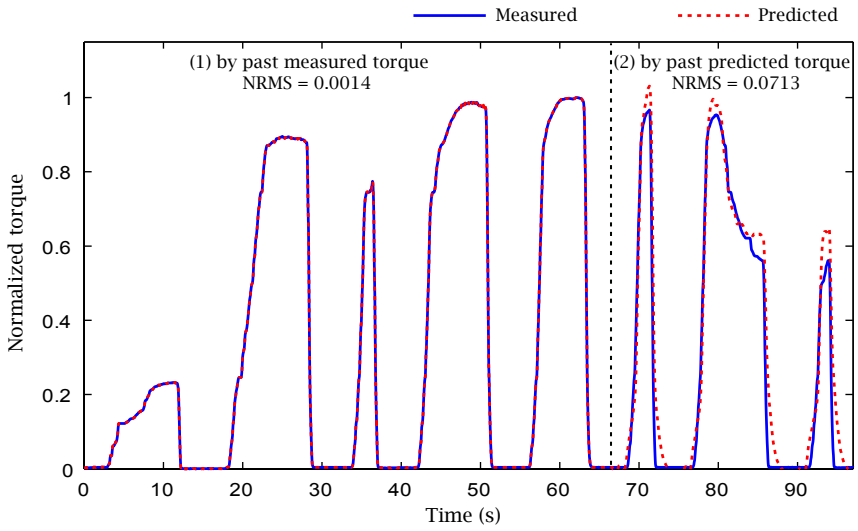

FIGURE 3.8: The measured and predicted torque obtained by the eEMG-to-torque model in the random test of sub S5. (1) The torque is predicted based on the past measured MAV of eEMG and past measured torque. (2) The torque is predicted based on the past measured MAV of eEMG and past predicted torque, with initial predicted torque at zero.

Parameter model

In a time-varying muscle contraction model, if indicative information about the evolution in muscle fatigue is available–for instance, the fatigue rate is indicated by eEMG amplitude or frequency components–the model parameters can be easily modeled by incorporating into (3.12). Otherwise, the changes in model parameters are considered absolutely random, and the parameters are represented by a random walk process,

$$\theta(k) = \theta(k-1) + \varepsilon(k) \tag{3.12}$$

where k indicates the current time step and $\theta(k)$ is the kth-step parameters. The parameter transition is assumed to be Gaussian white noise ε, $\varepsilon \sim N(0, \sigma^2)$. This implies that the mean of the parameter process is constant, but its variance is not constant. Thus, the parameter model is non-stationary, and the variance is variant with time. In practice, this model structure makes the prediction process very simple since all the future values of $\theta(k+s)$ for $s > 0$ are assumed to be equal to $\theta(k)$ and the variance is set according to the system dynamics. For example, if the variation in torque is considered higher in comparison with the variation in eEMG with an increase in muscle fatigue level, the coefficients of past torque $a_i(k)$ should be set relatively higher than the coefficients of past eEMG $\mu_{ij}(k)$. In other words, we assume more uncertainty concerning muscle mechanical behavior than muscle electrical behavior with increasing fatigue.

Process and measurement models

A state-space model consists of a measurement model relating the observations to the state vector, and a Markovian transition equation describing the evolution in the state vector over

time. For a PHM (l,m,n), the state vector, which consists of q=max(l,m) variables, is given by

$$\mathbf{x}(k) = \begin{bmatrix} x_1(k) & x_2(k) & \cdots & x_q(k) \end{bmatrix}^T \tag{3.13}$$

The previous state $\mathbf{x}(k-1)$ is transferred to the current state $\mathbf{x}(k)$ by a transfer matrix $\mathbf{A}(k) \in \mathbb{R}^{q \times q}$, such that

$$\mathbf{x}(k) = \underbrace{\mathbf{A}(k)\mathbf{x}(k-1) + \mathbf{B}(k)\mathbf{u}(k-1) + \mathbf{w}(k)}_{\mathbf{f}(\mathbf{x}(k-1), \mathbf{u}(k-1), \mathbf{w}(k))} \tag{3.14}$$

$$\mathbf{u}(k-1) = \begin{bmatrix} u(k-1) \\ u(k-1)^2 \\ \vdots \\ u(k-1)^n \end{bmatrix} \tag{3.15}$$

where $\mathbf{u}(k-1) \in \mathbb{R}^{n \times 1}$ contains the exponents of previous model inputs, which are known at each current step. Vector $\mathbf{w}(k)$ is Gaussian white noise of the system model. $\mathbf{B}(k) \in \mathbb{R}^{q \times n}$ relates the previous model input $\mathbf{u}(k-1)$ to the current state $\mathbf{x}(k)$.

As for the measurement model, it relies only on the first state element $x_1(k)$, being written in vector expression as

$$y(k) = \mathbf{C}\mathbf{x}(k) + v(k), \tag{3.16}$$

where v(k) is Gaussian white noise of the measurement sensor. When the system has a single output, the observer is scaler variable y; otherwise, it is a vector and the corresponding noise element is also with vector expression. The current state $\mathbf{x}(k)$ is correlated with the current system output y(k) by measurement matrix $\mathbf{C} \in \mathbb{R}^{1 \times q}$

$$\mathbf{C} = \begin{bmatrix} 1 & 0 & \cdots & 0 & 0 \end{bmatrix}.$$

In the prediction phase of KF, the evolution in the model states is given by (3.14), while the evolution in the model parameters is given by (3.12). In the correction phase, the measurement from output sensor, y(k), will be applied to update the estimates of model states and model parameters.

3.6.2 Kalman Filter with Forgetting Factor

In order to identify the time-variant model states in $\mathbf{x}(k)$ and the parameters in $\theta(k)$, even though a dual KF is a solution to identify them in two parallel KF, as described in [Aboy et al., 2005], another treatment is more direct and convenient for this purpose and is used in this work. The main idea is to identify the model states and the model parameters concurrently by regarding the unknown model parameters as elements of the state vector. In this way, the basic KF algorithm does not need to be modified, except that the state vector $\mathbf{x}(k)$ will be augmented with the unknown parameters in $\theta(k)$. That is, the meta-state vector $\mathbf{\Theta}(k)$ is given by

$$\mathbf{\Theta}(k) = \begin{bmatrix} \mathbf{x}(k) \\ \theta(k) \end{bmatrix}_{[(q+l+m\times n)\times 1]} \tag{3.17}$$

Accordingly, from equation (3.12) (3.14) and (3.16), the augmented system is rewritten by

$$\boldsymbol{\Theta}(k) = \underbrace{\begin{bmatrix} \mathbf{f}(\mathbf{x}(k-1), \mathbf{u}(k-1), \mathbf{w}(k)) \\ \theta(k-1) + \boldsymbol{\varepsilon}(k) \end{bmatrix}}_{\mathbf{F}(\boldsymbol{\Theta}(k-1), \mathbf{u}(k-1), \boldsymbol{\nu}(k))} \tag{3.18}$$

$$y(k) = \underbrace{\begin{bmatrix} \mathbf{C} & \mathbf{0}_{1\times(l+m\times n)} \end{bmatrix} \boldsymbol{\Theta}(k) + v(k)}_{\mathbf{G}(\boldsymbol{\Theta}(k), v(k))} \tag{3.19}$$

where the process noise $\mathbf{w}(k)$, the parameter noise $\boldsymbol{\varepsilon}(k)$ and the measurement noise $v(k)$ are the same as shown in (3.12) (3.14) and (3.16). They are assumed to be independent, white and normally distributed,

$$\boldsymbol{\nu}(k) = \begin{bmatrix} \mathbf{w}(k) \\ \boldsymbol{\varepsilon}(k) \end{bmatrix}$$

$$p(\boldsymbol{\nu}) \sim (0, \mathbf{Q}) \tag{3.20}$$

$$p(v) \sim (0, R) \tag{3.21}$$

The recursive algorithm of KF is a mature technique that consists of two phases, prediction and correction. In the prediction phase, the system is assumed to be stationary, which implies the *a priori* estimate of the state at instant k, $\hat{\boldsymbol{\Theta}}^{-}(k)$, is equal to the *a posteriori* state at the previous instant k-1, $\hat{\boldsymbol{\Theta}}(k-1)$,

$$\hat{\boldsymbol{\Theta}}^{-}(k) = \mathbf{F}(\hat{\boldsymbol{\Theta}}(k-1), \mathbf{u}(k-1), 0) \tag{3.22}$$

The estimate error covariance $\mathbf{P}(k)$ is propagated according to (3.23):

$$\mathbf{P}^{-}(k) = \mathbf{D}(k)\mathbf{P}(k-1)\mathbf{D}^{T}(k) + \mathbf{Q}(k-1) \tag{3.23}$$

where $\mathbf{Q}(k-1)$ is a diagonal matrix containing the process noise covariance, and $\mathbf{D}(k)$ is the Jacobian matrix of partial derivations of process transfer function $\mathbf{F}$ with respect to the variables involved in $\boldsymbol{\Theta}$, with each element D_{ij} being computed by:

$$D_{ij}(k) = \frac{\partial F_i}{\partial \Theta_j}(\hat{\boldsymbol{\Theta}}(k-1), \mathbf{u}(k-1), 0) \tag{3.24}$$

In the correction phase, $\mathbf{K}(k)$ in (3.25) is called a KF gain that minimizes the *a posteriori* error covariance,

$$\mathbf{K}(k) = \mathbf{P}^{-}(k)\mathbf{H}^{T}(k)(\mathbf{H}(k)\mathbf{P}^{-}(k)\mathbf{H}^{T}(k) + R(k))^{-1} \tag{3.25}$$

where R(k) is a scalar measurement noise covariance (for a single output system). $\mathbf{H}(k)$ is the Jacobian matrix of partial derivations of sensor transfer function $\mathbf{G}$ with respect to $\boldsymbol{\Theta}$, with each element H_{ij} being computed by:

$$H_{ij}(k) = \frac{\partial G_i}{\partial \Theta_j}(\hat{\boldsymbol{\Theta}}^{-}(k), 0) \tag{3.26}$$

incorporating to (3.19), $\mathbf{H}(k) = \begin{bmatrix}\mathbf{C} & \mathbf{0}_{1\times(l+m\times n)}\end{bmatrix}$.

When actual measurement y(k) is available, an *a posteriori* state estimate is generated by incorporating measurement as in (3.27). An *a posteriori* error covariance estimate is obtained via equation (3.28).

$$\hat{\mathbf{\Theta}}(k) = \hat{\mathbf{\Theta}}^{-}(k) + \mathbf{K}(k)(y(k) - \mathbf{G}(k)(\hat{\mathbf{\Theta}}^{-}(k), 0)) \tag{3.27}$$

$$\mathbf{P}(k) = (\mathbf{I} - \mathbf{K}(k)\mathbf{H}(k))\mathbf{P}^{-}(k) \tag{3.28}$$

Although the KF is an effective way of estimating the state and parameters of a discrete time-controlled process, its performance in estimating the time-varying parameters is degraded by the fact that it refers to the entire history of past measurements. This is particularly troublesome when it is used to estimate the muscle contraction system, since the activity of stimulated muscles tends to vary, with prolonged or repetitive stimulation leading to variant muscle states. In order to track the time-varying muscle condition, a forgetting factor λ is deliberately introduced to forget the old measurements when muscle fatigue increases. Consequently, (3.23) and (3.25) can be rewritten as,

$$\mathbf{P}^{-}(k) = \mathbf{D}(k)\mathbf{P}(k-1)\mathbf{D}^{T}(k)/\lambda \tag{3.29}$$

$$\mathbf{K}(k) = \mathbf{P}^{-}(k)\mathbf{H}^{T}(k)(\mathbf{H}(k)\mathbf{P}^{-}(k)\mathbf{H}^{T}(k) + \lambda)^{-1} \tag{3.30}$$

Choosing the forgetting factor $\lambda \in [0,\ 1]$ depends on how much of the old measurements we expect the filter to forget. If the forgetting factor is smaller, the filter will forget more past measurements that are farther away from the present instant. A smaller forgetting factor enables us to track changes in the system quickly, but it requires a longer time to arrive at convergence, which may lead to more fluctuations. Whereas if a forgetting factor is close to 1, it assures fast convergence but is not sensitive to the system variations. Consequently, a tradeoff between the smoothness of tracking and the lag in detecting system changes should be considered when a forgetting factor is introduced to a KF. Generally, $\lambda \in [0.9,\ 1]$ is suitable for most applications. Moreover, if a system changes slowly over time, one can select a forgetting factor close to 1.

3.7 Fatigue Tracking Based on Experimental Data

In this section, the estimation of time-varying parameters and the torque prediction for fatigue tracking are performed based on experimental data using the KF with forgetting factor.

First, to illustrate the evolution in the model parameters, the torque estimates and identification error are plotted. One result is shown in Fig. 3.9 for subject S5, where the torque declines 21%, and the estimator updates the model parameters adaptively and accurately tracks the fatigue effect. The estimation takes approximately 1 s to converge and then the identification error maintains almost less than 0.1 (corresponding to 10% of the measured torque). Notably, after a 40-s evolution, the model arrives at a steadier state, representing less than 5% identification errors. Apparently, the model parameters vary over time and generally with a low varying rate, which makes it possible to obtain good torque prediction in a given prediction horizon.

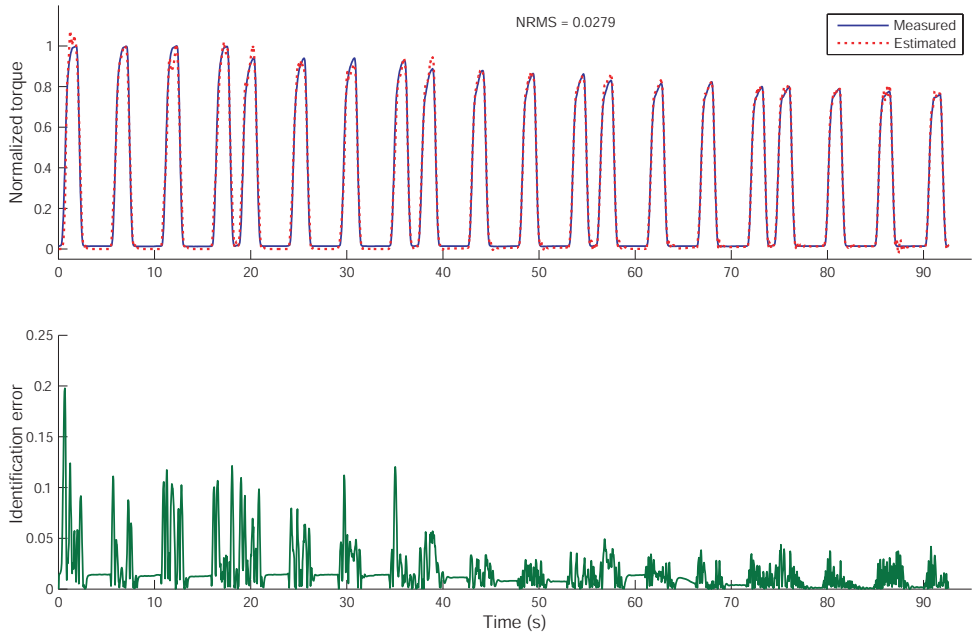

FIGURE 3.9: The estimated torque and identification error in subject S5. At each instant, the eEMG-to-torque model parameters are updated adaptively by KF with forgetting factor 0.997. The identification error of each evolution is plotted at the bottom. The identification takes approximately 1 s to converge.

3.7.1 Fatigue Dynamics

The estimation of the muscle contraction process is used to explore the dynamics of fatigue phenomena. The parameter estimates in $\hat{\theta}(k)$ are used to compute the poles of the muscle contraction system. At each evolution, a PHM (l,m,n) has l poles, and the solution is to solve a polynomial function as

$$q^l + a_1 q^{l-1} + \cdots + a_{l-1} q + a_l = 0$$

The locations of these poles in subjects S1 and S3 are indicated in Fig. 3.10. The unit circles are also plotted in this figure. All the poles are located within the unit circles, which is of significance in ensuring the model stability under such a stimulation protocol. The arrows denote the direction of movement of the z-plane poles. The time-varying property of the poles may also interpret the muscle dynamics. Moreover, the locations and movements of the z-plane poles in all subjects present similar characteristics, suggesting that it is possible to assess muscle fatigue dynamics from such information. In general, the damping ratio increases when the muscle is highly fatigued. This matches our intuition concerning the effect of muscle fatigue.

3.7.2 Torque Prediction Performance

To investigate the torque prediction performance in time, t1, t2 and t3, corresponding to 6-s, 18-s and 30-s ahead predictions, are evaluated. The torque predictions are computed using (3.10) and are only driven by the eEMG signals and identified model at t0, assuming a stationary system within the prediction horizon. At each instant, the NRMS error and Normalized

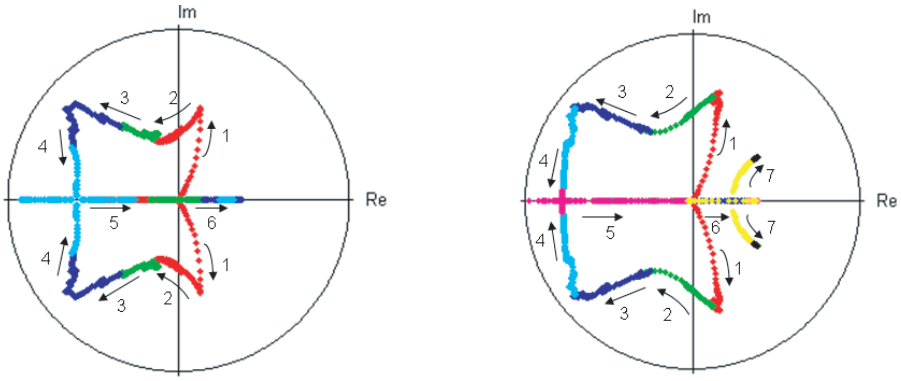

FIGURE 3.10: The changes of the muscle contraction dynamics of muscle behavior due to fatigue during surface FES in subjects S1 (left) and S3 (right). The arrows denote the direction of mmovement f the z-plane pole. The plot color is changed every 16s to show the time transition.

Peak Error (NPE) during a given prediction horizon are computed. NPE is the peak error during the prediction horizon at each evolution. The prediction errors in all subjects in surface FES are quantified in TABLE 3.2.

3.7.3 Robust Fatigue Tracking

The idea for verifying the robustness of the filter is that, assuming measurement is unavailable or unreliable from time instant t0 to t1, the identified model at t0 can be used to predict the torque induced by stimulation until instant t1. When prediction is executed, the model is only driven by the eEMG and identified model at t0, while model updating is suspended.

The measurement failure is simulated by suspending the prediction phase of KF at an arbitrary instant t0. To reestablish the tracking of muscle fatigue, the identified model at t0 is used for the prediction of torque generation for 15 s. To reveal the accuracy of the predicted torque, the measured torque is also shown for comparison. The results of two fatigue sequences in the implanted subject are illustrated in Fig. 3.11. When identification is suspended, the model parameters maintain stationary, while the torque can still be well tracked. The high tracking quality may result from the fact that the Hammerstein model is suitable to catch the muscle electrical mechanical behavior under isometric condition. Consequently, the KF is suitable to track the gradually time-varying fatigue by adaptively identifying the model.

TABLE 3.2: Prediction performance with experimental data

Subject	Average error	Prediction horizon		
		6s	18s	30s
S1	NRMS	0.0638	0.0974	0.1282
	NPE	0.1616	0.2990	0.3414
S2	NRMS	0.0763	0.0925	0.1110
	NPE	0.2466	0.3402	0.4230
S3	NRMS	0.0278	0.0314	0.0366
	NPE	0.0743	0.0962	0.1146
S4	NRMS	0.0524	0.0534	0.0556
	NPE	0.1208	0.1523	0.1697
S5	NRMS	0.0387	0.0418	0.0437
	NPE	0.1036	0.1360	0.1510

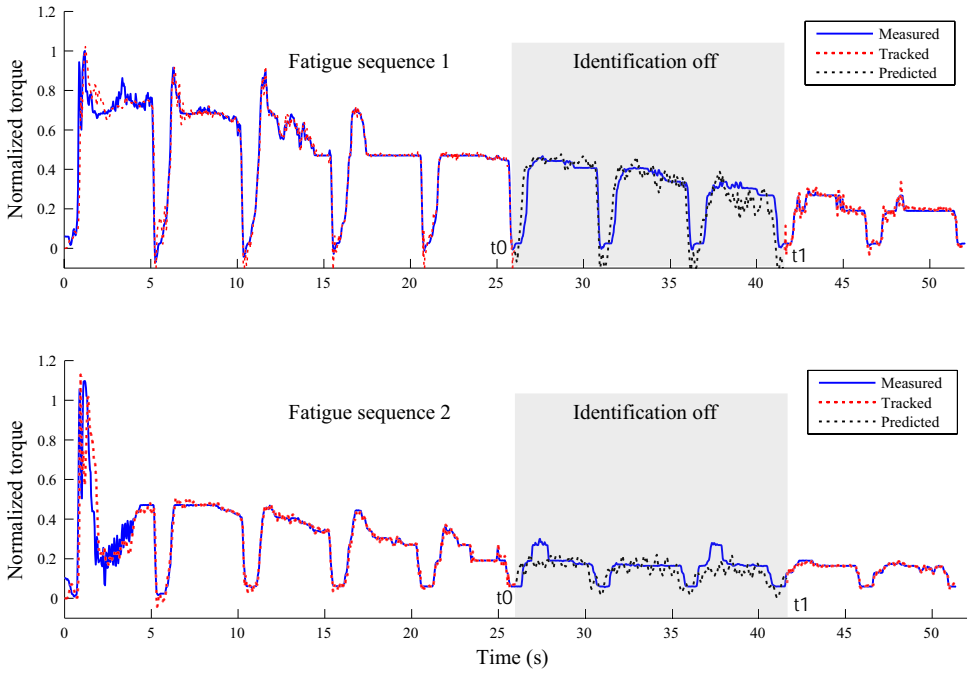

FIGURE 3.11: Robust fatigue tracking based on the eEMG-to-torque model and Kalman filter in implanted FES. The model identified at t0 is used to predict the torque from t0 to t1, where the online identification is suspended for 15 s. The forgetting factor is chosen at 0.97 to react to the fast fatigue under continuous stimulation condition.

3.8 Toward Real-time Portable Torque Prediction

In this section, we present a real-time eEMG based joint torque estimation system. Raw eEMG (M-wave) and joint torque data are acquired synchronously, and mean absolute value (MAV) of the raw eEMG is calculated per stimulation loop with moving window manner. Recursive Kalman filter (KF) is used as the online estimator for identifying MAV-to-torque relationship. Prediction results show promising performance of real-time eEMG based joint torque estimation system.

The system tests were conducted firstly on two able-bodied volunteer subject upon their consent, as a pilot study before entering a wide protocol on spinal cord injured patients (approved by Nîmes Ethics Committee, France, 2013). The system setup for the torque estimation experiment is shown in Fig. 3.12. The system consists of the wireless stimulator [Toussaint et al., 2010] as shown in Fig. 3.13, eEMG (Biopac MP100, Biopac Systems Inc., Santa Barbara, CA, USA) and torque acquisition devices (Biodex 3, Shirley Corp., NY, USA), and a laptop computer with the MATLAB interface for data processing and torque estimation. Electrical current pulses generated through the wireless stimulator were delivered to the right Tibialis (TA) muscle group with surface electrodes placed. Raw eEMG of TA muscle group and ankle joint torque were recorded, amplified (gain 1000) and sampled at a frequency $f_{samp} = 4096Hz$ by an acquisition system with a 16-bit A/D card.

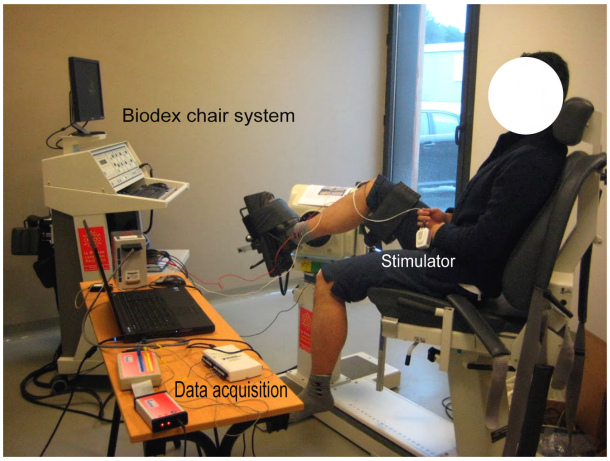

FIGURE 3.12: Experimental setup for real-time FES-induced torque estimation

The stimulation frequency was set at $f_{stim} = 40Hz$ leading to the loop execution time 25ms. The maximum pulse width (PW) of the stimulator was limited to 350μs. The suitable stimulation intensities were found to be 25mA. The test session included two phases: identification and prediction phases. Each sequence contained trapezoidal trains consisting of 2s stimulation (0.5s ramp-up, 1s plateau and 0.5s ramp-down) and 2s rest. During identification phase, the plateau stimulation PW of each trapezoidal train was increased gradually with step size of from 10% to 90% of the maximum PW. After identification, the plateau stimulation PW was randomly determined within 40% to 100% of maximum PW in the prediction phase. The real-time PW series were predefined and dispatched through MATLAB Timer object and then sent to the wireless

stimulation unit. During every loop the mean absolute value (MAV) of eEMG and mean value of torque were computed based on the $f_{samp}/f_{stim} \approx 103$ raw eEMG and raw torque sampling respectively.

FIGURE 3.13: Wireless stimulator (Left) with its control unit (Right) (Vivaltis Inc., Montpellier, France)

3.8.1 Results

We present online identification and prediction results obtained by the established real-time system. During the whole estimation process, the predefined stimulation pattern is of trapezoidal type. Fig. 3.14 shows the eEMG-based torque estimation results. In the first 20 seconds the model is undergoing identification, after time instant 20s, measured torque information is not used any more and we predict the torque purely based on eEMG with the identified model.

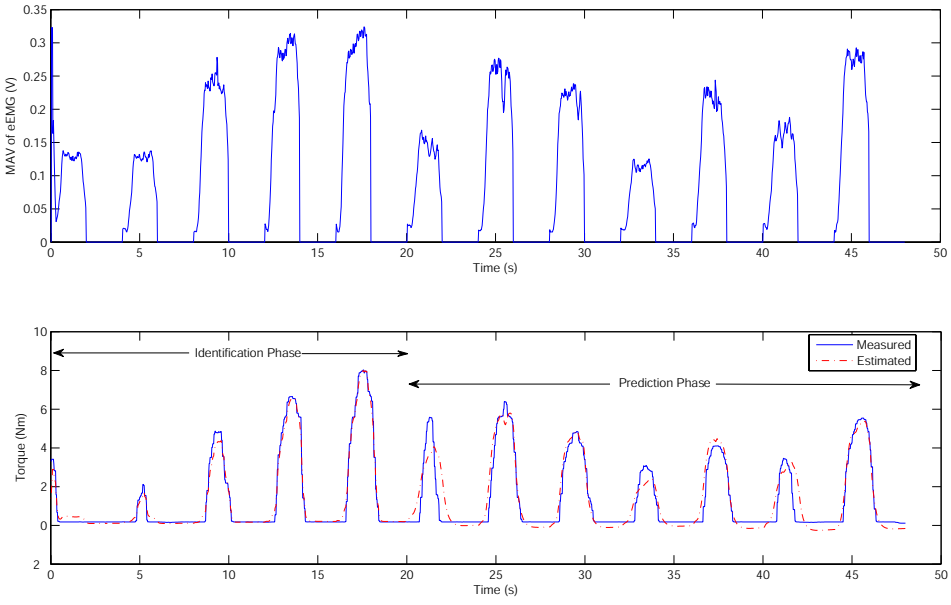

FIGURE 3.14: Real-time online eEMG based torque estimation results. Upper: MAV of the measured eEMG; Lower: corresponding estimated and measured torque containing identification and prediction phases, from $t = 20$s identification is switched off.

TABLE 3.3: Real-time torque prediction performance evaluation on one healthy subject.

Trial #	RMSE (Nm)	Normalized RMSE (%)	VAF (%)
1	1.09	13.62	89.10
2	0.63	9.00	87.61
3	0.52	0.52	87.82
4	0.75	7.42	74.13
5	0.66	9.42	67.26

Tab. 3.3 shows the aforementioned performance indexes for the prediction of the able-bodied subject with five trials. The overall average RMSE and VAF are respectively 0.73 ± 0.21 Nm and $81.14\% \pm 9.86\%$. The system's loop execution time of the every instant estimation was between 18ms and 20ms for all loops, which was not exceeding 25ms. The measure maximum torque of the subject was around 15Nm, so the RMSEs of the five trials are below 1Nm indicating accurate predictions achieved by the system.

3.9 Conclusion

The final direction of this work is to develop a model-based FES controller for muscle fatigue compensation. First step for it is to manage the joint torque prediction under FES. As FES induces fast fatigue and unexpected disturbances, whereas the patients cannot perceive the muscle fatigue, accurate torque estimation is essential to feedback muscle output for adaptive adjustment of the stimulation. We confirm that muscle contraction dynamics are time-varying with FES. A time-varying eEMG-to-torque model was employed to represent the electrical and mechanical behaviors of stimulated muscle, with the model parameters identified by a KF with forgetting factor. The predictive performance of the adaptive identification method has been validated in simulation and with experimental data. The results demonstrate sufficient adaptivity to internal muscle changes or external disturbances in a systematic way.

In terms of improvements in fatigue tracking, when the measurement of the torque sensor suffers from recording interruption or distortion, the proposed method could bridge these problems and provide sufficiently accurate fatigue tracking only on eEMG measurement. The success of torque prediction only based on eEMG is significant in FES. In addition, we may have good torque estimation ability both in surface and implanted FES (enclosed in Annex). On the basis of predicted torque, the torque can be used in a model-based predictive controller aiming at torque control. As a muscle is very slow actuator, the feedforward control is necessary and therefore, the muscle response under FES should be well predicted. Real-time implementation with wireless portable stimulator is also archieved in this chapter. The next chapter focuses on the novel FES control strategy with EMG-feedback function.

CHAPTER 4

EMG Feedback Predictive Muscle Control in FES

In this chapter, an EMG feedback predictive control is proposed as a new modality in FES control, which allows joint torque control rather than conventional position feedback control in closed-loop FES system. An FES system delivers electrical charges that are determined by a control unit to excitable motor neurons, in order to contract target muscle. The challenge in the present FES system starts with the problem of how to process the high nonlinearity and complexity of musculoskeletal systems, which complicate the model identification process. Another challenge arises from time-varying muscle dynamics due to physiological and biochemical factors (such as fatigue, reflex), as these need to be compensated in order to augment the applications of FES. Therefore, eEMG feedback, which represents muscle activity, contributes by taking the muscle state into account in the FES control system. The predictive nature facilitates the prediction of the muscle response and therefore the system can respond to the time-variant muscle state changes toward a muscle-response-aware FES control.

4.1 Control System for Movement Induced by FES

The conventional control systems for FES are illustrated in Fig. 4.1. Most current FES systems work in an open-loop paradigm (Fig. 4.1 (a)), where predefined stimulation patterns are delivered to the muscle without feedback on the real response. When the actual trajectory is not suitable for performing the desired task, the stimulation pattern cannot be accordingly adjusted. The application of an open-loop FES system is thus limited due to the degradation in performance caused by muscle state changes or other disturbances. The currently used manual FES modulation (such as a hand switch) tends to cause distraction and is thus suboptimal. Compared with open-loop control, a closed-loop controller is superior as it feeds back useful information on the current state of the system for regulating system input in accordance with the desired output. A sensor-based closed-loop control scheme is shown in Fig. 4.1 (b). It is driven by the errors between the actual trajectory and the desired trajectory. The integration of more available sensors would be beneficial to provide more useful information, but mounting, calibrating and computing the time of signal processing are complicated in implementation. In this context, the standard Proportional Integral Derivative (PID) controller and extended PID controller have been investigated. However, tuning the PID parameters to produce satisfactory tracking performance and robustness is difficult. The model-based closed-loop controller shown in Fig. 4.1 (c) is a promising means to deal with the nonlinear and time-varying characteristics of the musculoskeletal system. Model-based control techniques, such as feed-forward and predictive control strategies, require sensors and dynamic models of the system, as well. The FES control performance would thus be enhanced by a model-based controller if sufficient knowledge of the system were available.

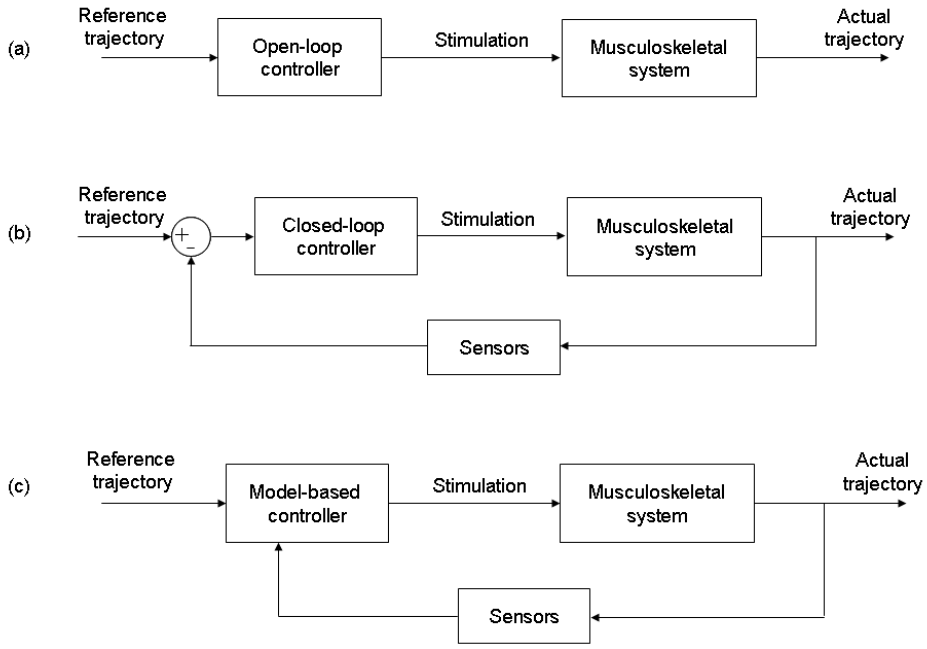

FIGURE 4.1: Organization of traditional functional electrical stimulation control systems: open-loop (a), closed-loop (b) and model-based control scheme (c) [Popović and Sinkjæ r, 2000].

4.2 Previous Works

In the current FES systems, closed-loop control has been investigated in the lab but has not been widely applied in practice. Regarding the scenario of lower limb FES closed-loop control, one goal has been to adaptively modulate the stimulation onset according to effects, such as walking speed, gait rhythm, or the intentions of users. In [Chen et al., 2001], a closed-loop FES system controlled by position sensors and triggered by a foot-switch was proposed. A micro-controller dynamically adjusting the FES intensity through a built-in algorithm was presented in [Breen et al., 2006], which was able to generate a stimulation envelope with any shape, reflecting walking speed changes. By taking advantage of EMG signals, an EMG-triggered FES control system was presented through a pattern recognition approach. In [Dutta et al., 2008], the FES system was triggered by the recognition of the patient's intention from voluntary EMG signals from incompletely paralyzed muscles.

To achieve a reliable stimulation pattern and compensate muscle property changes during FES, in [Ferrarin et al., 2001] the authors suggested using model-based approaches to achieve an efficient and robust FES system. In [Jezernik et al., 2004], a sliding model closed-loop control method was proposed to control shank movement. Another work [Ajoudani and Erfanian, 2009] combined the classic sliding model control and a neural network to control FES to track the desired knee joint trajectory. In these works, the feedback signal was based on joint motion recording. However, as muscle contraction is induced by artificial stimulation in FES, the drawback of closed-loop control of joint motion is that the resultant motion may not only derive from stimulation but also from external forces (such as environmental con-

tact). A stimulation pattern based only on motion sensors is likely to be unsafe and unreliable in this case.

In this work, evoked EMG is used as the feedback of actual muscle activation information, which is useful to predict torque and then to achieve torque control rather than position control. This chapter aims at developing an FES control strategy based on FES-evoked EMG feedback from stimulated muscle to induce the desired torque trajectory. A model-based predictive control strategy taking the eEMG signal as feedback is proposed in this work.

4.3 Muscle Excitation and Contraction Model

In FES, external electrical currents are used to excite the peripheral motor nerves via surface or implanted electrodes; action potentials are subsequently generated and propagate toward the muscle. When the action potentials reach the target muscle, the muscle contracts and produces joint torque and then joint movement. Joint torque control is carried out by adjusting stimulation parameters, either stimulation frequency, stimulation amplitude or PW. By introducing an additional EMG sensor to accompany the torque sensor, the muscle excitation and contraction dynamics are respectively modeled. Just as the muscle contraction dynamics are modeled by a PHM model, a PHM is also applied to describe the muscle excitation responding to the stimulation impulses. This model structure is able to represent a time-varying nonlinear process, as described previously.

Although two PHM models are involved to resolve the control problem of both the excitation and contraction processes, a generic PHM structure and its state-space form are introduced here for simplification as they have the same structure. By modeling the linear and nonlinear parts of the Hammerstein cascade with an ARX and a polynomial basis function, respectively, the PHM at a given time k is parameterized as:

$$f(u(k-i), y(k-i), \theta) = \sum_{i=1}^{l} a_i y(k-i) + \sum_{i=1}^{m} \sum_{j=0}^{n} b_i \gamma_j [u(k-i)]^j \tag{4.1}$$

Note that the MAV of the eEMG is the input u of the contraction dynamics, but for simplification, the abbreviation of eEMG is used instead of the MAV of eEMG in the following description. The weights of inputs are separated for linear and nonlinear terms, rather than being coupled as in (3.10).

The delivered stimulus, the collected eEMG, and the torque signals are provided to identify both the muscle excitation and contraction models, as shown in Fig. 4.2. Apparently, the eEMG acts as the output of the excitation model with stimulation as the input, as well as the input of the contraction model with joint torque as the output. To indicate the two distinct statuses of eEMG in these two models, different notations are used for eEMG, with u as input and y as output. Furthermore, the model input u, the unmeasurable internal variable h, and the model output y in the above-mentioned generic formulation are substituted by u_s, h_s, y_m in the excitation model and u_m, h_m, y_t in the contraction model, as shown in Fig. 4.2.

With the same model structure representing the muscle excitation and contraction dynamics, the identifications of both models are processed in the same way. The only difference is

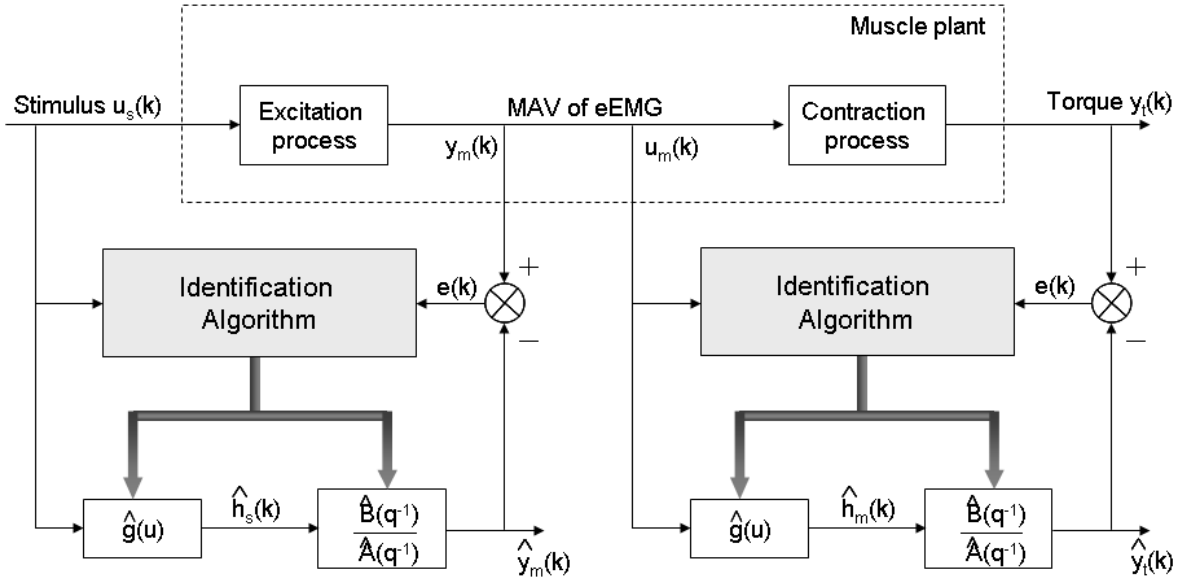

FIGURE 4.2: Model structure of stimulated muscle for model identification. The contraction dynamics model relates eEMG to torque. The excitation dynamics model relates stimulation to eEMG.

that data sets $(u_s(i),\ y_m(i))$ are prepared to identify the stimulation-to-eEMG model, while data sets $(u_m(i),\ y_t(i))$ are prepared to identify the eEMG-to-torque model. When constructing the state-space form of the generic PHM (l,m,n) model, the following process equation is used instead of the equation (3.14):

$$\mathbf{x}(k) = \underbrace{\mathbf{A}\mathbf{x}(k-1) + \mathbf{B}\mathbf{\Psi}\mathbf{u}(k-1) + \mathbf{w}(k)}_{\mathbf{f}(\mathbf{x}(k-1), \mathbf{u}(k-1), \mathbf{w}(k))} \tag{4.2}$$

where $\mathbf{u}(k-1)$ is the previous model input as (3.15) and subscript k denotes the current time step. The current state vector $\mathbf{x}(k) = \begin{bmatrix} x_1(k) & x_2(k) & \cdots & x_q(k) \end{bmatrix}^T$, $q = \max(l, m)$. Matrix $\mathbf{A} \in \mathbb{R}^{q \times q}$ correlates the previous states with the current states. Vector $\mathbf{B}$ and $\mathbf{\Psi}$ contain linear and nonlinear weights of eEMG,

$$\mathbf{B} = \begin{bmatrix} b_1 & b_2 \cdots b_m \end{bmatrix}^T \tag{4.3}$$

$$\mathbf{\Psi} = \begin{bmatrix} \gamma_0 & \gamma_1 \cdots \gamma_n \end{bmatrix} \tag{4.4}$$

Thus, the linear and nonlinear parameter vectors can be written as

$$\theta_l = \begin{bmatrix} a_1\ a_2 \cdots a_l\ b_1\ b_2 \cdots b_m \end{bmatrix}^T \tag{4.5}$$

$$\theta_n = \begin{bmatrix} \gamma_0\ \gamma_1 \cdots \gamma_n \end{bmatrix} \tag{4.6}$$

This improvement is meaningful for the direct application of the predictive control scheme with the linear part of the PHM model. Next, all the time-varying states and parameters involved are identified concurrently by KF with forgetting factor, as proposed in Section 3.6.2.

4.4 Controller Design

This work aims at developing an EMG feedback closed-loop control strategy which can adaptively modulate the stimulation pattern to obtain the desired torque trajectory. This control scheme is developed based on the two internal PHM models described above. Accordingly, the controller consists of two Nonlinear Generalized Predictive Control (NGPC) in series, as shown in Fig. 4.3. The control target is to generate an optimal stimulation signal u_s to produce the desired isometric joint torque y_d. The main idea is to use the eEMG signal for a dual purpose resulting in EMG-Feedback Predictive Control (EFPC), which involves an activation controller and a stimulation controller. The activation controller takes eEMG as the control signal m_d to drive the predicted torque y_p, close to the desired torque trajectory y_d, based on the contraction dynamics model. The stimulation controller takes m_d obtained from the activation controller as the desired eEMG trajectory, so that the control signal, stimulation PW u_s, is computed to drive the predicted eEMG m_p close to m_d, based on the excitation dynamics model. In both the ac-

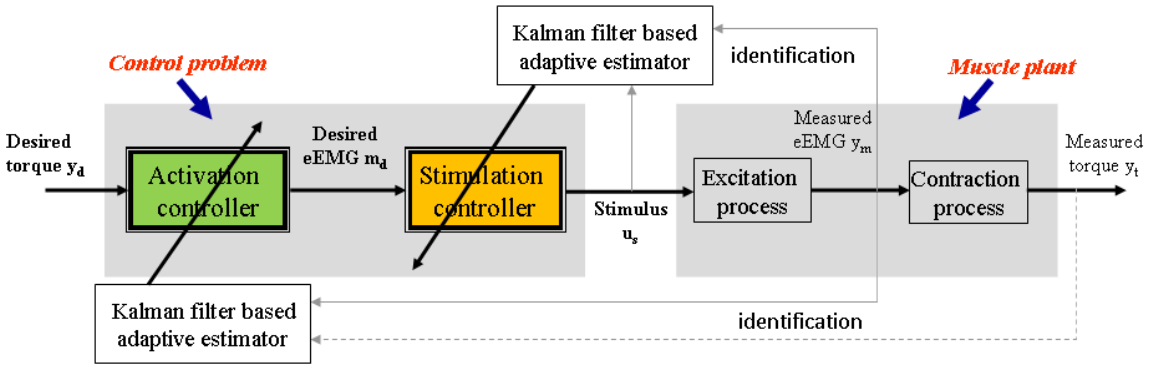

FIGURE 4.3: Diagram illustrating the EMG-feedback predictive control strategy. The control signal obtained from the activation controller is used as the desired reference of the stimulation controller. In each controller, a nonlinear generalized predictive control algorithm is applied based on a PHM model. The torque measurement y_m and eEMG measurement m_m are only used for model identification, as shown by the dashed lines.

tivation controller and the stimulation controller, the same model structure — a generic PHM model — is used for process prediction and optimization. Therefore, the overall control problem can be reduced to resolve two single NGPC problems. The link between these two NGPC controllers lies in that, at each sample time, the output of the activation controller is used as the input of the stimulation controller. Therefore, in the next section, the control solution based on a single generic PHM model is discussed. The notations are kept consistent, as described in section 4.3.

4.4.1 Nonlinear Generalized Predictive Control

As a whole, the solution of a single NGPC consists of two parts: a linear part and a nonlinear part, as shown in Fig. 4.4. The control problem of the linear part is first resolved by the Generalized Predictive Control (GPC) algorithm, which has been described in a number of pu-

blications such as [Camacho and Bordons, 1999] and [Zhu et al., 1991]. Although different methods can be used to obtain the control law of GPC, the general idea is to minimize a multistage cost function given by

$$J = \sum_{j=1}^{N_p} \xi_j [\hat{y}_{k+j|k} - v_{k+j}]^2 + \sum_{j=1}^{N_u} \delta_j [\Delta h_{k+j-1}]^2 \tag{4.7}$$

where $\hat{y}_{k+j|k}$ is an optimum j-step ahead prediction of the controlled variable using data up to time instant k, v_{k+j} is the future reference trajectory, and $\Delta h_{k+j-1} = h_{k+j|k} - h_k$ is the increment of control action. Weighting coefficients ξ_j, δ_j respectively penalize the tracking performance regarding $\hat{y}_{k+j|k}$ and the smoothness of the control signal regarding Δh_{k+j-1}. N_p is known as the prediction horizon and the control horizon is N_u; $1 \leq N_u \leq N_p$ implies that all the increments of the control effort are assumed to be zero for $j > N_u$.

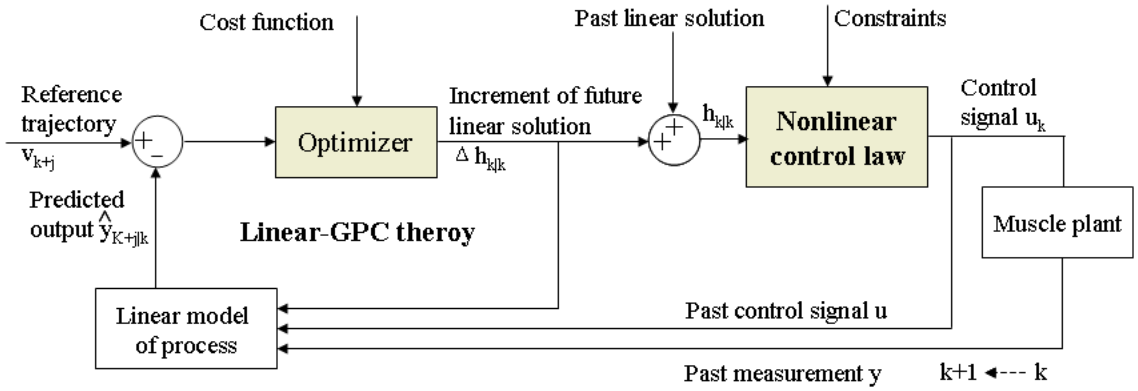

FIGURE 4.4: A single nonlinear generalized predictive controller based on a PHM model. The linear solution is provided by the linear generalized predictive control law. The nonlinear solution is obtained by resolving a polynomial function.

The optimization problem is computed online and in real-time in terms of the control action sequence $[h_{k|k}, h_{k+1|k}, \cdots, h_{k+N_u-1|k}]$, so that the predicted controlled variables $[\hat{y}_{k+1|k}, \hat{y}_{k+2|k}, \cdots, \hat{y}_{k+N_p|k}]$ follow a desired reference trajectory $[v_{k+1}, v_{k+2}, \cdots, v_{k+N_p}]$.

The control signal $h_{i|k},\ i = k \sim k + N_u - 1$ computed by GPC is a solution of the linear predictive control problem at step k, which is required to be applied to the linear part of the system. It is also provided to generate the plant input u_k on the basis of function (3.1). The nonlinear problem can be stated such that, at each time step, the signal $h_{i|k}$ is obtained as described above, the nonlinear model coefficients $\gamma_0, \cdots, \gamma_n$ are known by model identification, and the nonlinear problem is to find the control input signal $u_{i|k},\ i = k \sim k + N_u - 1$. It can be resolved as finding zeros of the following function

$$p(u_{i|k}) = \gamma_0 + \gamma_1 u_{i|k} + \gamma_2 {u_{i|k}}^2 + \cdots + \gamma_n {u_{i|k}}^n - h_{i|k}. \tag{4.8}$$

In this work, $u_{i|k}$ is calculated by finding eigenvalues using the Frobenius companion matrix [Malek and Vaillancourt, 1995]. Until now, the control problem of a nonlinear generalized

predictive controller was solved in two steps, first a linear solution and then a nonlinear solution. Usually, only the first element of the control sequence $u_{k|k}$, $u_{k+1|k}, \cdots, u_{k+N_u-1|k}$ is actually implemented during time interval [k,k+1]; that is, $u_k = u_{k|k}$. The procedure is repeated at the next sampling time.

As described above, the proposed dual predictive controller consists of two NGPC controllers that work successively. In this dual NGPC, the control signal sequence obtained in the activation controller is treated as the reference trajectory for the stimulation controller. In the stimulation controller, only the first control signal is sent to the stimulator at each sample time. The closed-loop implementation of the EFPC consists of the following steps periodically:

Algorithm Closed-Loop Implementation of the Dual Predictive Controller

1. $k \leftarrow 0$
2. Initialize the KF, and the control parameters for the activation and stimulation controllers: prediction horizon N_{p1}, N_{p2}, control horizon N_{u1}, N_{u2}, and weighting factors ξ_1, δ_1, ξ_2, δ_2.
3. **while** system is running ***do***
4. $k \leftarrow k + 1$
5. Collect the eEMG and torque signals (at current instant k)
6. Update the model parameter estimates by KF for both the muscle excitation model and the contraction model. Note that, both the linear parameters in θ_l (4.5) and the nonlinear parameters in θ_n (4.6) are simultaneously identified

   //activation controller
7. Calculate linear solution sequence h_m by GPC (see Fig. 4.4)
8. Calculate control signal sequence m_d using (4.8), and then these are used as the desired reference for the stimulation controller

   //stimulation controller
9. Calculate the intermediate signal h_s by GPC (see Fig. 4.4)
10. The control signal u_s is calculated using (4.8)
11. Apply u_s to the stimulator
12. ***end***

4.5 Evaluation of Predictive Performance

Drop foot is a condition in which an individual is not able to adequately dorsiflex or lift the foot. It is associated with a variety of conditions such as stroke, head injury, spinal cord injury, multiple sclerosis, and cerebral palsy [Lyons et al., 2002]. Regardless of the mechanism of injury, the drop foot condition can be improved by different techniques, which are typically referred to as drop foot correction.

To assess the performance of the proposed EFPC, preliminary experiments for drop foot

correction are conducted on three healthy subjects. Surface stimuli are applied with stimulation PW modulation and constant amplitude and frequency. The common peroneal nerve and the Tibialis Anterior (TA) are both activated as usual to induce dorsiflexion. Isometric ankle torque and eEMG signals are collected for off-line analysis. After signal processing as described in section 3.4.3, the relationship between stimulation, MAV of eEMG, and torque in 45-s recruitment and random stimulation sessions are respectively plotted in Fig. 4.5. In random test sessions, the stimulation PW at a plateau of each train is randomly determined from 20% $\sim$ 100% of maximum PW. This protocol is important to verify more realistic and complex gait events and is rarely investigated.

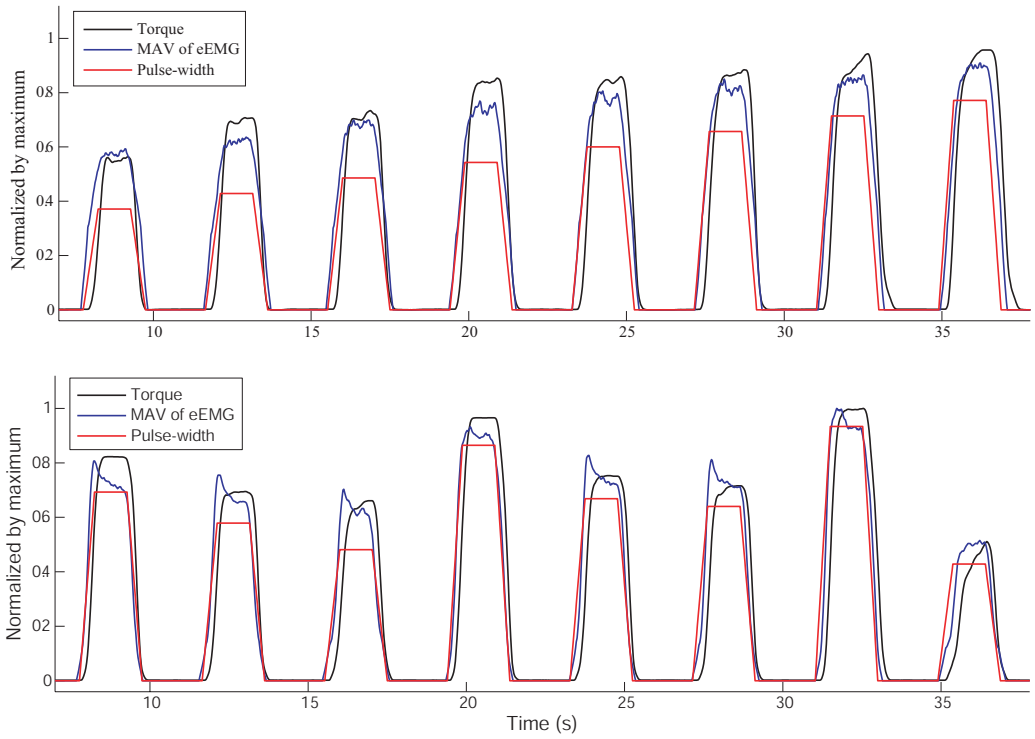

FIGURE 4.5: Relationship among stimulation pulse width, MAV of eEMG, and torque in recruitment (top) and random (bottom) tests. All variables are normalized by their maximum value.

4.5.1 Experimental Validation of Predictive Torque Control

First, the control performance is evaluated by comparing the obtained control signal with the actual experimental stimulation PW. The measured torque is considered as the desired torque reference, where the control signal is computed by the EFPC. As we use experimental data for this study, the actual stimulation input corresponding to the generated torque is known. Here, we try to verify whether the input solution from the EFPC controller is appropriate in comparison with the true stimulation input. If they match well, this implies that the model identification and controller work correctly. The forgetting factor of the Kalman filter is fixed at 0.999 as the muscle fatigue rate is lower in healthy subjects than in patients with SCI. The sampling time is 0.025 s, consistent with a 40-Hz stimulation frequency. The control signal u_s,

the normalized MAV of eEMG, is constrained within [0,1], representing respectively, non-fiber recruitment and maximal fiber recruitment. For convenience, in each NGPC, the weighting coefficient of the controlled variables is set at $\xi = 1$, while the weighting coefficient of the control signal is adjustable. Therefore, the tuning problem is reduced to tuning one weighting parameter δ_1 in the activation controller and one δ_2 in the stimulation controller.

One example result is shown in Fig. 4.6. The reproduced torque through the EFPC shows good fidelity with the desired trajectory. The control signals show acceptable accuracy with an RMS error of 7.2% $\sim$ 9.1% of PW_{max}. Moreover, the muscle fatigue that results from repetitive stimulation and the effect of withdrawal reflex in this stimulation protocol are unavoidable, so the control performance also indicates the ability of this control strategy to compensate muscle fatigue and reflex to some extent.

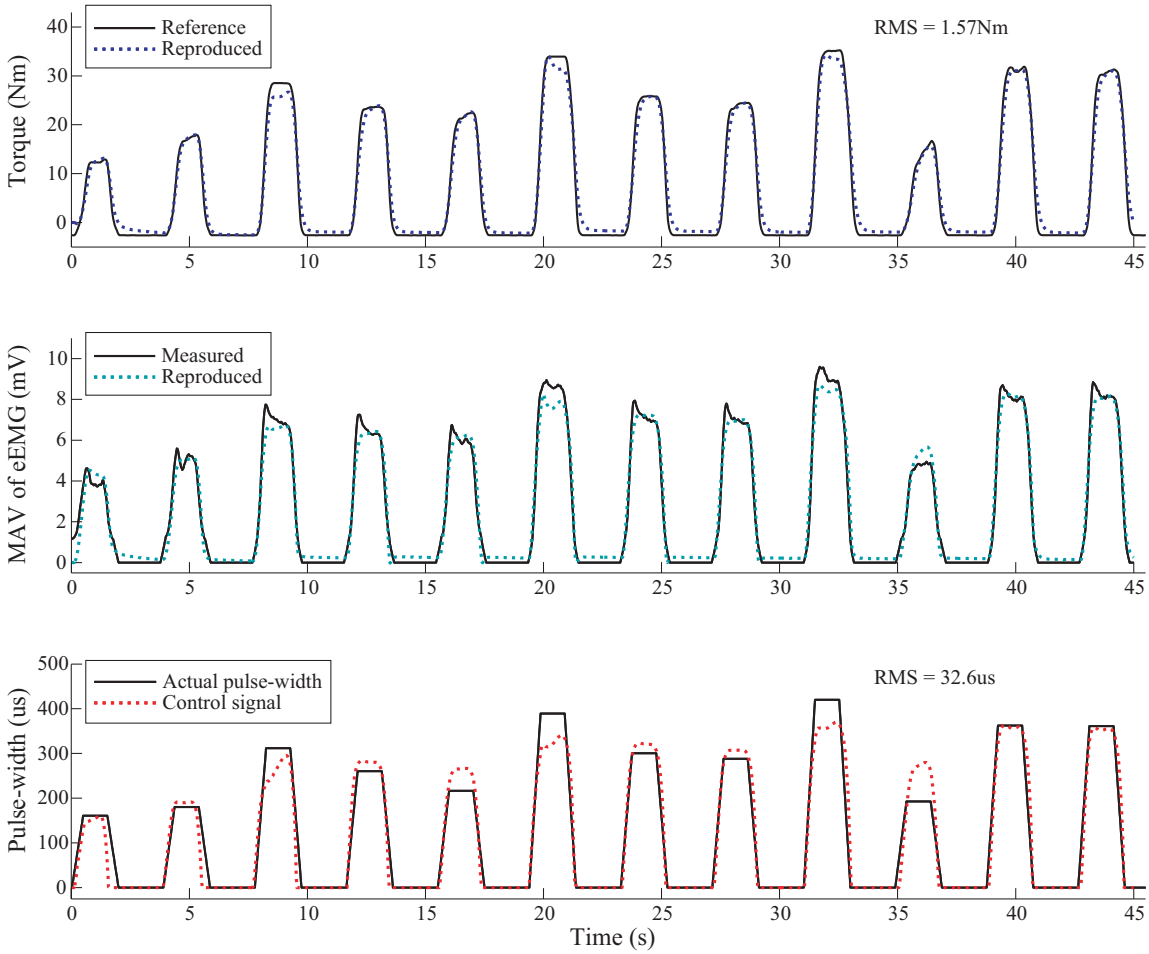

FIGURE 4.6: Evaluation of EFPC to obtain randomly changed torque in subject OR. Upper: Reproduced torque from the muscle model (dashed blue) tracks the desired torque (solid black) well. Middle: The actual eEMG and the reproduced eEMG through the excitation model are shown. Bottom: The control signal matches the actual stimulation input well, indicating the controllability and fatigue compensation ability of the proposed EFPC.

Torque control only based on the eEMG signal

In order to assess the robustness of the proposed controller in the scenario where a torque sensor is not available or controllability is based only on eEMG information, the identification of the muscle contraction model is switched off at an arbitrary time instant t. This scenario is quite useful for FES control in the presence of sensor failure or control based only on eEMG feedback while torque control quality is maintained. The results in two subjects are illustrated in Fig. 4.7 and Fig. 4.8. This indicates that control without a torque update is feasible in the identification process, especially when muscle fatigue develops slowly, which may occur in some subjects. The RMS errors of controlled torque, intermediate state — the MAV of eEMG and the control signal — stimulation PW, are averaged in several tests in each subject and summarized in TABLE 4.1.

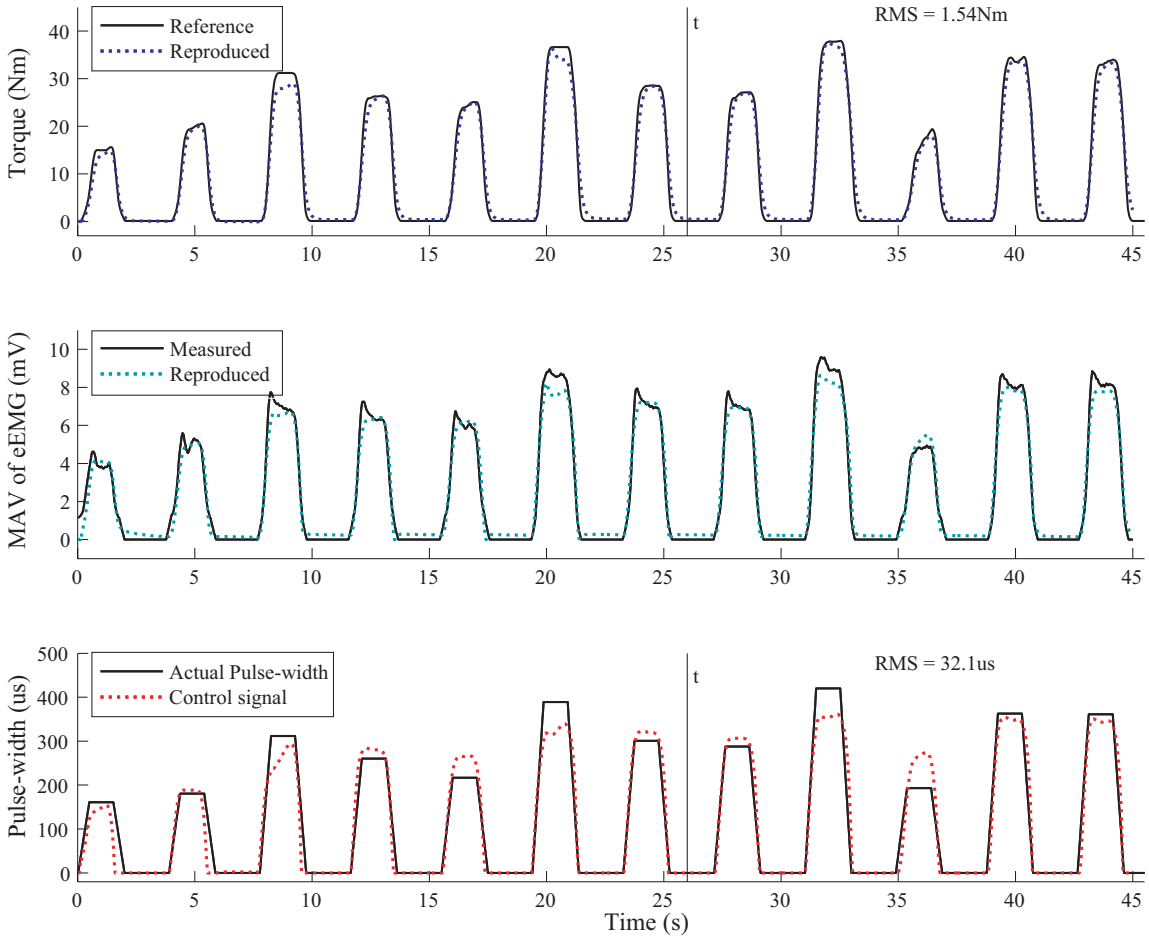

FIGURE 4.7: Evaluation of the robustness of the proposed EFPC to obtain randomly changed torque in subject OR. Top: The reproduced torque tracks the desired torque well. Bottom: The control signal still matches the actual stimulation PW well, even when eEMG-to-torque model identification is switched off from instant t, simulating unreliable torque measurement.

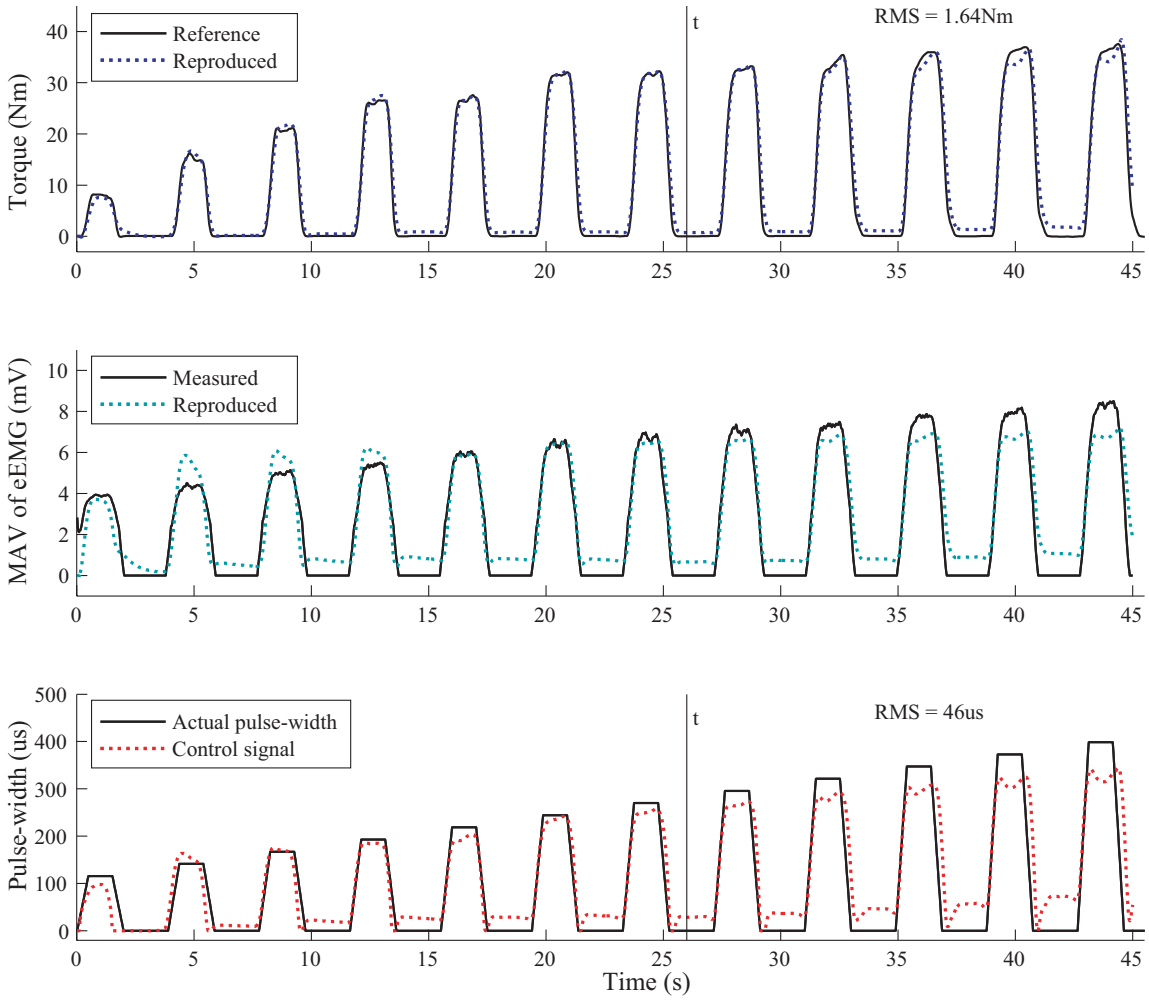

FIGURE 4.8: Evaluation of the robustness of the proposed EFPC to obtain randomly changed torque in subject HG. Top: The reproduced torque tracks the desired torque well. Bottom: The control signal does not deteriorate extremely, even when eEMG-to-torque model identification is switched off from instant t.

TABLE 4.1: Summary of the control errors while eEMG-to-torque model identification is switched on/off

Subject (Number of tests)	Variable	Averaged RMS Error	
		ON	OFF
OR (N=6)	Torque (Nm)	2.28	2.16
	PW (us)	39.8	40.47
HG (N=9)	Torque (Nm)	1.77	1.78
	PW (us)	45.5	46.9
ZQ (N=2)	Torque (Nm)	0.895	0.915
	PW (us)	49	50.4

4.5.2 Featured Predictive Control Performance

In this preliminary work, the fatigue compensation approach is not incorporated into real-time FES control. Therefore, simulation studies are carried out to evaluate the performance of the EFPC in generating an appropriate stimulation pattern for an arbitrary torque envelope and compensating fatigue. Virtual subjects are constructed with the model identified by the experimental data. From the successful experimental results in section 4.5.1, we expect that the identified model reflects the actual muscle properties quite well. The versatility of the proposed EFPC is evaluated in terms of muscle fatigue compensation and the generation of the stimulation pattern.

Effects of weighting factors

The torque reference consists of a sequence with a square train and a trapezoidal train. The tracking performance of the desired torque is shown in the left plot of Fig. 4.9. Three sets of weighting coefficients are tested, respectively referred to as EFPC1 ($\delta_1 = 0.1$, $\delta_2 = 20$), EFPC2 ($\delta_1 = 0.5$, $\delta_2 = 5$) and EFPC3 ($\delta_1 = 20$, $\delta_2 = 2$). It is found that, on the one hand, different weighting coefficients lead to different converging times to the desired torque and, on the other hand, even though different weighting coefficients are selected, the controlled torque is able to track the torque reference in a limited time and the transient processes are smooth in both torque tracking and control input, which is important for muscle to gradually respond to the stimulation. It also matches the intuitive requirements of muscle response during electrical stimulation.

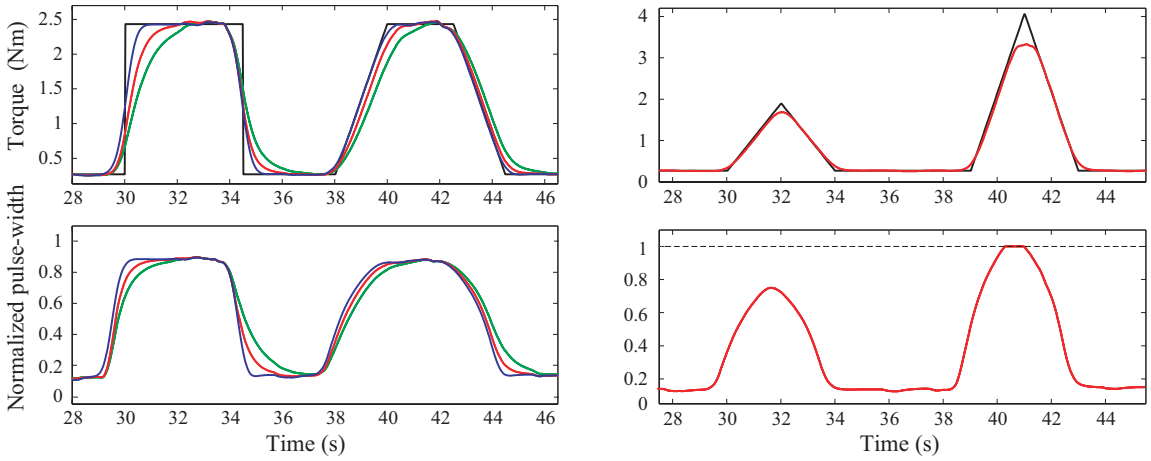

FIGURE 4.9: Left: To track the torque reference (black), three sets of weighting factors are tested, EFPC1 (green), EFPC2 (red), and EFPC3 (blue). Right: Torque reference (black) and reproduced torque (red) are shown in the top plot. The normalized control signal is constrained in [0,1] to guarantee stimulation safety of subjects (bottom).

Moreover, even if an unrealistic torque trajectory is designed by mistake, the controller can generate a more realistic stimulation signal by adjusting the weighting coefficients. This feature is important since the muscle reactive rate is limited, whereas the controller has the ability to ensure practical input transition.

Effects of control constraints

The desired torque reference consists of a sequence of two triangular trains, where different maximum peaks are set. The simulation result is shown in the right plot of Fig. 4.9. The proposed EFPC is used to generate the stimulation PW to drive the predicted torque as close as possible to the desired torque. The stimulation pulse width represents saturation when the stimulation arrives at the maximum value within the predefined stimulation range. This property is important so that the FES controller ensures the safety of patients, rather than damaging them with overstimulation.

Muscle fatigue compensation

The goal of this study is to assess the ability of the EFPC to compensate fatigue effects. A torque trajectory with the same torque level is assumed as the torque reference, and the virtual subject is used as above. The EFPC works to generate suitable stimulation PW in order to maintain the torque level. Fig. 4.10 depicts the result for a desired trapezoidal torque trajectory. The average of the RMS errors is approximately 2.18 Nm. The torque trajectories converge to obtain constant maximum torque, and the stimulation has to be increased gradually. Even though these results were obtained in simulation, the virtual model was identified with experimental data. Thus, this result is significant for advanced FES control that allows torque control with automatic muscle fatigue compensation.

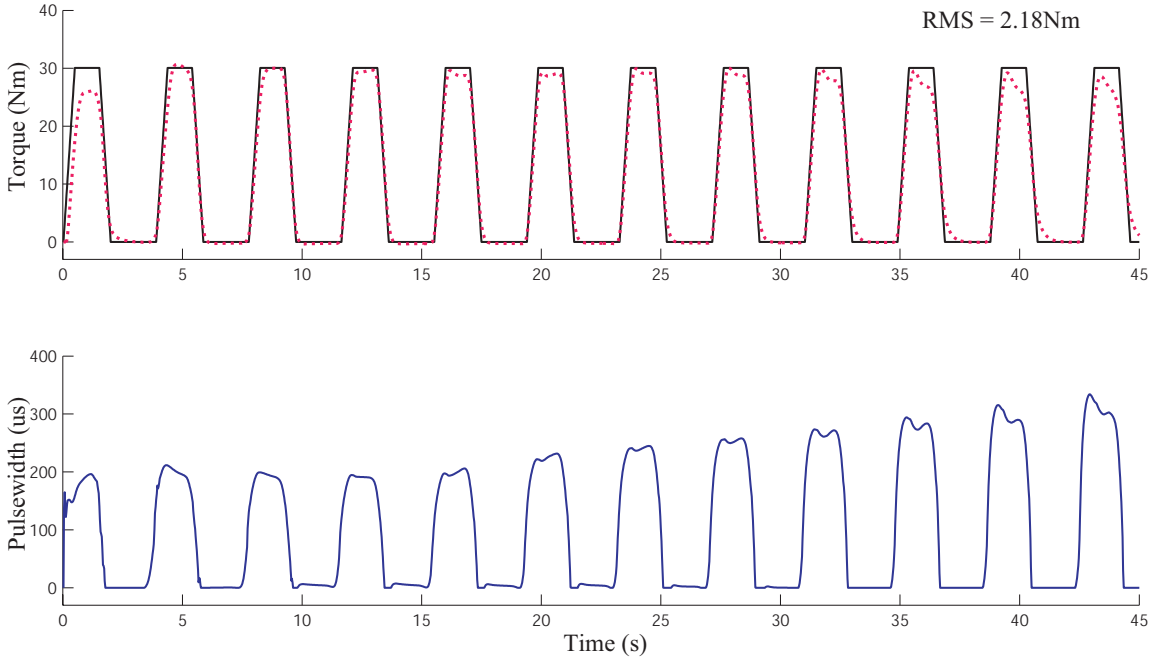

FIGURE 4.10: The torque is desired to be maintained with constant maximum level. The PW required to obtain this torque trajectory is calculated by the proposed EFPC and represents the compensation effect against fatigue.

Complex stimulation pattern generation

The proposed EFPC is also able to track the torque trajectory with any shape in order to perform a complex task. In Fig. 4.11, the envelope of torque reference is simulated according to muscle activity during natural gait [O'Keeffe et al., 2003]. The control framework yields the

stimulation PW that is required to produce the desired trajectory. This is important and convenient to generate the required stimulation pattern for the intended trajectory, which is superior to the empirically defined stimulation pattern.

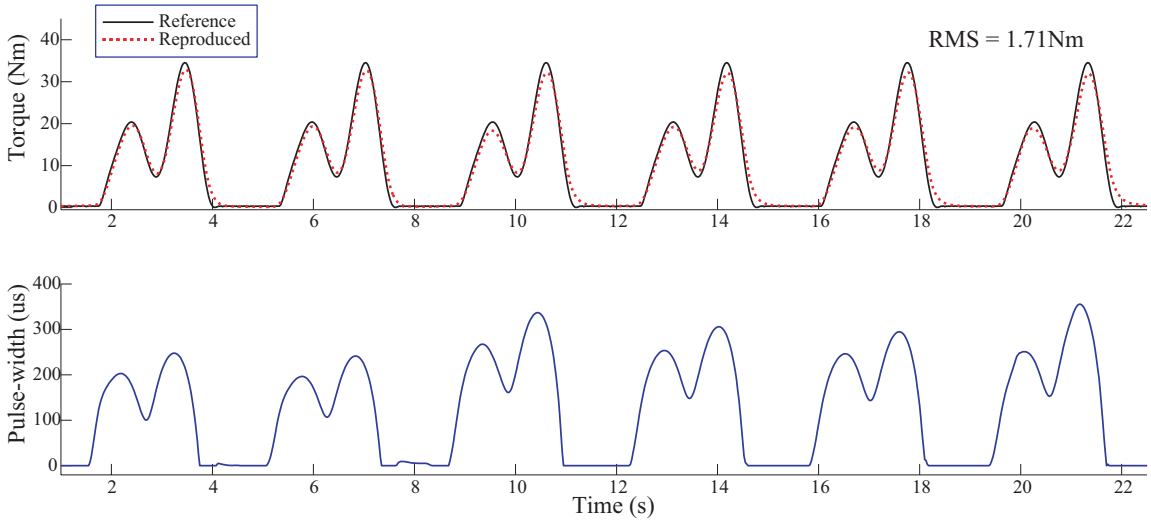

FIGURE 4.11: The top plot traces the torque trajectory (black) and the reproduced torque from the muscle model. The bottom plot traces the stimulation pattern that was created by EFPC for the designed gait torque trajectory.

4.6 Discussion

Open-loop control of FES delivers a predefined stimulation pattern to target muscle. It does not provide feedback on the real muscle response. Closed-loop control is preferred in order to adaptively adjust the stimulation in reaction to unexpected variations in the muscle properties, thereby improving FES performance in terms of robustness. In the context of gait restoration by FES, some research has attempted to develop the optimal stimulation pattern to produce natural gait for open-loop control of FES, which is still useful when the muscle state does not change much, as we see from the performance of existing commercial FES systems. But if we need to specify the exact torque trajectory for a certain desired motion, the appropriate stimulation pattern is still unknown for complex gait events. Thus, it is also important to find a way to generate an optimal stimulation pattern, even for open-loop control, while minimizing muscle fatigue. For this purpose, an optimal stimulation pattern was proposed in [O'Keeffe et al., 2003] by time-consuming optimization. In another work [Johnson and Fuglevand, 2011], a transfer function converting eEMG signals into an appropriate pattern of electrical stimulation was proposed to generate the desired torque trajectory.

In this work, an EFPC framework for FES is developed. This framework provides control adaptability and torque control rather than classical position control. The eEMG signal recorded from stimulated muscle is used to feedback the actual muscle activity to achieve torque control, which has never been tried in the FES context, since an appropriate torque sensor has not been available for human joints, which differ from robotic joints. As muscle mechanical be-

havior always lags after muscle electrical behavior, it is feasible to use eEMG to predict torque generation before delivering a stimulus to the target muscle. In addition, the predictive feed-forward property of the predictive controller contributes smooth input transition, taking into account the physiological muscle activation process in advance. This EFPC contributes to augmenting the FES system in several aspects. First, an appropriate and secure stimulation pattern can easily be generated to produce the desired torque for open-loop use. This is useful when muscle fatigue is not evident or tracking accuracy is not strictly required. Second, in this control strategy, the control signal can be explicitly constrained to guarantee stimulation safety. Last, this control strategy is capable of muscle fatigue or reflex compensation. Moreover, the solution of the EFPC mainly consists of a two-step solution with a simple NGPC structure, where only the linear system is considered in the cost function, while the nonlinear term is excluded. Consequently, the calculation of each control update takes less than 15 ms in the Matlab environment, which is sufficient for real-time implementation of FES with the commonly used stimulation frequency of 20 Hz$\sim$50 Hz. The typical drawback of predictive control is that model inaccuracy may affect control performance. This issue is covered in this work by KF with forgetting factor for time-varying and subject-specific model identification.

4.7 Real-time Evoked EMG-based Closed-loop Control of Muscle Activation

This section presents the muscle activation closed-loop control by FES. Predictive model control is used to control the muscle activation level which is represented by filtered MAV of eEMG, and the wireless stimulator is modulating pulse width to control the muscle activation level with constant stimulation frequency and intensity. The model between stimulation pulse width and MAV is described by the Hammerstain model as well. Since the Kalman filter is adopted as the state observer for the predictive model controller, normalization operations are done for both pulse width and MAV by dividing their maximum values. Since eEMG can be always available through acquisition system, the MAV could be thus always used for updating stimulus-to-eEMG model. This can improve the modeling precision of the plant and guarantee the accuracy of the predictive model controller. The control algorithm for muscle activation control by stimulus is as shown by Algorithm 4.7.

Algorithm 4.7 Closed-Loop Implementation of the Model Predictive Controller for Muscle Activation by FES

† $k \leftarrow 0$

Initialize the Kalman filter, and the control parameters for the controller: prediction horizon N_p, control horizon N_u and weighting factors ϵ_j and δ_j.

† **while** The identification is running with predefined stimulation pattern ***do***

$k \leftarrow k + 1$

† Collect the eEMG and compute its MAV at each stimulation loop k

† Update the PW-MAV model parameters estimated by Kalman filter. Both the linear parameters and the nonlinear parameters are simultaneously estimated and stored

† Calculate the intermediate linear solution $h(i|k)$ as shown in Fig. 4.12

† The control signal $s(i|k)$ is calculated using (4.8)

† Send the control signal $s(i|k)$ to the stimulator

† ***end***

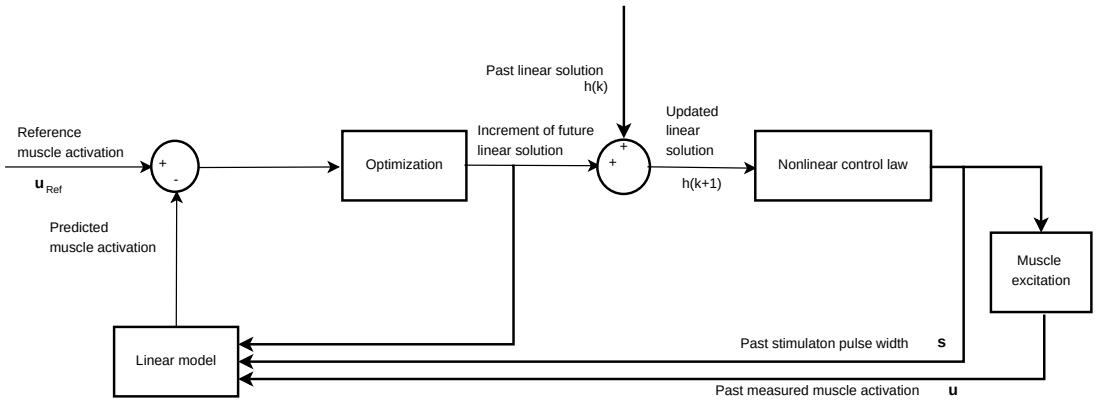

FIGURE 4.12: Updating process of model predictive control of muscle activation by FES.

The following is the real-time implementation of the predictive model controller for online control of muscle activations:

1) The reference muscle activation trajectory is generated before beginning estimation and control;

2) Trapezoidal shape pulse width stimulation in different amplitude levels is predefined with recorded eEMG to identify the relationship between normalized pulse width and normalized MAV of eEMG by Kalman filter;

3) After identification phase ends, the FES system goes into control mode. The stimulator is under computation as a predictive controller to modulate pulse width to track the desired muscle activation trajectory. At the same time, stimulation-to-eEMG model is always updated.

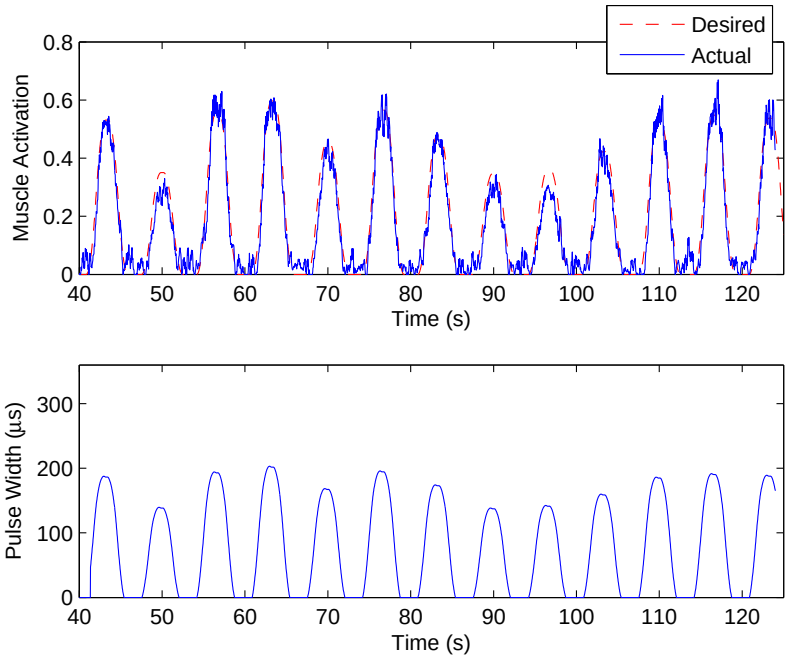

FIGURE 4.13: Upper: real-time control performance of muscle activation with desired random-amplitude muscle activation pattern (red dash line is desired muscle activation trajectory and blue solid line is the measured muscle activation under the muscle activation control by FES). Lower: the corresponding computed stimulation pulse width.

4.7.1 Results and Discusssion

The wireless stimulator (Vivaltis Inc., Montpellier, France) is equipped around TA muscle to evoke its muscle activations, and the eEMG is acquired by the Biopac 100 system (Biopac Inc., Santa Barbara, CA, USA). The TA muscle activation is represented by the normalized MAV of eEMG. Model predictive control is adopted to control the muscle activations by modulating PW of the wireless stimulator, and thus the control input is the stimulation PW and the output is the muscle activation. The model between PW and muscle activation is identified with predefined trapezoidal PW pattern of gradually-increased amplitude plateau and normalized measured MAV of eEMG from time instant 0s to 40s. Afterwards, the predictive model controller is computing the PW level with Stim-eEMG model updated at every stimulation loop and send the PW value to the wireless stimulator to realize the tracking control of the muscle activation under FES. The desired muscle activation for the real-time control by FES is generated artificially following the three patterns:

1) Random amplitude level with constant contraction duration;

2) One kind of natural patterns with two continuous contraction;

3) TA muscle contraction pattern during a whole cycle of actual walking test.

Fig. 4.13 shows the muscle activation control result and the computed PW by the predictive controller with 1) pattern. We observe that the controller possesses good muscle activation control performance to track the desired muscle-activation trajectory. Figs. 4.14 and 4.15 show the

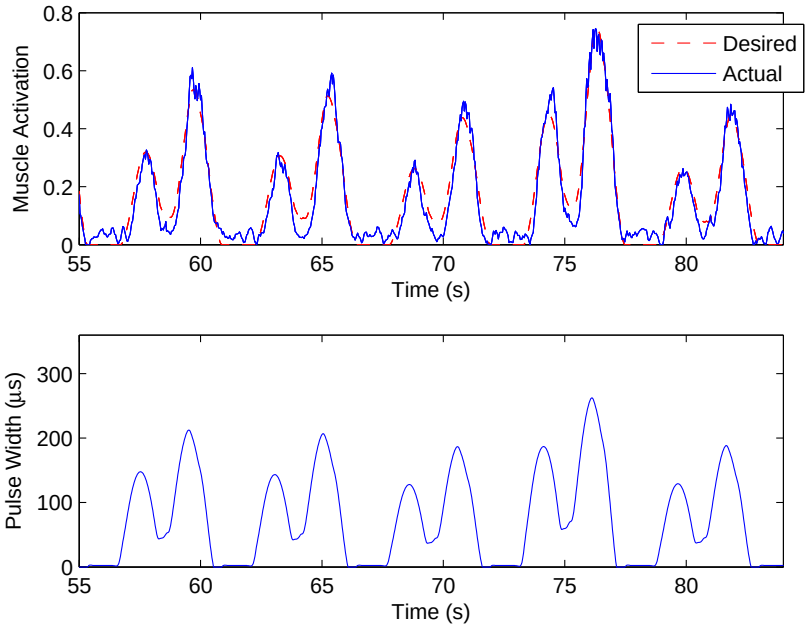

FIGURE 4.14: Upper: real-time control performance of muscle activation with desired natural muscle activation pattern. Lower: the corresponding computed stimulation pulse width. The example shows it succeeds to generate the different levels of muscle activations.

TABLE 4.2: Performance of real-time control of muscle activation for three healthy subjects

Subject #	# of trials	RMSE (%)	VAF (%)
1	15	5.23±1.10	92.7020±2.3329
2	8	6.70±3.77	93.6050± 3.6281
3	13	6.22±2.59	91.3980±4.3074

control performance in 2) and 3) pattern, and we confirm that the developed muscle-activation controller could modulate the PW to let the TA muscle track the desired muscle activation precisely. The control performance indexed by RMSE and VAF of the FES control tests on three able-bodied subjects as indicated in Tab. 4.2. From this table, we could see that, the mean RMSE error is less than 5% and the mean VAF is above 90% and the standard deviations of the RMSE and VAF are less than 5%, indicating the control performance quite promising and stable.

4.8 Conclusions

The purpose of this work is to improve the performance of FES systems in terms of accurate, safe and robust control of stimulation. As eEMG has been validated for torque prediction in the last chapter, an EFPC strategy is newly developed. To obtain the desired joint torque while taking into account the time-varying muscle dynamics, the eEMG signal is used to feedback

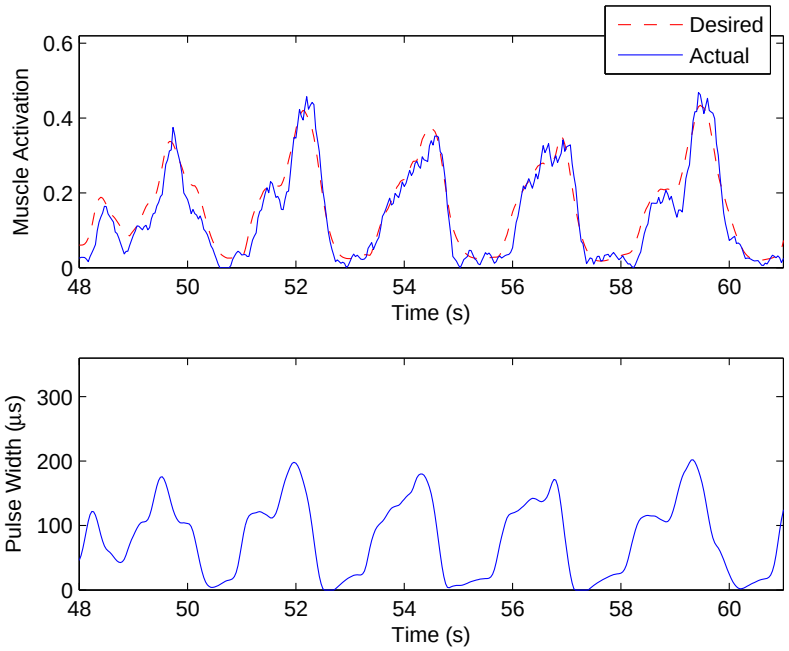

FIGURE 4.15: Upper: real-time control performance of muscle activation with desired walking muscle activation pattern. Lower: the corresponding computed stimulation pulse width. The example shows that this method allows to reproduce other one's muscle activation patterns into the subject.

actual muscle states. The control problem of the EFPC is resolved as a solution of dual NGPC in series. Once the torque deviates from the desired trajectory due to the effects of variations in muscle states like fatigue, the controller will recalculate the appropriate stimulation pattern to achieve the desired torque as long as it does not conflict with stimulation constraints. This control framework provides satisfactory control accuracy and notable robustness for sensing failure, according to the experimental data investigations. In addition, the controller is able to generate a necessary stimulation pattern for a given torque trajectory, which is a new FES control modality enabling joint torque control in FES.

Real-time control ability is demonstrated along with the capability to reproduce someone's muscle activation patterns into the subject muscle. One application is to use averaged muscle combinations as reference to reproduce healthy motor patterns for the motor-disabled patient. Muscle activation control of single muscle could be potentially extended to multiple-muscle case through the artificially reproduced motor synergy patterns by using inversed activation solution as presented in Chapter 5.

CHAPTER 5

Personalized Modeling for Volitional Motor Actions

5.1 Voluntary EMG-to-Force Estimation with Multi-Scale Physiological Muscle Model

Background: EMG-to-force estimation for voluntary muscle contraction has many applications in human motion analysis, sports science and computational rehabilitation. EMG-based model can account for a subject's individual activation patterns to estimate muscle force. So-called Hill-type model has been used in most of the cases. It has already shown its promising performance. However it is known as a phenomenological model considering only macroscopic physiology. In this paper, we discuss EMG-force estimation with a multi-scale physiology based muscle model.

Methods: In addition to Hill macroscopic representation, a microscopic physiology description as stated by Huxley is integrated and applied for EMG-driven muscle model. It has significant meaning to develop EMG-force estimation method with multi-scale physiology dynamics model which is not a phenomenological model. Using EMG signals of isometric muscle contraction in able-bodied subject, the torque estimation results are shown by classical and modified Hill model and proposed physiological based approach.

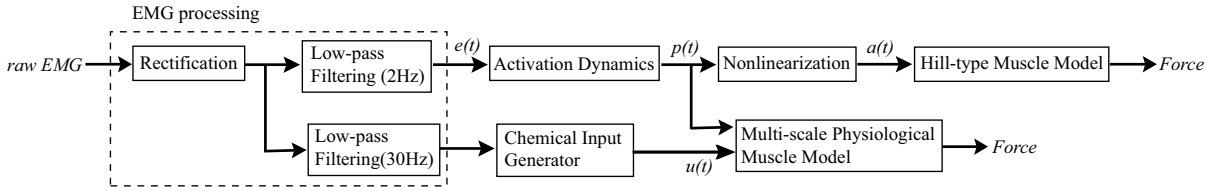

FIGURE 5.1: A flowchart of EMG-force estimation by Hill-type model and multiscale physiological muscle model.

Results: Results estimated by physiology based model show good performance both in short-term and long-term contractions in random tests in two subjects. The smooth transition of torque can be found compared with Hill-type estimation. The acceptable RMS errors can also be found in Hill-type model estimation. However, it is diffcult to obtain small errors in two types of contraction at the same time. This fact corresponds to the recommendation that we should tune appropriate cut-off frequency depending on the task in the case of classical EMG-torque modeling.

Conclusions: We have presented a method that allows to estimate the muscle force from EMG signal with a multi-scale physiology based model with a link to underlying microscopic filament dynamics. Experimental results highlight the feasibility of the torque estimation and its comparison with Hill-type models using same EMG signals. This paper is the first report about EMG-force estimation based on multi-scale physiology model integrating Hill-type and microscopic cross bridge representation. The proposed method features:

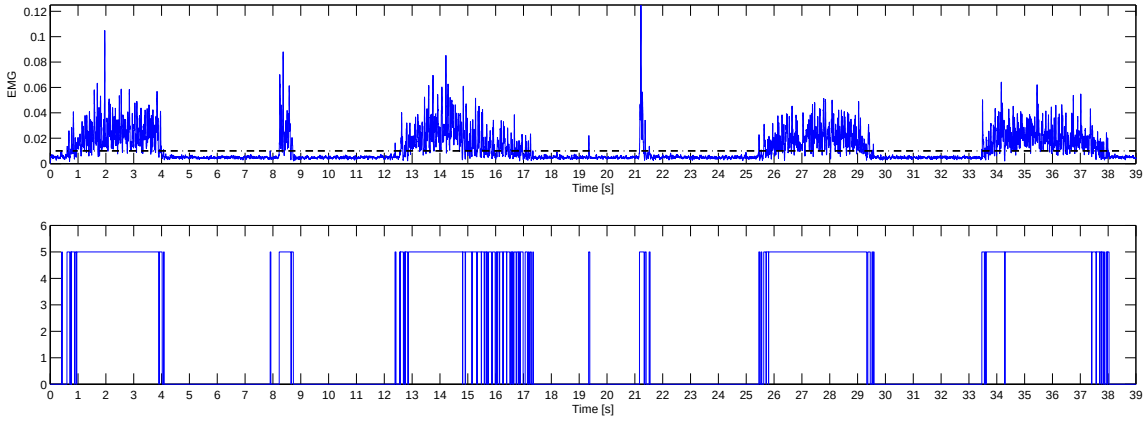

FIGURE 5.2: Generated chemical input (A) filtered rectified EMG signal. (B) chemical input by thresholding for SOL.

- a novel physiologically detailed model for EMG-force estimation instead of a phenomenological Hill-type muscle model,
- the estimation improvement especially for lower activation and short-term contraction with the natural integration of the frequency property of neural activation.
- the consideration of firing rates of motor units in the generation of chemical command input.

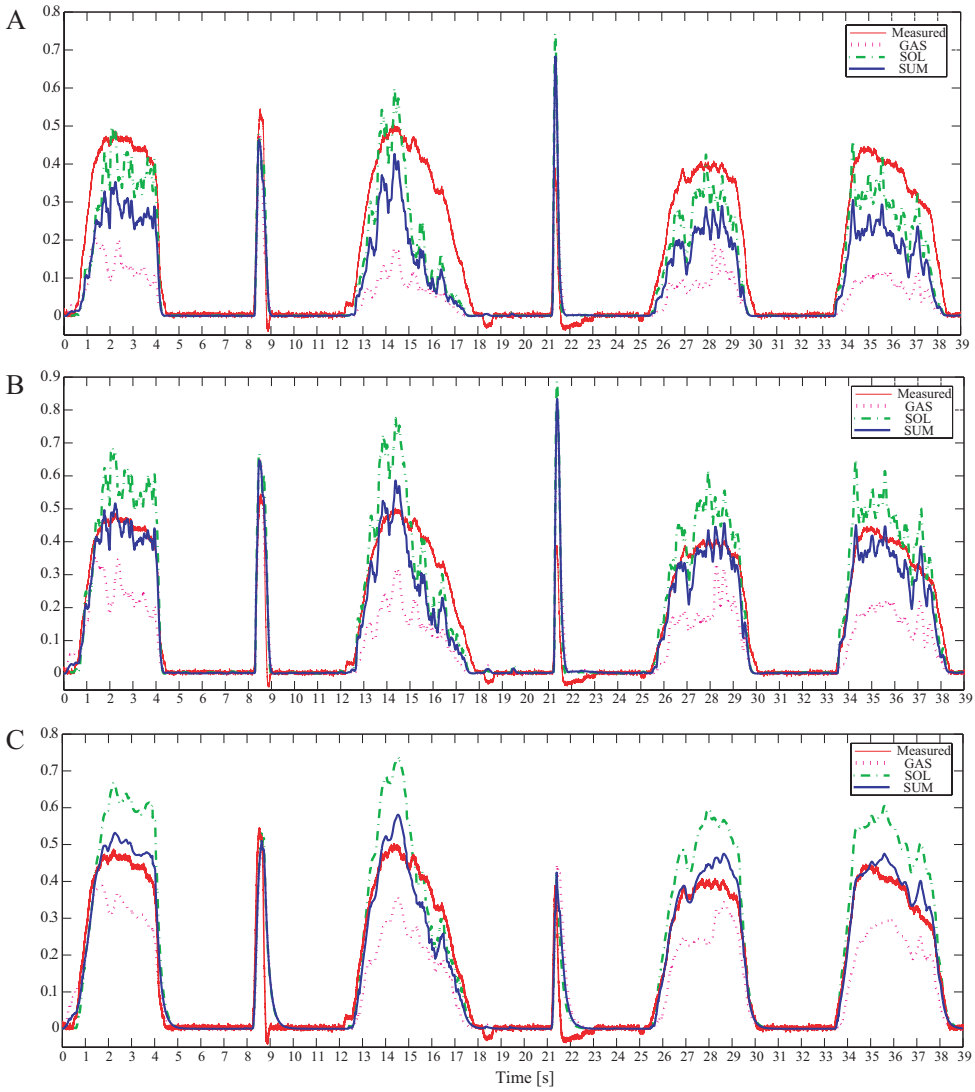

FIGURE 5.3: Normalized estimated torques for random contraction (red: measured, magenta: estimated by model of GAS, green: estimated by model of SOL, blue: sum of both models) (A) result obtained with classical Hill model. (B) result obtained with modified Hill model. (C) result obtained with multi-scale physiology based model.

5.2 Inverse Estimation of Multiple Muscle Activations with Muscle Synergy Extraction

5.2.1 Introduction

In the domain of neuroprosthetics [Borton et al., 2013] based on functional electrical stimulation (FES), conversely, the muscle group activities for the desired movement have to be determined to meet the desired joint torque, which is formulated as the inverse problem. The inverse problem involves indefinite solutions because of the inherent muscle redundancy with respect to the associated joints, and there is no bijection between one degree of freedom and the co-contracted muscles spanning around the joint. In this case, muscle synergy is a useful and insightful concept to investigate co-contractions and the coordination among them [D'Avella et al., 2003]. In a physiological sense, muscle synergy reveals how the central nervous system (CNS) elicits redundant muscle groups in a coordinated manner. It can be obtained from multiple-muscle activations via dimension reduction techniques, aiming at diminishing a higher-dimensioned signal space to a lower-dimensioned feature space.

In general, most current FES systems activate one agonist muscle group for each degree of freedom (DOF). However, instead of stimulating only one muscle, it would help to minimize the rapid fatigue that is a common clinical problem in FES systems if the necessary force could be distributed by activating multiple muscles. To assist the future design of FES systems with distributed control over multiple muscles, information on muscle synergy could be exploited to naturally follow the way CNS regulates and optimally take advantage of muscle redundancy [Wu et al., 2002, Giuffrida and Crago, 2005]. By extracting muscle synergy information from healthy subjects and simultaneously measuring the corresponding kinetics/kinematics, insight into each individual muscle's contribution to the joint flexors/extensors would be obtained. The synergies extracted from healthy subjects, together with their joint moment data, could then be used to design stimulation patterns for multiple muscles of spinal cord injured subjects both in complete and incomplete situations where one still has remaining volitional contraction of their partially deficient muscles [Giuffrida and Crago, 2005]. The recruitment order in percutaneous FES is often in a non-physiological manner, which induces muscle fatigue faster than natural voluntary contraction. Employing multiple redundant muscle activations in FES can promote reducing fatigue of the stimulated muscles and increasing joint articulation stability by using the co-contraction of antagonist muscles [Nielsen et al., 1994]. An insightful view of how multiple muscle activations are coordinated and combined toward the desired joint torque sequence in able-bodied subjects [Kobetic et al., 1997] is needed as an alternative to reduce the time-consuming empirical FES tuning on paralyzed patients. Thus, the computational inverse estimation of multiple muscle activations is of broad interest for FES applications and should moreover help to further elucidate the underlying physiological processes, which is the primary motivation for this chapter.

5.2.2 Muscle Synergy Extraction

Consider the multiple muscle activations u_{SOL}, u_{MG}, and u_{TA} of the SOL, MG and TA muscles during the identification time period $[0, t_{id}]$ (Here, notations with these muscles are used

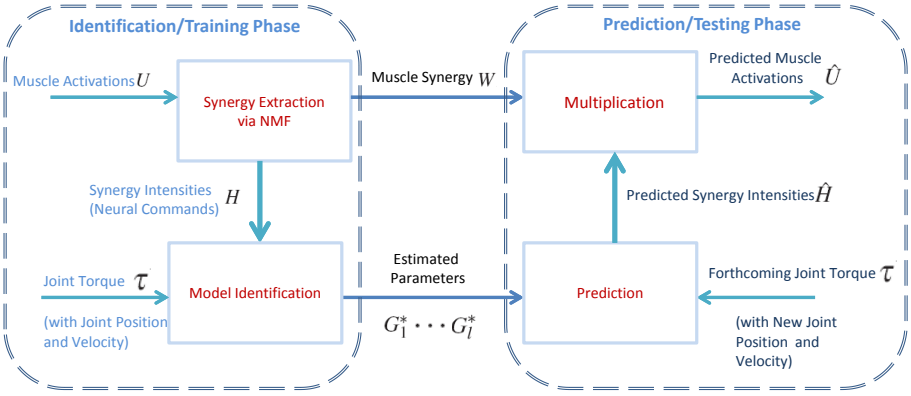

FIGURE 5.4: Block schematic of the process for inverse estimation of multiple muscle activations from the joint movement.

for demonstration, but they can be any other muscle group combination involved in a joint.)

$$U = \begin{bmatrix} u_{\text{SOL}} \\ u_{\text{MG}} \\ u_{\text{TA}} \end{bmatrix} = \begin{bmatrix} u_{\text{SOL}}(0) & u_{\text{SOL}}(1) & \cdots & u_{\text{SOL}}(t_{id}) \\ u_{\text{MG}}(0) & u_{\text{MG}}(1) & \cdots & u_{\text{MG}}(t_{id}) \\ u_{\text{TA}}(0) & u_{\text{TA}}(1) & \cdots & u_{\text{TA}}(t_{id}) \end{bmatrix} \tag{5.1}$$

One can use NMF to decompose U as [D'Avella et al., 2003]

$$U = WH + E \approx WH \tag{5.2}$$

where W denotes the muscle synergy ratio matrix, H denotes the extracted synergy intensity vector (neural command), and E is the decomposition residual error term. The decomposition for updating entries h_{lm} and w_{nl} of H and W is conducted with the following iterative algorithm [D'Avella et al., 2003]:

$$h_{lm} \leftarrow h_{lm} \frac{[W^T U]_{lm}}{[W^T W H]_{lm}} \tag{5.3}$$

$$w_{nl} \leftarrow w_{nl} \frac{[U H^T]_{nl}}{[W H H^T]_{nl}} \tag{5.4}$$

It should be noted here that, there are two types of articulation for ankle joint sagittal movement for one DOF: plantar flexion and dorsi flexion [Sinkjæ r et al., 1993][Nielsen et al., 1994]. Therefore, the number of muscle synergies can be finalized as two for one-DOF corresponding to the flexion and extension of the joint, that is, the dimension of the reduced resultant subspace is chosen as $l = 2$ in this study.

5.2.3 Identification

Different joint torque levels can be achieved by actuating different levels of muscle synergy intensities. To do so, identification is first established between the joint torque and the synergy intensities. In the literature [Clancy et al., 2012], activation-to-torque (u_i to τ) forward mapping is described in a general nonlinear form $f_i(\cdot), i \in \{\text{SOL}, \text{MG}, \text{TA}\}$ as

$$\tau = \sum_i f_i(u_i)$$

This implies that a nonlinear relationship from torque to activations exists. Throughout this paper, we assume that this inverse relationship can be expressed as the following general nonlinear form $g_i(\cdot)$

$$u_i = g_i(\tau)$$

According to (5.2) and the nonlinear relationship above, the activations of the three muscles can be rewritten as

$$\begin{bmatrix} u_{\text{SOL}} \\ u_{\text{MG}} \\ u_{\text{TA}} \end{bmatrix} = \begin{bmatrix} g_{\text{SOL}}(\tau) \\ g_{\text{MG}}(\tau) \\ g_{\text{TA}}(\tau) \end{bmatrix} \approx W \begin{bmatrix} H_1 \\ \vdots \\ H_l \end{bmatrix} \tag{5.5}$$

Analytically, the extracted synergy intensity vector is

$$\begin{bmatrix} H_1 \\ \vdots \\ H_l \end{bmatrix} \approx W^{\dagger} \begin{bmatrix} g_{\text{SOL}}(\tau) \\ g_{\text{MG}}(\tau) \\ g_{\text{TA}}(\tau) \end{bmatrix} \tag{5.6}$$

where $W^{\dagger}$ is the Moore-Penrose pseudoinverse of muscle synergy matrix W. Consequently, each individual synergy intensity vector can be estimated generally as follows

$$\begin{aligned} \tilde{H}_1 =& G_1^* \Phi_{id} \\ & \vdots \\ \tilde{H}_l =& G_l^* \Phi_{id} \end{aligned} \tag{5.7}$$

where

$$\Phi_{id} = \begin{bmatrix} \tau_0 & \tau_0 & \tau_0 & \cdots & \tau_0 \\ \tau(0) & \tau(1) & \tau(2) & \cdots & \tau(t_{id}) \\ \tau^2(0) & \tau^2(1) & \tau^2(2) & \cdots & \tau^2(t_{id}) \\ \vdots & \vdots & \vdots & \ddots & \vdots \\ \tau^q(0) & \tau^q(1) & \tau^q(2) & \cdots & \tau^q(t_{id}) \\ p(0) & p(1) & p(2) & \cdots & p(t_{id}) \\ v(0) & v(1) & v(2) & \cdots & v(t_{id}) \end{bmatrix}$$

in isotonic case

and the estimated parameters are

$$\begin{aligned} G_1^* =& H_1 \Phi_{id}^{\dagger} \\ & \vdots \\ G_l^* =& H_l \Phi_{id}^{\dagger} \end{aligned} \tag{5.8}$$

where $\Phi_{id}^{\dagger}$ is the Moore-Penrose pseudoinverse of Φ_{id}, τ_0 denotes the baseline joint torque value, and $p(\cdot)$ and $v(\cdot)$ denote the joint position and velocity information respectively.

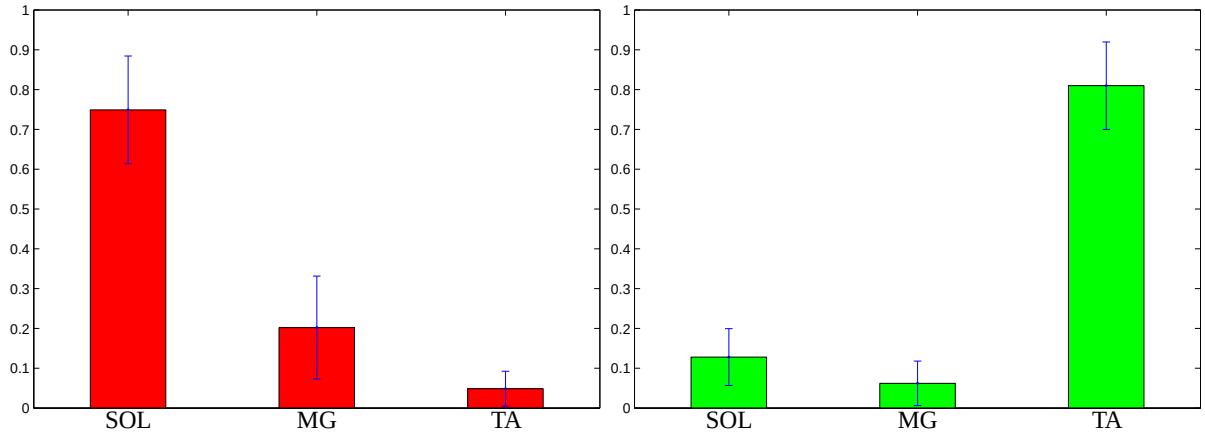

(a) Synergy ratio pattern at plantar flexion (b) Synergy ratio pattern at dorsi flexion

FIGURE 5.5: The obtained muscle synergies for the ten able-bodied subjects. It represents the means of normalized muscle synergy ratios. Error bar indicates standard deviation. We can observe both subject-specificity and common characteristics among subjects.

5.2.4 Results

In this section, we present the inverse estimation/prediction results obtained with the aforementioned approach, based on the experimental data collected from the ten able-bodied subjects. In the identification/training phase, the muscle synergies and intensities are extracted during the identification time period $[0, t_{id}]$ through the NMF algorithm. The parameters G_1^*, G_2^*, which map ankle joint torque and the synergy intensities, are then estimated by equation (5.8). In the prediction/testing phase, the muscle activations are further predicted with the forthcoming ankle joint torque information as the sole input. The evaluation is made under both isometric and isotonic conditions, in order to present the prediction performances in both static and dynamic situations.

The muscle synergies for all ten subjects are extracted from the muscle activation recordings in the corresponding pair of plantar- and dorsi-flexions. To quantitatively evaluate each muscle's contribution to the resultant torque of these plantar- and dorsi-flexions, the normalized synergy ratio for each synergy pair l is defined as follows.

$$\text{Ratio}_{\text{SOL}} = \frac{w_{1l}}{w_{1l} + w_{2l} + w_{3l}}$$
$$\text{Ratio}_{\text{MG}} = \frac{w_{2l}}{w_{1l} + w_{2l} + w_{3l}}$$
$$\text{Ratio}_{\text{TA}} = \frac{w_{3l}}{w_{1l} + w_{2l} + w_{3l}}$$

Fig. 5.5 shows the mean values with standard deviations of the normalized synergy ratios of the ten subjects, with two distinct types of muscle synergy of the three muscles for the subjects.

The first synergy pattern [Fig. 5.5(a)] shows that SOL is the main agonist muscle conducting plantar-flexion of the ankle joint, whereas the second pattern [Fig. 5.5(b)] shows that TA is

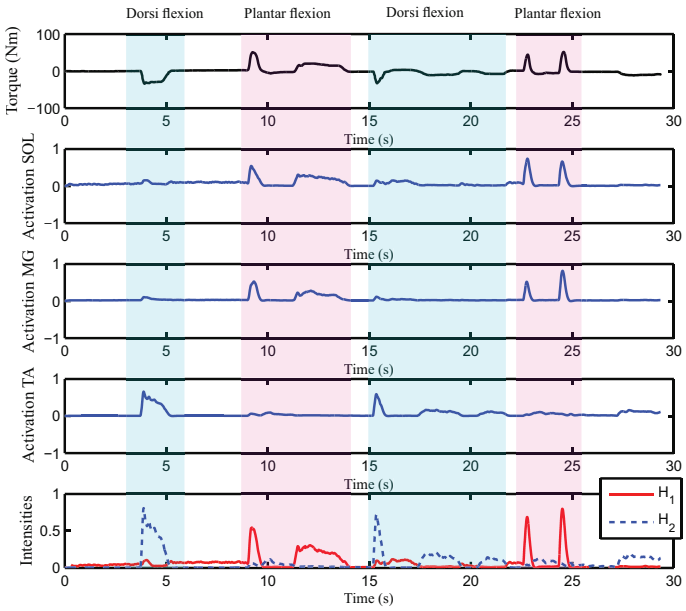

FIGURE 5.6: From upper to lower: 1) ankle joint torque, 2) SOL activation, 3) MG activation, 4) TA activation, and 5) extracted synergy intensity components H_1 and H_2 from muscle activations U by NMF. Note the random pattern of muscle activations between the positive torque period and the negative period, which correspond, respectively, to plantar-flexion and dorsiflexion.

the main agonist muscle for dorsi flexion of the ankle joint. The co-contractions of agonist and antagonist muscles can be observed for both directions of flexion. For more detailed observation, we take Subject V1 as an illustrative example as shown in Fig. 5.6. The two synergy intensity (neural command) vectors H_1 and H_2 extracted from the muscle activations of the three muscles correspond to Synergy 1 and 2 respectively. In Fig. 5.6, one can intuitively observe that, positive ankle joint torque (i.e., plantar-flexion torque) highly correlates with synergy intensity H_1, and negative ankle joint torque (i.e., dorsi-flexion torque) highly correlates with synergy intensity H_2. Since the extracted synergy intensity is the direct reflection of neural command, this may indicate that the CNS may dispatch two different neural commands to control the joint extension and flexion by respectively activating two different pairs of muscle combinations.

To assess the prediction/testing performance of this synergy-based approach, the inverse estimation for multiple muscle activation is demonstrated by cross validation in the ten subjects. In our previous works [Li et al., 2013b][Li et al., 2013a], the multiple regression method was efficient for the inverse estimation of multiple muscle activations. Multiple-regression analysis is without dimension reduction. To compare evaluation between the synergy-based method and the aforementioned multiple regression method, the prediction results using the multiple regression method [Li et al., 2013b][Li et al., 2013a] are presented here as well.

Fig. 5.7 illustrates the isometric case for Subject V1. The identification is finished in a time period ranging 0s to around 47s, and from 47s onward only the identified model and the forthcoming ankle joint torque information are provided for muscle activation prediction. In Fig. 5.7, we see that the predicted muscle activations of the three muscles fit well with the mea-

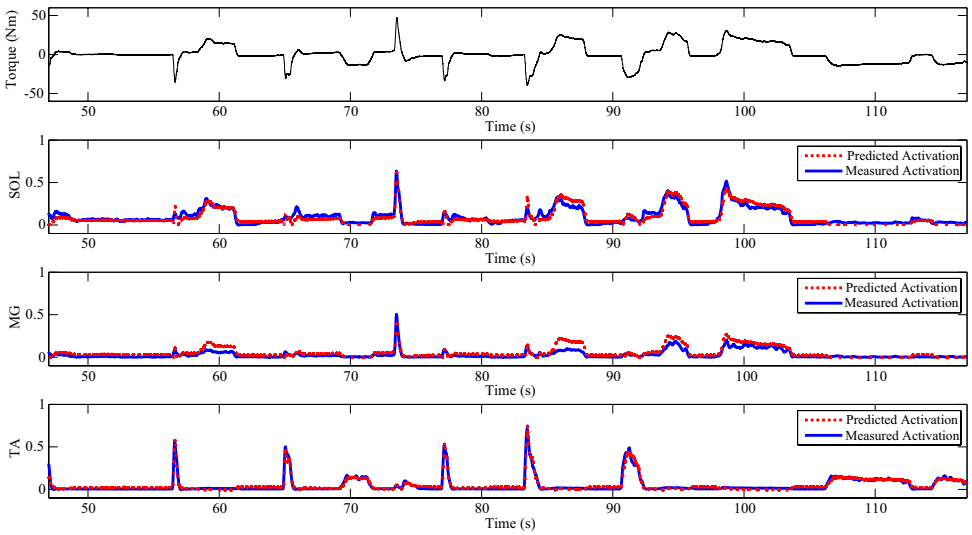

FIGURE 5.7: Cross Validation for Subject V1: From around $t = 47$s the prediction is conducted with the identified model and the incoming joint torque. Red dotted curves represent the predicted activations and blue solid curves represent the measured activations. Torque below and above the baseline represents the dorsi- and plantar-flexion respectively.

sured ones from time instant 47s to the end. Even when dorsi-flexion and plantar-flexion are contained randomly with short (1-2s) and long (>2s) term contractions, the proposed method is able to produce the resultant multiple muscle activations from the ankle joint movement with good accuracy. We observe that the synergy-based method inversely estimates the multiple muscle activations successfully as the multiple regression method.

The p-value obtained by similarity analysis through cross-correlation measure for the errors of the two approaches is less than 0.05, indicating that they are with high similarity. This indicates that the synergy-based method possesses the same estimation quality as the multiple regression method regardless of dimension reduction after muscle synergy extraction. We also use these two methods to estimate the three muscle activations under the isotonic condition. In this situation, the joint position and velocity are also involved for inverse estimation to take into account the muscle response changes due to the force-length-velocity relationship. Tab. 5.1 shows that the performances of two methods via the synergy-based method and the multiple regression method [Li et al., 2013a][Li et al., 2013b] in the isotonic case are similar, indicating that the synergy-based method is similar in estimation quality to the multiple regression method under the isotonic condition (p-value<0.05 by similarity analysis). In Tab. 5.1, the values within parentheses indicate the inverse estimation performance results without joint position and velocity information, whereas the values outside the parentheses are with the joint position and velocity information taken into account. We see that, inverse estimation is improved for both methods by including ankle joint position and velocity information in the isotonic situation (i.e., smaller RMSEs and larger VAFs). Although additional joint position and velocity information could improve the inverse estimation, no significant statistic difference between means is observed [p-value>0.05 by one-way analysis of variance (ANOVA)].

TABLE 5.1: RMSE (%) and VAF (%) of estimated muscle activations of the ten subjects in isotonic condition with constant plantar load 10Nm and dorsi load 5Nm*

Method		Synergy-based method			Multiple regression method		
Profile		$RMSE_{id}$	$RMSE_{pr}$	VAF	$RMSE_{id}$	$RMSE_{pr}$	VAF
V1	SOL	1.44 (1.53)	4.90 (5.12)	79.44 (77.75)	1.43 (1.53)	4.93 (5.12)	79.15 (77.77)
	MG	0.98 (1.15)	4.59 (4.83)	44.14 (37.99)	0.95 (1.15)	4.52 (4.84)	45.74 (37.72)
	TA	2.28 (2.96)	5.66 (6.90)	92.66 (89.13)	2.47 (3.21)	6.14 (7.48)	92.66 (89.14)
V2	SOL	7.86 (7.90)	16.69 (16.69)	61.69 (61.96)	7.83 (7.89)	16.66 (16.65)	61.66 (62.06)
	MG	5.64 (5.72)	11.83 (11.91)	56.07 (55.53)	5.52 (5.70)	11.61 (11.91)	57.68 (55.48)
	TA	7.86 (10.84)	12.28 (14.97)	78.03 (68.24)	7.80 (10.83)	12.29 (14.98)	77.99 (68.19)
V3	SOL	3.17 (3.67)	4.22 (3.66)	59.65 (71.97)	2.99 (3.52)	3.78 (3.17)	65.58 (76.65)
	MG	4.77 (5.54)	6.55 (6.74)	75.14 (74.34)	4.65 (5.44)	6.58 (6.74)	77.62 (77.21)
	TA	8.72 (10.73)	11.63 (12.71)	81.86 (78.45)	8.72 (10.73)	11.53 (12.28)	82.00 (78.59)
V4	SOL	5.18 (5.29)	7.33 (7.57)	70.54 (69.14)	5.14 (5.29)	7.42 (7.50)	69.66 (69.50)
	MG	4.01 (3.97)	5.97 (5.91)	69.09 (69.82)	3.93 (3.96)	5.74 (5.98)	71.57 (69.27)
	TA	4.40 (5.49)	5.79 (5.04)	87.35 (90.05)	4.40 (5.49)	5.79 (5.03)	87.31 (90.06)
V5	SOL	14.03 (14.19)	12.95 (13.12)	87.33 (86.88)	14.76 (14.96)	13.17 (13.44)	85.37 (84.84)
	MG	3.25 (3.10)	3.59 (3.47)	84.45 (85.43)	2.56 (2.71)	3.46 (3.57)	85.19 (83.83)
	TA	9.57 (11.12)	12.17 (12.50)	92.68 (91.77)	12.26 (13.44)	20.10 (21.85)	92.57 (91.50)
V6	SOL	9.39 (11.27)	10.34 (10.63)	64.30 (63.97)	9.36 (11.83)	10.71 (10.94)	56.07 (55.11)
	MG	9.01 (9.63)	7.14 (7.58)	81.77 (79.18)	9.28 (10.21)	7.52 (7.61)	81.02 (80.98)
	TA	6.52 (16.66)	6.35 (11.67)	80.68 (35.39)	6.68 (17.10)	6.23 (12.40)	82.72 (27.91)
V7	SOL	2.94 (3.03)	4.63 (4.77)	52.64 (51.92)	2.94 (3.03)	4.65 (4.80)	53.51 (52.16)
	MG	3.09 (3.13)	4.31 (4.36)	43.43 (43.09)	3.10 (3.13)	4.27 (4.31)	42.90 (42.83)
	TA	3.00 (3.65)	3.16 (3.88)	78.49 (63.50)	3.02 (3.67)	3.29 (4.00)	76.47 (61.12)
V8	SOL	0.55 (0.62)	0.86 (0.92)	80.69 (78.62)	0.56 (0.63)	0.89 (0.93)	79.53 (77.90)
	MG	0.34 (0.35)	0.20 (0.21)	79.87 (77.78)	0.33 (0.35)	0.20 (0.21)	81.06 (77.56)
	TA	1.77 (1.86)	2.22 (2.25)	96.11 (95.80)	1.79 (1.87)	2.18 (2.23)	96.21 (95.87)
V9	SOL	8.27 (9.81)	16.07 (17.65)	49.43 (36.79)	8.15 (9.78)	16.43 (18.06)	47.27 (34.16)
	MG	10.04 (12.48)	14.28 (16.39)	68.02 (55.25)	9.94 (12.46)	13.87 (15.98)	69.73 (57.21)
	TA	2.49 (2.57)	3.61 (3.61)	90.92 (90.92)	2.18 (2.57)	3.55 (3.56)	91.19 (91.17)
V10	SOL	4.54 (4.55)	5.45 (4.86)	74.82 (79.66)	5.47 (5.48)	5.50 (5.46)	73.87 (74.25)
	MG	6.14 (7.28)	8.00 (8.46)	89.88 (88.34)	6.75 (7.56)	8.17 (9.12)	89.43 (86.63)
	TA	3.26 (3.46)	3.85 (4.13)	93.49 (92.53)	3.46 (3.72)	4.22 (4.45)	92.35 (91.46)
Overall Average		5.15±3.34 (6.11±4.34)	7.23±4.42 (7.73±4.88)	74.82±15.07 (71.37±17.68)	5.28±3.59 (6.30±4.57)	7.51±4.94 (8.15±5.48)	74.83±15.03 (70.60±18.44)

* Figures inside parentheses are without joint position and velocity information and ones outside parentheses are with joint position and velocity information.

Tab. 5.2 shows the leave-one-out cross validation, by which the average synergy of the other nine subjects is used for cross validation in the isotonic case to evaluate the inter-subject differences on synergy pattern. Each of the subjects adopted the other subjects' normalized average synergy ratios in their own cross validation respectively, and from Tab. 5.2 we observe that, although the performance tends to be degraded in this leave-one-out cross validation, the difference in accuracy is not so large when it is compared to Tab. 5.1.

5.2.5 Discussion

The proposed framework involves the muscle synergy extraction of multiple muscle activations for inverse estimation from joint torque. Within this framework, NMF is applied to extract muscle synergies from multiple muscle activations to obtain the muscle co-contraction patterns corresponding to different levels and directions of joint flexion/extension. In this study, two synergy patterns are selected to account for the two types of articulation (plantar- and dorsi-flexion) for one-DOF sagittal movement. Similarly, for the flexion and extension of other joints that mainly focus on one-DOF tasks like the knee or elbow, two synergy patterns can be used to divide the muscle groups into flexor and extensor muscles in a systematic manner. The extracted synergy intensity vectors may help to analyze the individual correlations and the driving impact to the joint space. Fig. 5.6 shows that, each component of synergy intensity matrix

H can have different levels of correlations with the joint torque; that is, H_1 is highly correlated with the plantar-flexor joint torque and H_2 is highly correlated to the dorsi-flexor joint torque. This suggests that H_1 and H_2 may be the dual types of neural commands inherently delivered by the CNS for potential control of ankle joint torque. The analysis of synergy intensities could be further applied to FES to control co-contraction levels along with the joint torque control for ankle joint movement. We may stimulate the plantar- and dorsi-flexor muscles simultaneously under different pulse width levels to control the ankle joint torque and the joint stiffness by adjusting the co-activations of the plantar-flexor and dorsi-flexor actuators.

With regard to estimation performance, the synergy-space method is as accurate for inversely estimating muscle activations as the multiple regression method, as shown in Tab 5.1. In the isotonic condition, we compare the performances with and without information on joint position and velocity in order to see its impact. As we hope to achieve neuroprosthetic muscle control in the future by using averaged muscle synergy information, it would be interesting to see whether we can apply the average of the synergy information obtained from others to a specific subject. Tab. 5.2 shows the performance results of inverse estimation if we replace subject's normalized synergy ratio with the average one from nine other subjects. From the table, we see that the performance is somewhat degraded but acceptable. This implies that there may be some similarities in muscle synergy patterns among the able-bodied subjects, indicating that we might be able to apply others' average synergy patterns to a new subject for neuroprosthetic purposes, taking advantage of natural and optimal muscle controls from the intact CNS system. This suggests that, these able-bodied subjects possess similar synergies globally even if there are some individual characteristics, and thus the average synergy of others may be applied to an unknown subject as well. This concept can support the idea of using the generalized muscle synergy pattern to reproduce natural muscle combinations in the patient by means of neuroprosthetics. A recent work [Waltz, 2013], in which a patient with complete spinal cord injury was able to regain some motor functions by application of electrical stimulation to the spinal cord, has started to attract considerable attention. In their work, they applied machine learning to help optimally design stimulation patterns. Computer-based intelligent technologies have the potential to play a more active role in rehabilitation applications and in promoting the quality of life for motor-disabled individuals.

5.2.6 Conclusion

In this chapter, a synergy-based computational framework for the inverse estimation of multiple muscle activations is proposed and evaluated with experimental analysis. In this first trial, experimental validation is conducted with the ankle joint in isometric and isotonic conditions and the estimation of three muscle activations (SOL, MG, and TA). The synergies extracted by NMF helped to reduce the dimension to express the muscle activation patterns, the extracted synergies in ten subjects indicated both subject-specificity and similarity regarding the multiple muscle activation patterns. The model was cross validated on the prediction of multiple muscle activations with ten able-bodied subjects in order to evaluate the performance of this method. The approach was found to be promising for inverse estimation of the muscle activities expected from joint torque, both in isometric and isotonic contraction. Regardless of dimension reduction, the performance was not degraded compared with the result

TABLE 5.2: RMSE (%) and VAF (%) of inverse estimation by the synergy-based method in isotonic condition: every other nine subjects' normalized average synergy ratios are applied to replace the rest one's own synergy respectively for leave one-out cross validation.

Method		Synergy-based method	
Profile		$RMSE_{pr}$	VAF
V1	SOL	7.89	50.75
	MG	3.72	73.64
	TA	7.99	86.27
V2	SOL	22.52	42.79
	MG	12.97	59.96
	TA	13.82	72.15
V3	SOL	3.45	41.10
	MG	9.39	52.64
	TA	11.52	76.36
V4	SOL	12.21	36.57
	MG	8.95	61.11
	TA	6.15	88.09
V5	SOL	18.01	81.51
	MG	3.57	84.47
	TA	11.87	92.36
V6	SOL	10.21	59.98
	MG	21.64	43.79
	TA	4.57	89.14
V7	SOL	3.87	64.42
	MG	6.41	25.90
	TA	3.21	74.75
V8	SOL	1.28	68.09
	MG	0.55	39.96
	TA	2.78	95.80
V9	SOL	17.99	24.30
	MG	12.71	77.57
	TA	6.39	82.16
V10	SOL	6.10	84.42
	MG	23.55	38.30
	TA	3.75	93.56
Overall Average		9.30±6.40	65.39±21.32

with the multiple regression. The statistical analysis showed the significant similarity between methods. This suggests the usefulness of muscle synergy for inverse solutions as it can keep same prediction performance with natural muscle coordination information and in a reduced dimension space operation. In addition, the other one's averaged synergy ratio was applied for muscle activation estimation with leave-one-out cross validation manner, which resulted in 9.3% estimation error over all the subjects. This result supports the common muscle synergy based neuroprosthetics control concept.

In future work, we intend to investigate the inverse problem in the multiple joints situation, with the ultimate aim of achieving whole-body muscle activity estimation. The extracted information in this situation would undoubtedly be useful for the control of neuroprosthetic systems. The typical use of multiple muscles in able-bodied subjects could be reproduced for the artificial control of the muscles with multi-channel FES. The reproduced co-contractions would stabilize the joint, similar to the case of the natural motion employed by CNS.

CHAPTER 6

Personalized Home Rehabilitation

6.1 Toward Personalized Balance Measure at Home

The need for in-home care, monitoring, and rehabilitation of the elderly and impaired is increasing as the world population continues to age. The United Nations expects that 16% of the population will reach 65 years or older by 2015. This, together with the fact that falls are a leading cause of injury in the elderly [Painter et al., 2009], has prompted the need to remotely monitor the condition of older adults and provide them with an efficient rehabilitation tool for balance assessment. This has led many research teams to design non-intrusive surveillance tools: systems capable of recording gait parameters over time [Stone and Skubic, 2011], or of monitoring everyday activities [Patel et al., 2012].

Standing balance has been generally used to predict fall risks in elderly populations. For example, the BBS and the TUG are commonly used by clinicians to determine static and dynamic balance respectively [Langley and Mackintosh, 2007]. In a similar way, posturography, *i.e.* , the analysis of CoP trajectory, has shown that human balancing strategies change with age [Fujita et al., 2005].

In order to prevent falls, balance training is common after orthopedic surgery or cardiovascular accidents [Deutsch et al., 2009, Kennedy et al., 2011]. Some research teams have focused on creating preventive systems and promoting fitness training at home. For example, Kinect (Microsoft®, Redmont, WA, USA) based video games have been developed to encourage players to move while performing tasks designed to improve functional reach [Lange et al., 2011, Dowling et al., 2014]. Similarly, a WBB has been used to increase the range of CoP excursion during rehabilitation [Kennedy et al., 2011].

As with BBS and TUG, in practice, it is preferable to determine balance without the use of force platforms or force sensors in order to increase the patient's range of motion without requiring him/her to stand on top of the device. We propose to use video based motion capture to reduce the number of sensors attached to the subject for home-based applications. This would be useful for the analysis of unconstrained motion such as walking, StS, or general training specified by their therapists.

Several balance metrics have been developed for biped robots. One of the most widely used is the ZMP criteria developed by Vukobratović in the early 1970s [Vukobratovic and Borovac, 2004]. The ZMP concept has been successfully used to generate stable walking gaits, often through a simplified model involving the position and acceleration of the robot's CoM [Kajita et al., 2009, Erbatur et al., 2009, **?**]. In addition, it has been proven that the ZMP is equivalent to the CoP [Goswami, 1999, Sardain and Bessonnet, 2004]. Human balance may also be analyzed by studying CoM and CoP trajectories in both static and dynamic cases [Sardain and Bessonnet, 2004, Cotton et al., 2009]. The CoP trajectory is only defined inside the support polygon. A similar metric, the ZRAM point [Goswami and Kallem, 2004], is not constrained to the support polygon and can be

used to establish a criterion for determining if a movement can result in a loss of balance or a fall. That is, it can be used to determine if a step must be taken to avoid falling.

Any system estimating the position of the CoM in the home environment requires two key factors: portability, and a practical way of performing a self-identification procedure without the need for a long set up time. We previously presented the SESC [Cotton et al., 2009] and showed that it is possible to estimate a subject-specific CoM. Moreover, we applied the method using low-cost sensors like the Kinect [González et al., 2012, González et al., 2014], which can be used in the home environment. Our recent work [González et al., 2014] has focused on the validation of the use of the Kinect and the WBB for personalized CoM estimation using low-cost sensors against high-end sensors used in the laboratory environment. In this way we studied the portability of the system. The results of the SESC method were promising, but the identification process performed off-line had several drawbacks: (1) No indication of the identification quality was given to the subject in real-time. (2) There was no way for the subject to know if enough information had been provided for the identification. (3) Since no graphical interface was presented to the subjects, it was not possible for them to determine which postures to provide during the identification. In short: off-line SESC parameter identification is a long process, making it impractical for a home rehabilitation scenario, or a self-directed identification.

To address these issues, we expand the *on-line* identification of the SESC parameters, where a recursive algorithm is applied to identify a SESC. In the present study the SESC parameters are obtained *live* with the help of an adaptive interface, and information regarding the parameter identification process is given to the subject as visual feedback. In this way, the subject is free to create his/her own identification protocol; *i.e.* , they can interact with the interface and provide a variety of postures which he/she is comfortable and capable of performing. Here we test the hypothesis that visual feedback helps the subject to reduce the total time needed for the SESC parameter identification. We focus on the benefits that a user-friendly adaptive interface can have in home rehabilitation while providing a personalized CoM estimate by improving the self-identification of body parameters. Moreover, we compute a balance assessment using the ZRAM point [Goswami and Kallem, 2004] based on the trajectory of the personalized CoM estimation. This assessment is determined from kinematic measurements alone and may be used even when the subject is not standing on a force platform.

6.2 Related Works

Several studies recognize the role that sensory feedback plays on balance training, *e.g.* , immersive walking [Fung and Perez, 2011] and cycling [Song et al., 2004] simulators have been developed to help patients recover motor skills. These simulators were installed inside a laboratory and included: a treadmill with haptic feedback [Fung and Perez, 2011]; or a bicycle with force feedback [Song et al., 2004]. The effect of sensory feedback on the patient's balance was observed by asking the patients to move along a virtual path. Both of these studies reported improved performance when sensory feedback was introduced.

Other studies, such as [Czerwosz et al., 2009], focus on the role that visual feedback has on balance training. Their subjects were asked to change their CoP position while on-screen

feedback was given; the CoP sway was used as an indicator of balance. A similar system was implemented by Kennedy *et al.* [Kennedy et al., 2011] with a WBB. Using low-cost devices paves the way for balance training to be used in a clinical setting or inside the patient's home. The same idea was suggested by Lange *et al.* [Lange et al., 2011] and Dowling *et al.* [Dowling et al., 2014] when they proposed a Kinect based video game for functional rehabilitation. Under this paradigm, the elderly and balance impaired can profit from VR rehabilitation systems [Rendon et al., 2012, Kamieth et al., 2010] inside their homes.

Advanced VR rehabilitation systems for the elderly and the impaired should correctly evaluate a balance index during dynamic motion. However, these subjects can easily present a different mass distribution than that found in anthropometric tables [de Leva, 1996]. For example, post-stroke patients, hemiplegic subjects with asymmetric body mass distributions, and elderly or obese patients would present an atypical CoM location. If the average mass distribution parameters given in the literature were applied to them, the CoM estimation and subsequent balance evaluation could be inaccurate. This is why a subject-specific CoM estimation is important for rehabilitation.

Other studies make use of high-end motion capture systems to estimate the CoM position [Cotton et al., 2011, Schepers et al., 2009] but can not be used inside a patient's home due to cost and space limitations. Works like [Floor-Westerdijk et al., 2012] propose to use IMU to track the CoM position. This low-cost sensor approach is suitable for a home, but the method is only accurate for walking or quiet standing. This prompted us to design a portable, accurate, and *real-time* CoM estimation and visualization system to be used inside unstructured environments.

Ayusawa *et al.* [Ayusawa et al., 2013] have estimated center of mass and inertial parameters of both humans and humanoid robots. The same group has also developed an on-line parameter estimation tool capable of real-time feedback; which was given to the subject to improve the estimation [Venture et al., 2009]. The subject was shown a colored model that allowed him to recognize segments that still needed to be moved to improve the accuracy of the identified inertial parameters, but the impact of the system regarding the amount of time required for the identification was not reported. The method was also applied to determine subject-specific muscle strength [Hayashibe et al., 2011a]. In these studies the use of high-end motion capture equipment and sensitive force plate measurements was required.

This study investigates the performance of an adaptive identification tool using a Kalman filter. We analyze the effect that visual feedback may provide on the speed and quality of the identified SESC parameters. Visual feedback helps the subject better perform the identification protocol by assisting the decision regarding the postures to be performed. Additionally, we determine a measure of stability during dynamic motion by means of the ZRAM point determined using only the subject-specific CoM trajectory. This is a step towards practical usage of a personalized CoM estimation in home-based rehabilitation.

6.3 Method

6.3.1 Statically Equivalent Serial Chain

A linked chain's CoM position can be expressed in terms of its link orientations and a set of parameters determined by the link geometry and mass. This representation is equivalent to the geometric description of an open, virtual serial chain whose end-effector is the original chain's CoM. This virtual chain is known as the SESC [Cotton et al., 2009].

In order to estimate the CoM position for a human subject, we use a skeleton model composed of 9 links connected by 4 spherical and 4 hinge joints (see Figure 6.1). We associate a frame $\mathcal{R}_i$ to each link with the SESC parameters expressed with respect to those frames. The orientation between two frames is expressed using the rotation matrix $\mathbf{A}_i^j$. Additionally, the translational vector between two frames is written as $\boldsymbol{p}_i^j$. The CoM of a system with an n number of links, each with a mass m_i, can be represented by performing the matrix multiplication:

$$\boldsymbol{c} = \frac{1}{M}\sum_{i=1}^{n} m_i \left(\mathbf{A}_i \boldsymbol{c}_i + \boldsymbol{p}_i\right) = \begin{bmatrix} \mathbf{E} & \mathbf{A}_1 & \dots & \mathbf{A}_9 \end{bmatrix} \begin{bmatrix} \boldsymbol{p}_1 \\ \boldsymbol{r}_1 \\ \vdots \\ \boldsymbol{r}_9 \end{bmatrix} \tag{6.1}$$

where $\mathbf{E}$ is an identity matrix and $\mathbf{A}_i$ is the 3-by-3 orientation matrix of link i with respect to the global frame. The values in $\boldsymbol{r}_i$ can be explicitly determined as a function of the link masses (m_i), CoM positions in their local reference frames ($\boldsymbol{c}_i$), and $\boldsymbol{p}_i^j$. M is the total mass. The superindex 0 used to denote a position or orientation measured form the global reference frame has been omitted for convenience.

For our model, $\boldsymbol{r}_i$ is a constant 3-by-1 vector. This is due to the fact that only spherical and hinge joints were considered. Moreover, the CoM can be referenced to a floating frame attached to the skeleton at $\mathcal{R}_1$. Using the torso as a base for the SESC, (6.1) can be rewritten as follows:

$$\boldsymbol{c}^1 = \begin{bmatrix} \mathbf{A}_1 & \dots & \mathbf{A}_9 \end{bmatrix} \begin{bmatrix} \boldsymbol{r}_1 \\ \vdots \\ \boldsymbol{r}_9 \end{bmatrix} = \mathbf{B}\boldsymbol{r} \tag{6.2}$$

where $\boldsymbol{c}^1$ is the CoM position measured from the origin of $\mathcal{R}_1$, $\mathbf{B}$ contains the orientation matrices for all of the chain's links, and $\boldsymbol{r}$ represents a 27-by-1 vector of subject-specific parameters. The explicit expressions of $\boldsymbol{r}$ can be found in [González et al., 2014].

It was noted in [Cotton et al., 2009] that due to the SESC redundancy, there are several solutions to the identification problem. To constrain the solution, while hoping to find the one closest to our model, we put forward the following assumptions: (a) The floating frame $\mathcal{R}_1$ is attached to the skeleton at the torso. (b) As depicted in Figure 6.1, one axis of the associated reference frame $\mathcal{R}_i$ lies on the line segment connecting two joints. (c) The CoM position for all limb segments, $\boldsymbol{c}_i^i$, also lies on this straight line. The last two assumptions reduce the size of $\boldsymbol{r}$ once the rows which are known to equal zero are removed. Accordingly, $\mathbf{B}$ is reduced by removing the corresponding columns. In summary, $\boldsymbol{r}_1$ remains a 3-by-1 vector while $\boldsymbol{r}_{2\dots9}$ are represented

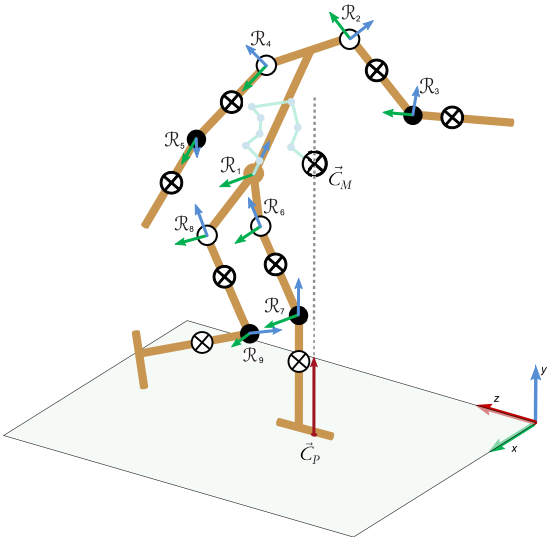

FIGURE 6.1: The skeleton model is composed of nine rigid segments. Shoulders and hips are represented with spherical joints, while elbows and knees are treated as hinge joints. The SESC is seen in blue. The CoM position is indicated by the last link of the SESC.

by one scalar each. The number of unknown SESC parameters was reduced from 27 to 11 constants which can then be estimated using recursive techniques.

6.3.2 SESC Parameter Identification and Visual Feedback using a Kalman Filter

To determine the geometric parameters of a serial chain such as the one described in (6.2), we use a recursive approach where each new measurement improves our knowledge of $\widehat{\boldsymbol{r}}$ [Mooring et al., 1991]. The Kalman filter can be used to determine a set of constant values from a group of noisy measurements. Consider the linear system described by:

$$\boldsymbol{x}_k = \mathbf{F}_{k-1}\boldsymbol{x}_{k-1} + \boldsymbol{w}_{k-1} \tag{6.3}$$

where the subindex k denotes the time step. The evolution of the state vector $\boldsymbol{x}_k$ is determined by $\mathbf{F}_{k-1}$ and a zero mean process noise $\boldsymbol{w}_k$ with covariance $\mathbf{Q}_k$. An estimate of vector $\boldsymbol{x}_k$ can be found from a number of $\boldsymbol{y}_k$ measurements. Each measurement is a linear combination of the states and a zero mean measurement noise $\boldsymbol{v}_k$ with covariance $\mathbf{R}_k$. Each measurement can be expressed in the form:

$$\boldsymbol{y}_k = \mathbf{H}_k\boldsymbol{x}_k + \boldsymbol{v}_k \tag{6.4}$$

where $\mathbf{H}_k$ is known as the configuration matrix.
The Kalman filter provides an optimal linear solution for systems defined by (6.3) and (6.4). When estimating a constant vector, the linear Kalman filter may be written as fol-

lows [Simon, 2006]:

$$\mathbf{P}_k^- = \mathbf{P}_{k-1}^+ + \mathbf{Q}_{k-1} \tag{6.5}$$

$$\mathbf{K}_k = \mathbf{P}_k^- {\mathbf{H}_k}^T \left(\mathbf{H}_k \mathbf{P}_k^- \mathbf{H}_k^T + \mathbf{R}\right)^{-1} \tag{6.6}$$

$$\widehat{\boldsymbol{x}}_k = \widehat{\boldsymbol{x}}_{k-1} + \mathbf{K}_k \left(\boldsymbol{y}_k - \mathbf{H}_k \widehat{\boldsymbol{x}}_{k-1}\right) \tag{6.7}$$

$$\mathbf{P}_k^+ = \left(\mathbf{E} - \mathbf{K}_k \mathbf{H}_k\right) \mathbf{P}_k^- \tag{6.8}$$

where $\mathbf{P}_k^-$ and $\mathbf{P}_k^+$ are the covariance matrices before and after the state update, $\mathbf{E}$ is an identity matrix of suitable size, and $\mathbf{K}_k$ is the optimal filter gain for minimizing the estimation error. Convergence of the estimation is reflected by the eventual decrease in the covariance matrix ($\mathbf{P}$) magnitude, as the confidence on the current estimate increases. That is, the estimation improves as $\mathbf{P}$ approaches zero.
In order to determine the effect that the adaptive visual feedback has on the identification, the color of each of the skeleton segments is varied to represent the convergence of the corresponding SESC parameters. $\mathbf{P}$ can thus be used to determine the color of each skeleton segment. $\mathbf{P}$ has a large value at the beginning of the identification: the skeleton is drawn completely in red. As $\mathbf{P}$ decreases the corresponding segments turn to green.

To perform a correct identification, a large number of measurements with an appropriate set of configuration matrices should be obtained. The orientation of each limb is directly measurable, but this is not the case for the subject's CoM. CoP offers a good approximation of the ground projection of CoM during quiet standing. This is due to the small CoM accelerations [Cotton et al., 2009] that occur in these postures. To determine if a posture is stable enough, we observe the CoP position and the limb roll-pitch-yaw angles during a one second window. We look at the standard deviation of both the angles and CoP values to determine if the pose was stable enough during this window to be used as identification data.

6.3.3 Zero Rate of change of Angular Momentum

The use of the ZRAM to determine the stability of humanoid robots during the single and double support phases was developed by Goswami [Goswami and Kallem, 2004] and originates from the same metric as ZMP control [Kajita et al., 2009]. The main difference between ZMP/CoP and ZRAM point is that the former are confined to the support polygon, while the latter can be used to determine a point on the ground where the reaction forces should be positioned in order to maintain balance.

For a walking robot on level ground, a sum of moments on its CoM can be written as:

$$\dot{\boldsymbol{\mathcal{L}}}_{\boldsymbol{c}} = (\boldsymbol{c}_p - \boldsymbol{c}) \times \boldsymbol{f} \tag{6.9}$$

where $\dot{\boldsymbol{\mathcal{L}}}_{\boldsymbol{c}}$ is the rate of change of angular momentum, $\boldsymbol{f}$ is the vector of reaction forces and $\boldsymbol{c}_p$ gives the point of its application. The ZRAM point is defined as the position on the ground where $\dot{\boldsymbol{\mathcal{L}}}_{\boldsymbol{c}} = \mathbf{0}$, *i.e.* , the action line of the ground reaction force passes through the CoM. Let $\boldsymbol{p}_0$ represent a point on the ground plane and $\boldsymbol{n}$ a vector normal to the plane, then the ZRAM point can be determined as follows:

$$\boldsymbol{p}_f = \frac{(\boldsymbol{p}_0 - \boldsymbol{c}) \cdot \boldsymbol{n}}{\boldsymbol{f} \cdot \boldsymbol{n}} \boldsymbol{f} + \boldsymbol{c} \tag{6.10}$$

Unlike ZMP and CoP, the ZRAM point may exit the support polygon. This excursion can be seen as an unstable situation and used to provide a dynamic measure of balance but does not predict a fall. Falling may still be avoided if a step is taken or the limbs are used to balance. A full dynamic analysis is necessary to determine if a fall cannot be avoided.

Kajita *et al.* [Kajita et al., 2009] present an equivalence between the sum of forces acting on a linked chain and the acceleration of its CoM.

$$\boldsymbol{f} = M\left(\ddot{\boldsymbol{c}} + \boldsymbol{g}\right) \tag{6.11}$$

where M is total mass of the chain and $\boldsymbol{g}$ the acceleration of gravity. Using (6.10) and (6.11), the ZRAM point can be determined from the trajectory of CoM alone, without the need for external force sensors.

Measuring Balance

Whenever the CoP is measured (by means of a force platform), $\dot{\boldsymbol{\mathcal{L}}}_{\boldsymbol{c}}$ can be used to evaluate balance. It is obtained from (6.9) and it should remain close to zero for stable motions. On the other hand, the ZRAM point can be obtained and used to evaluate balance in the absence of CoP measurements. We propose to use the position of the ZRAM point ($\boldsymbol{p}_f$) with respect to the center of the support polygon to determine stability [Goswami and Kallem, 2004]. We distinguish two cases. (i) A single support phase where the distance of the $\boldsymbol{p}_f$ to the ankle is found as

$$d = \|\boldsymbol{p}_{l,r} - \boldsymbol{p}_f\| \tag{6.12}$$

where $\boldsymbol{p}_{l,r}$ is the three-dimensional position of the support ankle (left or right). (ii) A double support phase where we determine the distance of $\boldsymbol{p}_f$ to the line defined by both ankles. When this line is expressed as a function of the left ankle position and of the unit vector $\boldsymbol{v} = (\boldsymbol{p}_r - \boldsymbol{p}_l)/\|\boldsymbol{p}_r - \boldsymbol{p}_l\|$, the distance between $\boldsymbol{p}_f$ and the line can be found as

$$d = \|(\boldsymbol{p}_f - \boldsymbol{p}_l) - ((\boldsymbol{p}_f - \boldsymbol{p}_l) \cdot \boldsymbol{v})\,\boldsymbol{v}\| \tag{6.13}$$

6.3.4 Experiment

Eight healthy volunteers (two females, and six males, age = 27±3.0 years, weight = 76.4±20.9 kg, height = 1.76±0.06 m), were asked to participate in this study and gave their informed consent. The subjects had never participated in a SESC parameter identification before. The subjects were asked to stand on top of a WBB and to maintain a series of static postures. They were also asked to hold each posture for approximately two seconds before changing to a different one. No instructions were given regarding the number or type of postures to perform, but they were asked to move all joints during the experiment.

The procedure was performed three times: (i) once without visual feedback of the identification status; (ii) once with visual feedback (where the skeleton color indicates the SESC parameter covariance); and (iii) a final recording without feedback to be used as cross-validation for the identified SESC model. That is, in (i) and (iii) the subject can observe the skeleton in

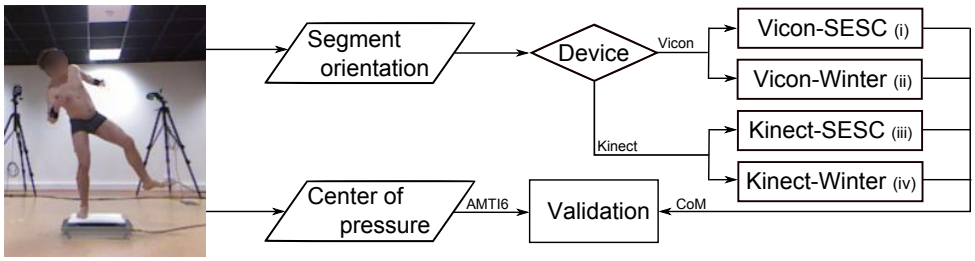

FIGURE 6.2: Using the same static postures, the volunteer's CoM is estimated from laboratory-grade measurements with: (i) an SESC and (ii) anthropometric values. To validate the use of low-cost sensors the CoM, estimation is repeated using (iii) an SESC and (iv) anthropometric values.

real-time but without a color change, and in (ii) the subject can observe the skeleton changing colors in real-time as the covariance of each SESC parameter changes during the identification.

The Kinect sensor was placed three meters away from the subject on the WBB. Both the depth information from the Kinect ; and the force and CoP data from the WBB were recorded synchronously using a custom application capable of reading and storing data. A custom program was created in C++ to: (1) Collect and save and data. (2) Display the information in 3D. (3) Allow user input for navigation in a 3D environment. (4) Identify the SESC parameters online. (5) Give visual feedback to the user/subject regarding the SESC parameter identification status.

Handling of the Kinect (Microsoft®, Redmont, WA, USA) and WBB sensor (Wii balance board by Nintendo® Co., Ltd., Kyoto, Japan) was managed using open-source code from *OpenNI* (PrimeSense, Ltd., Tel Aviv, Israel) [PrimeSense Inc.,] and the *WiiUse* project [Pavlik,], respectively. The visual interface was created using the OpenGL `GLUT` library, while OpenCV was used to perform the necessary matrix operations. The created software allows us to draw in 3D: the skeleton provided by *OpenNI* , the time-varying color information representing the Kalman filter's state convergence, the SESC, and the resultant CoM position estimated with the current model.

6.4 Results

6.4.1 Comparison: High-end vs. Portable sensors

In this work, we proposed a new method for estimating the whole body center of mass that can be used outside of the laboratory by utilizing the statically-equivalent serial chain and a Kinect. We evaluated the differences between the SESC's CoM estimate obtained from Vicon-AMTI6 data to one created using the Kinect-WBB. For this purpose, the SESC parameters were identified twice over the same static postures, using low-cost and high-end equipment. For completeness, the CoM was also estimated using anthropometric table data [Winter, 1990] to compare these results to the SESC estimate. Figure 6.2 summarizes this process.

Figure 6.3 shows the averaged rmse of the estimation for all subjects and all po-

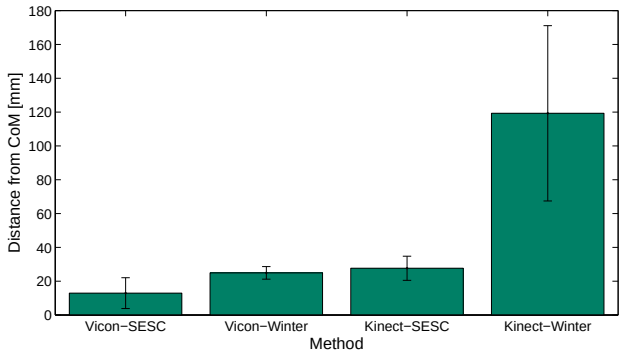

FIGURE 6.3: Summary of the performance of each CoM estimation method. The bars correspond to the rmse $\pm$ std averaged for all subjects. We observe an increase in the accuracy of the identified SESCs with respect to the literature estimates. In addition, the performance of the Kinect-SESC was found to be equivalent to that of the literature-based estimate using high-end sensors.

stures. The best performance was the (i) case with a 12.89 ± 9.11 mm average error. The (ii) and (iii) cases performed similarly to each other. The largest estimation error came from case (iv) using literature values with Kinect measurements. Table 6.1 shows the mean and std of the rmse for the (i)–(iv) estimations. This table also shows the error in the subjects' AP and ML directions and the coefficient of determination of each case compared to the CoP measurements of the validation posture set.

TABLE 6.1: The root mean square error (rmse) for each CoM estimation method, in cross-validation. The error is measured in the world reference frame, averaged for all subjects $\pm$ std. anterior-posterior (AP) and medio-lateral (ML) give the anterior-posterior and medio-lateral direction errors, respectively. R^2 is the coefficient of determination of the cross-validation set.

CoM Estimation	**Error (mm)**	**AP (mm)**	**ML (mm)**	$\mathbf{R^2}$
Vicon-SESC	12.8 ± 9.1	10.40 ± 6.6	10.2 ± 6.9	0.9 ± 0.1
Vicon-Winter	24.9 ± 3.7	23.16 ± 5.9	13.9 ± 7.3	0.8 ± 0.1
Kinect-SESC	26.6 ± 6.0	23.37 ± 6.8	17.1 ± 8.0	0.8 ± 0.2
Kinect-Winter	118.4 ± 50.0	94.82 ± 70.2	51.8 ± 24.2	-2.8 ± 6.9

The validation of human CoM estimation methods is an open problem, as this quantity cannot be directly measured. The segmentation method, using laboratory instruments and anthropometric tables, is considered as the standard for whole body CoM estimation [Lafond et al., 2004]. However, no study to our knowledge has yet investigated the possibility of using low-cost instruments to provide a subject-specific CoM estimation. We evaluated the accuracy of portable sensors (the Kinect and the WBB) to estimate CoM by comparing it with that obtained with conventional sensors (Vicon and an AMTI6 force platform). With the Vicon system, the estimation error of the literature-based CoM estimate was found to be

24.9 $\pm$ 3.7 mm; this error was reduced to 12.8 $\pm$ 9.1 mm using the SESC method. With the Kinect, the literature-based estimate had an error of 118.4 $\pm$ 50.0 mm, while the subject-specific SESC error was 26.6 $\pm$ 6.0 mm. We find that the subject-specific SESC estimation with low-cost sensors performed as well as a literature based one with high-end sensors.

Regarding CoM estimation accuracy, we improve on the literature due to the SESC's subject-specific nature. Figure 6.3 focuses on this. A lower rmse was observed with the Vicon-SESC method than the literature sources [Winter, 1990]. Similarly, using literature values with the Kinect (iv) results in large estimation errors (see Table 6.1). The SESC estimate for the Vicon-SESC has the same error magnitude for both the AP and ML directions, whereas the Kinect-SESC has a larger mean error on the AP (depth) direction than the ML one. This might be due to the noisy joint positions given by the Kinect skeleton, as only one camera is available to reconstruct the kinematics. In contrast, the Vicon skeleton offers better-defined joint obtained from the markers' positions. Finally, the performance of the Kinect-SESC estimate approaches the Kinect's known measurement error. The Vicon-SESC estimate error is larger than that of the Vicon's measurement. This is probably due to the simplified skeletal model.

A two-way ANOVA test was performed to determine the influence of the sensor (Vicon or Kinect) and of the origin of the parameters (Winter or SESC) on the rmse. A significant effect was found from both factors ($p < 0.01$). Additionally, a strong interaction of both factors was found ($p < 0.01$), suggesting that the low rmse found for the Vicon-SESC case was due to both the SESC method and the high-quality measurements of the Vicon system.

6.4.2 Convergence- Skeleton coloring feedback vs. no feedback

SESC identification is performed and compared between: (i) without color visual feedback and (ii) with color feedback. The color indicates the status of the on-going identification. For (i), the skeleton was visible but its color remained red. In Fig. 6.4 we show the adaptive interface for the identification used for (ii). The current CoM estimate is also visible. The skeleton color gradually changes from red to green indicating the convergence of the SESC model. The color change is determined from the magnitude of the SESC parameter covariance. We observe a high estimation error for the first frames and the CoM gradually entering the subject's body as the identification proceeds. In this figure, we see the gradual change in limb color. This happens as the confidence on the limb parameters increases as a larger amount of significant information is gathered. In Fig. 6.4, we see that the arms are the first segments to turn green; the subject presented them in many different orientations before moving the legs or thorax. With this interface, the subject understands which segments should still be reoriented. Fig. 6.5 represents the mean covariance value among the SESC parameters for all eight subjects. We show both cases: (i) seen in red, and (ii) in blue. The center line represents the mean value while the surrounding colored area shows the STD range. The feedback effect is visible. It reduces the overall parameter covariance, as well as their STD. As a result, we observed a faster convergence of the SESC parameter identification in (ii) than in (i).

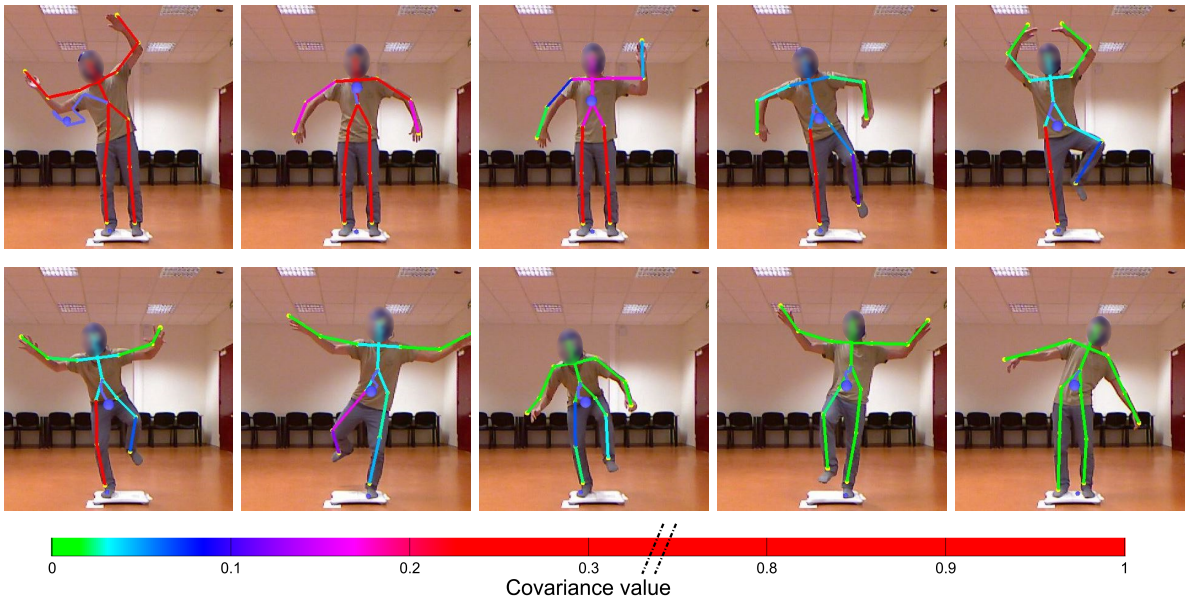

FIGURE 6.4: Adaptive interface for personalized center of mass estimation: The skeleton color changes from red to green indicating the convergence of the SESC model adaptively identified by the Kalman filter. Each segment color is determined by its respective covariance, where the highest value corresponds to red. The current CoM is also visible. We observe a high estimation error for the first frames and the CoM gradually entering the subject's body as the parameter identification proceeds. A video showing the identification procedure is available at http://youtu.be/J-yqOzRK5Ts.

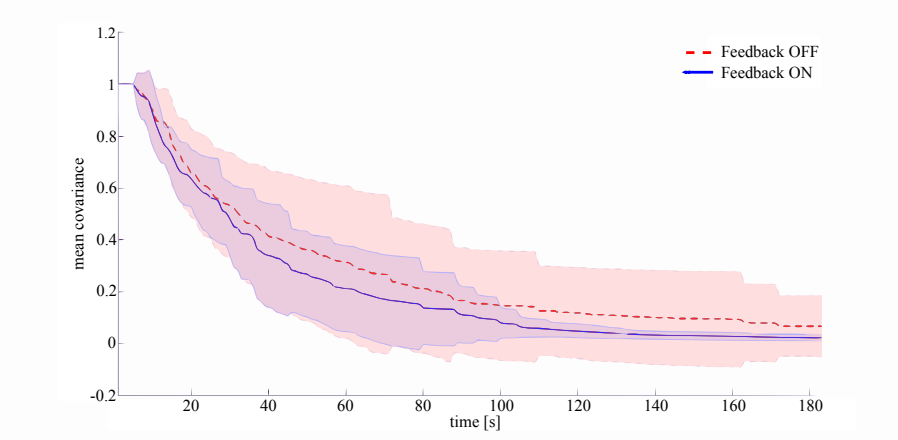

FIGURE 6.5: Mean and standard deviation of the maximum covariance among SESC parameters for all eight subjects during on-line identification. The red line shows the results without the adaptive interface while the blue line shows the results with the interface. The colored areas show the STD for each case. It is visible for the effects of the visual feedback on identification.

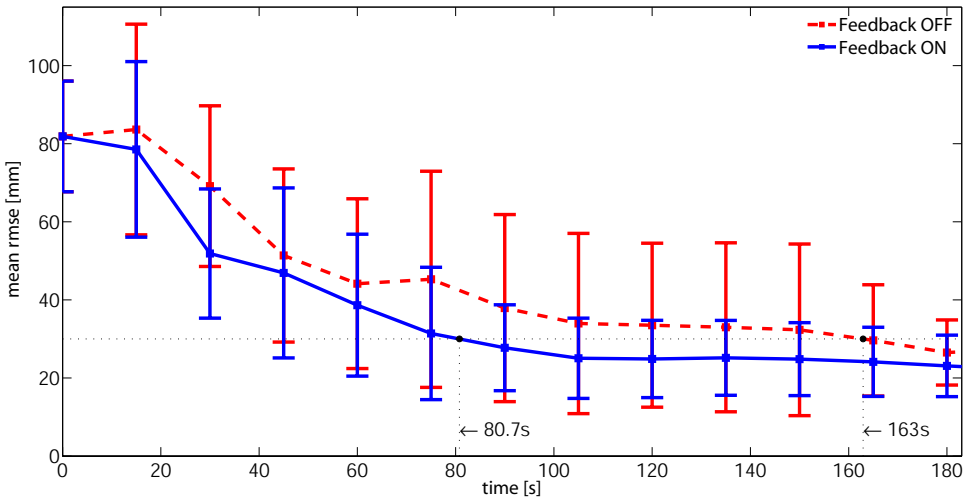

FIGURE 6.6: Root mean square error of the CoM estimation and standard deviations plotted against time averaged for all eight subjects. Convergence of CoM estimate appeared faster with the adaptive interface case. The CoM accuracy is also improved via the interface. For example for the same $RMSE$ error, almost half the time is required when the adaptive interface is provided.

6.4.3 Cross-validation with a new motion set

Cross-validation with a new motion set was done to evaluate the identified SESC model in terms of CoM estimation. The final SESC parameters from the (i) and (ii) recordings were used to estimate the subject's CoM during a third trial and compared to the measured CoP. Fig. 6.6 indicates the average $RMSE$ of the CoM estimation as a function of time spent in identification. SESC parameters obtained at 15 s intervals were used to estimate the CoM position of the cross-validation trial. The average $RMSE$ value decreases over time. That is, the overall identification improves as the time spent on identification increases. We observed faster convergence of CoM estimate when the adaptive interface was used. These results may serve as a guideline for the identification phase. To obtain an $RMSE$ of 30 mm, the identification time could be halved, *i. e.* , dropping from 163 s without visual feedback to 80.7 s with it.

6.4.4 Postural Stability Index

As an application example, we monitor the stability of a dynamic movement using the personalized CoM trajectory. The ZRAM point is used for this purpose. We consider a stable motion to be one where the ZRAM point remains inside the support polygon.

In Fig. 6.7, we show the distance between the $\boldsymbol{p}_f$ and the support polygon for a dynamic motions for which the subject did not stand on top of the WBB, that is, CoP position cannot be measured. Additionally, the ZRAM point is shown as a pink sphere in the ground plane. Starting from a stable position (A) the subject lifts her right leg initiating a single support phase. At this time the ZRAM point is far from the left ankle and the skeleton's red color reflects the unstable situation (B, C). To maintain balance, this motion required the subject to accelerate her

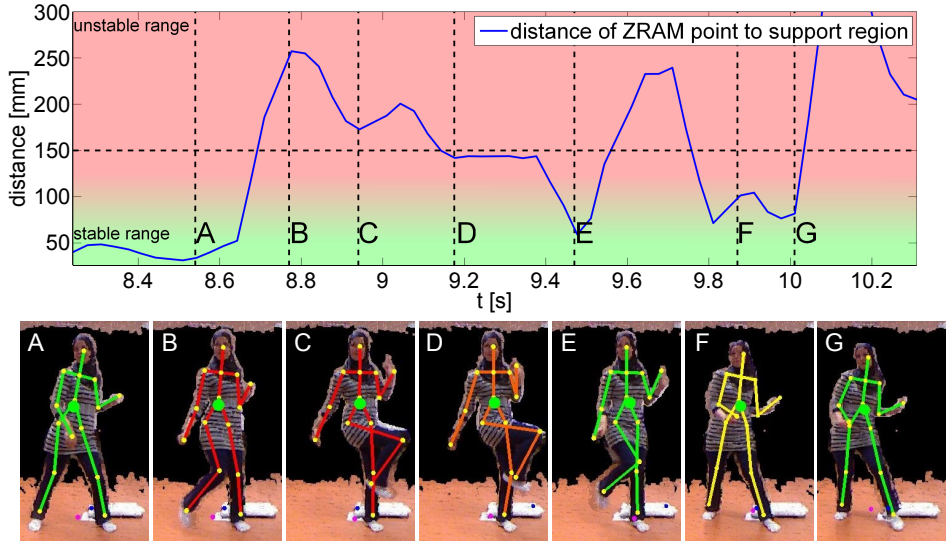

FIGURE 6.7: The distance between the ZRAM point ($\boldsymbol{p}_f$) and the center of the support polygon can be used to determine balance during dynamic motion. A value of 150 mm roughly corresponds to the edge of the support polygon, all greater distances place $\boldsymbol{p}_f$ outside of the polygon indicating an unstable situation. This stability metric can be obtained in real-time and shown to the subject. In this example, the subject's skeleton is colored in red to indicate an unstable movement and in green for a stable one.

CoM in order to place it over the left ankle. This moves the ZRAM point towards the ankle increasing subject stability and the skeleton color changes accordingly (D). At the end of the motion (E) the subject is stable over her left foot. Finally, the subject lowers her leg regaining a standing position. The CoM accelerates to the right and the ZRAM point moves away from the left ankle (F), this is seen as an unstable motion. Balance is regained by enlarging the support polygon by means of a double support phase (G).

6.5 Discussion

We tested the hypothesis that an adaptive visual feedback during the SESC parameter identification may reduce the total time needed to establish a personalized CoM estimation. When they performed the identification procedure with the help of the adaptive interface, each subject was also able to see the color change and was asked to make the skeleton green. The addition of an adaptive feedback interface reduced the average $RMSE$ values across all subjects and across all trials. It also decreased the average parameter covariance. In this way, the model could be established faster. To obtain an $RMSE$ of 30 mm, the identification time could be halved, going from 163 s without visual feedback to 80.7 s with it. Conversely, a lower error was found for the same identification time. For an identification session of 120 s in length, $RMSE$ was of 24.8 mm when feedback was provided, and 33.5 mm when it was not.

We believe that the improvement on the identification accuracy is due to the increased amount of information that the subjects were able to present to the identification algorithm.

The subjects were able to interpret the color-based feedback as an indication that he/she should perform a different posture to continue changing the color of the skeleton. In this way, the subject can use the adaptive interface tool to perform the parameter identification in a self-directed manner and in the home environment.

6.6 Conclusion

In this study, we propose an adaptive feedback interface which shows the convergence status of SESC parameters facilitating self-identification inside the home environment. The display of the identification quality resulted in faster convergence and a higher accuracy of the CoM estimation when the adaptive interface was active. This interface can contribute to a personalized CoM estimation with a practical identification time length (around two minutes). A portable CoM estimation that was also able to support a self-identification procedure would be promising to obtain a reliable postural stability measure in home rehabilitation. Fall risks and subject balance improvement during training would be accurately evaluated when considering subject-specificity. Such balance evaluation study in clinical application with the proposed method is scheduled as part of our future work.

After the SESC model is identified, a personalized CoM estimate can be obtained only using Kinect information. The CoM estimated with the SESC model is also valid for dynamic motions; the static postures (and WBB) are only necessary during the identification phase. Thus, a personalized balance stability evaluation is available through the ZRAM point. The work we present here is a step towards the determination of a personalized measurement of human balance that is adapted to low-cost sensors and that can be used in the home rehabilitation.

CHAPTER 7

Synergetic Motor Learning Control

7.1 Human Motor Learning Control in Redundancy

The use of bioinspired approaches [Ijspeert et al., 2007][Shimoda and Kimura, 2010] is rather appealing in controlling articulated robots with redundancy such as Humanoids. Even after recent progressive development of humanoid robotics all over the world, a performance of advanced humanoid is still highly limited especially for the case under new and unknown dynamic environment. When the given dynamics can be written with explicit equations both for the environment and the robot manipulator itself, and if it is especially for predefined tasks, the humanoid performance can be higher than the human skills. Such capability is benefitted from the model-based control and the knowledge of detailed dynamics and high-speed actuators without fatigue phenomena differently from the slow fatigable muscle actuators embedded in the human system [Hayashibe et al., 2011c]. Whether or not we can have a prior knowledge of the dynamics information brings significant differences in humanoids performance. The gap is huge than we imagine from their fascinating movement during the demonstration which is well prepared in advance.

The key to fill the gap between human and humanoid motor control ability is learning and adaptivity, coordination of multiple (redundant) joints, computational framework with modularity, and optimality principles for motor execution toward energy efficiency. In human motor learning control, it has all the above listed capability in seamless and synchronous manner. In contrast, humanoid study tends to use separated component to deal with each feature. For instance, using the explicit dynamics model, some researchers have been dealing with redundancy by applying mathematical optimization. Often, there is no learning feature in such optimization or it is dealt with separated components then it is hard to deal with two criteria in different aspects. In humans, our skeletal system has more degrees of freedom (DOF) than the number of dimension in our task space. Taking advantage of dexterity from redundancy, human can learn new skill and with dynamic adaptivity while keeping certain motion accuracy but also finding easier motor coordination considering our physical biomechanical conditions. Found motor solutions are energetically efficient taking into account our articulated body dynamics [Izawa et al., 2008]. Thus, the human motion is not always so precise. It means when we ask the subject to draw straight line in front of his body in pointing task, that line is often not completely straight since we tend to move in comfortable way, which is dynamically energy efficient to drive our multi-linked chains. This phenomenon is a proof of multi-criteria. In addition, the human control can change the combination of criteria depending on the way of instruction and their motivation. We have an ability to increase the precision of the straight line if the instructor looks serious while indicating our task. Basically, making a precise motion is more energy consuming as we can imagine easily from the example of high-gain Proportional-Derivative control to remove the error. Human motor control has a good flexibility to handle the dual conflicting criteria. When it seems not necessary to be so precise, we can find a good compromise naturally between the motion accuracy and the energy efficiency.

7.2 Modular Model-free Optimization Process

Such general ill-posed problem of DOF was originally formulated by Bernstein [Bernstein, 1967] as the DOF problem. It is still open problem to answer how motor controllers in the central nervous system (CNS) solve kinematic redundancy with multi-criteria. In this scientific problem, so-called cost function based mathematical optimization is a state-of-art approach to solve such ill-posed problem [Braun et al., 2009][Todorov, 2004] in computational neuroscience.

Several types of optimality model have been proposed. Such model is often defined as 'minimum X', where X can be jerk, torque changes [Uno et al., 1989], motor command [Harris and Wolpert, 1998] and energy consumption [Alexander, 1997]. In redundant manipulators, such cost function based optimal control was successfully applied in [Todorov and Jordan, 2002][Guigon et al., 2007]. In robotics, several methods were studied to deal with the redundancy [Nakamura, 1991, Arimoto and Sekimoto, 2006]. They basically assume the use of a physical inverse dynamic model [Nakanishi et al., 2008] or approximation-based model [Peters and Schaal, 2008]. The cost function is commonly designed for the optimization process.

As for model-free approach, adaptive feedback control is known in control society. However, adaptive control can not be applied to redundant systems without using cost function based a-priori optimization. Feedback-error-learning (FEL) is well studied to provide computational adaptation paradigms [Kawato and Gomi, 1992]. FEL is proven as a special form of adaptive feedback control [Nakanishi and Schaal, 2004]. Then it does not provide a mechanism that can systematically improve performance toward optimal solutions under redundancy.

Final solution likely performed by human can be obtained with optimization approach. However, mathematical optimization basically requires the dynamic model of the system and involves complex computation. In addition, such computational operation requires a global image of the system and to know the overall variables at different levels in the system, which is a quite complex process to be embedded in the CNS as a modular configuration [D'Avella et al., 2003][Tagliabue and McIntyre, 2014].

We may remind that central pattern generators are likely embedded in the spinal level rather than the cortical level. A spinal brain concept is recently proposed by [Courtine et al., 2009] where they found adaptive function even from spinal level coordination. Modular computational principle which can handle total system optimization is preferred to be considered as an embedded algorithm in the spinal side of CNS. However, the current mathematical optimization is not a module-oriented computational operation. If we could find an alternative modular algorithm which can manage to induce the total system phenomenological optimization, it could be a candidate as a computational principle to be likely embedded in the spine.

Recently, a novel learning scheme named *Tacit Learning* was developed [Shimoda et al., 2013] as an unsupervised learning paradigm. The experimental results demonstrated that the walking gait composed of primitive motions was well adapted to the environment in terms of walking efficiency [Shimoda et al., 2013]. Based on the tacit learning, we reformulated the paradigm as a supervised learning approach applied to cyclic reaching tasks using the feedback motor command error as a supervising signal. Synergetic learning

control (SyLC) paradigm is proposed to systematically induce the motor synergy emergence in reaching task [Hayashibe and Shimoda, 2014]. It is a modular computational paradigm to realize both adaptability and optimality in a redundant system with a dynamic-model-free and cost-function-free approach [Hayashibe and Shimoda, 2014]. It demonstrated to produce energy efficiency while finding a way to compensate the interaction torques in multijoint reaching, which was only verified in the computer simulation with the environment produced with Open Dynamics Engine. Here, we aim to investigate the feasibility of Synergetic Learning Control (SyLC) paradigm to be applied for redundant articulated robot with physical electromechanics in this paper.

It would be highly beneficial for controlling articulated robots as bioinspired solutions, which can provide also an insight on human motor control. The seamless learning and control is an important aspect, which is difficult to be managed with conventional model-based optimization in robotics. It is a step forward toward bridging the gap between learning and control in robotics. It is not realistic to apply mathematical optimization every time the dynamic environment is changed as it happens at any time in general robot control with environmental interaction. In addition, how we can switch time-variant model during optimization computation and during motor control is not yet solved even as a mathematical problem in model-based approach. Furthermore, the issue of how such exact model description is obtained for time-variant physical environment would also limit the application of model-based optimization in humanoid control in a real world.

7.3 Redundant Robot Configuration

Our skeletal system has complex series of linkages that produce coupled dynamics. For instance, when we quickly move our forearm by flexing the elbow joint, the flexion torques on the elbow joint accelerate our forearm. However, due to the forearm's inertia, this acceleration produces torques also on the shoulder. These interaction torques induce the undesired effect of accelerating the upper arm segment. The dynamics of multijoint limbs often causes such complex torques especially during vertical reaching task due to the gravity. In human control, the able-bodied subject can easily handle such interaction torques with motor learning and its predictive control [Shadmehr and Wise, 2005][Bastian et al., 1996]. In this work, we aim to verify the performance of redundant manipulator driven by synergetic learning control under vertical reaching as the configuration used in [Bastian et al., 1996].

In a sagittal plane, 3 Degrees-of-Freedom (DOF) composed of shoulder, elbow, wrist joint was arranged as illustrated in Fig.7.1. The upper arm, forearm and hand segments were connected through each joint. Each joint is actuated using a DC motor with an encoder and a Harmonic Drive gearing for backdrivability as depicted in Fig.7.1(a). 10W motors are used for Joint 1 (Shoulder) and 2 (Elbow), and 4.5W motor is used for Joint 3 (Wrist). The ratio of the gears is all 1/100. The motor located below Joint 3 is used to grasp the object by the hand. Each motor is current-controlled with servo-amplifier drives. Thus, each joint has a local torque control to generate the specified joint torque by the synergetic learning controller for the robot. The control algorithms are executed on a master PC with the interface of AD and DA converters

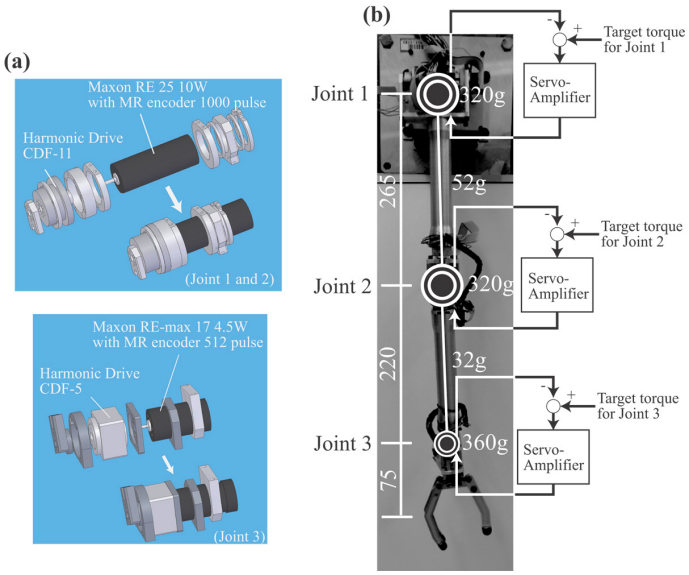

FIGURE 7.1: 3DOF Manipulator for Experiments: **(a)** structures of motor component: Each joint consists of a DC motor with an encoder and a Harmonic Drive gearing. **(b)** Overview of the 3DOF manipulator with some parameters. Each joint has the local servo-amplifier to create the targeted joint torque.

from the encoders and to the motors. This manipulator is redundant as the motor axes are in parallel. Some manipulator parameters are described in Fig.7.1(b).

We perform the control of this robot only with the proposed learning controller without using the explicit dynamics equations of the robot. Thus, we have an access only to the control of each joint torque and no access to the manipulator dynamics model in the learning process. It should be noted that this configuration is in so-called Bernstein's DOF problem where we have actuation redundancy since the task is performed in 2D with 3DOF manipulator.

7.4 Synergetic Learning Control via Tacit Learning

Synergetic Learning Control (SyLC) scheme for reaching motion of redundant robotic manipulator is represented as in Fig.7.2. The block diagram is formulated as a supervised learning paradigm using the feedback motor command error. Conceptually, it has an approach in common with FEL in how to use feedback errors as supervising signals [Kawato and Gomi, 1992]. However, in FEL, prior optimization is still necessary to achieve optimality for redundant system [Schweighofer et al., 1998]. Thus, we aim to provide a primitive mechanism for realizing such optimality without using cost function. As in the mechanism of the cerebellum with regard to long-term associative potentiation/depression, simple tacit learning with torque signal accumulation is employed to realize both adaptation and optimal control synchronously. We assume only forward kinematics (FK) information is available. The multijoint dynamics information is blind for the learning controller, thus this paradigm is to find a way to manage interaction torques through the repetitive interactions with the environment.

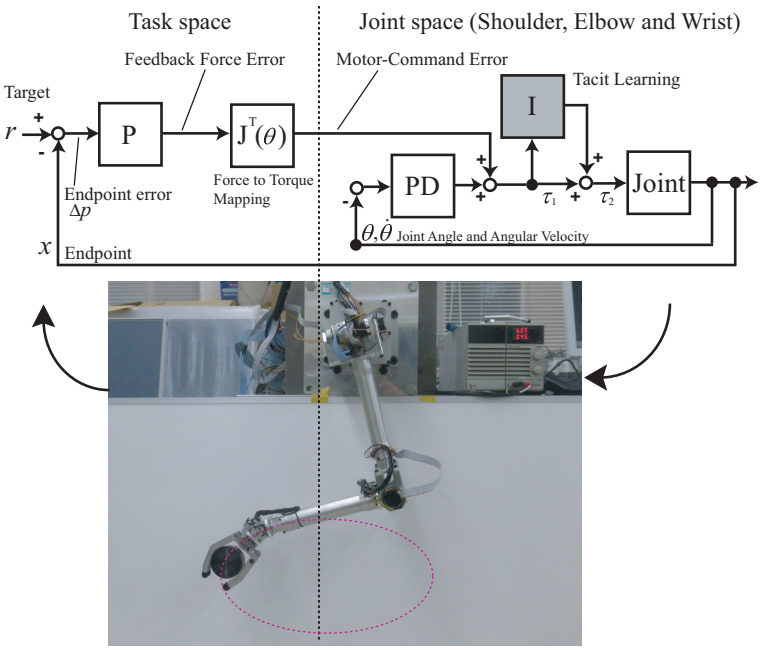

FIGURE 7.2: Synergetic Learning Control (SyLC) scheme for reaching motion of redundant robotic manipulator. The robot has 3 DOFs of the shoulder, the elbow and the wrist. The task is to track the moving target for 2D ellipsoidal trajectory while holding a load at its hand without the prior knowledge of its dynamics information. P represents Proportional, D Derivative and I the Integral controller, respectively. The box named joint represents the physical joint of the arm. The intentional target is expressed by a force vector in the task space, which represents the direction and distance to the target, using the proportional feedback error between the target and current endpoint. The feedback torque command error at each joint space is computed through the Jacobian of the arm by mapping the feedback force into the joint torque space. Local PD control represents the local reflex loop as a function of a muscle spindle. The torque command accumulation part in gray color corresponds to tacit learning.

The proposed synergetic learning control paradigm shown in Fig. 7.2 consists of these separated elements in loop:

1. The intention to follow the target is expressed by a force vector in the task space, which represents the direction to the target, and the distance as its intensity, using the proportional (P) feedback error between the target and current endpoint.

2. The feedback force error is mapped through the Jacobian of the arm into the joint torque space. It can be regarded as motor-command error that works as a supervising signal, as in FEL.

3. Local proportional derivative (PD) control mainly corresponds to a local reflex loop as a function of the muscle spindles. This part basically contributes to changing the joint angles smoothly.

4. Torque command accumulation part shown as gray box corresponds to tacit learning. This Integral (I) part serves as a unique learning process. This motor command accumu-

lation part starts to learn how to compensate the interaction torques, and turns into a predictive torque patterns for a given repetitive task.

Specifically, the controllers for PD feedback and synergetic learning control can be expressed as follows.
PD feedback:

$$\boldsymbol{\tau}_1 = -\boldsymbol{J}^T(\boldsymbol{\theta})k\Delta\boldsymbol{p} - \boldsymbol{A}\Delta\boldsymbol{\theta} - \boldsymbol{B}\dot{\boldsymbol{\theta}}. \tag{7.1}$$

Synergetic learning control:

$$\boldsymbol{\tau}_2 = -\boldsymbol{J}^T(\boldsymbol{\theta})k\Delta\boldsymbol{p} - \boldsymbol{A}\Delta\boldsymbol{\theta} - \boldsymbol{B}\dot{\boldsymbol{\theta}} + \boldsymbol{C}\int \boldsymbol{\tau}_1 dt. \tag{7.2}$$

$$\boldsymbol{\tau}_1, \boldsymbol{\tau}_2, \Delta\boldsymbol{\theta}, \dot{\boldsymbol{\theta}} \in R^m, \Delta\boldsymbol{p} \in R^n, \boldsymbol{J}^T(\boldsymbol{\theta}) \in R^{m\times n}, \boldsymbol{A}, \boldsymbol{B}, \boldsymbol{C} \in R^{m\times m}$$

where, m is the number of the joints, n is the task space dimension, $\boldsymbol{\tau}$ implies the control torque inputs of the joints, $\boldsymbol{\theta}$ implies the angles of the joints, $\dot{\boldsymbol{\theta}}$ implies the angular velocities of joints. $\boldsymbol{J}^T(\boldsymbol{\theta})$ is the transpose of the Jacobian of the arm, k is the gain of the task space proportional feedback, $\Delta\boldsymbol{p}$ is the endpoint error vector. The first term in (7.2) corresponds to the neural substrate of force mapping functionality presumably due to corticospinal control [Bizzi et al., 1991].

$\boldsymbol{A}$ and $\boldsymbol{B}$ are diagonal matrices which consist of the proportional and derivative gains of the PD controllers of local joint. $\boldsymbol{C}$ is a diagonal matrix which consists of the gains of the torque command integration regarding motor-command error and local feedback torque. The term $\boldsymbol{A}\Delta\boldsymbol{\theta}$ is optional, and it can be set if you specify the neutral position of the joint. In this work, this neutral position is specified only for the wrist joint, because the wrist tends to return to the central position when we relax.

As for local PD feedback, this part corresponds to a local reflex loop as a function of the muscle spindles [Shadmehr and Mussa-Ivaldi, 1994]. When a muscle is stretched, primary sensory fibers of the muscle spindle respond to changes in muscle length and velocity. The reflexivity evoked activity in the alpha motoneurons is then transmitted via their efferent axons to the muscle, which generates force and thereby resists the stretch.

Note that all joints are controlled independently except the task space operation, then the control configuration has a modular structure. All dynamical parameters, such as segment inertia and mass, and the model itself, are completely blind to the controller. Differently from typical optimization approach, our method is to produce such optimization process without using cost function, purely with repetitive interactions with the given dynamic environment. The difference between the PD feedback case and synergetic learning case is only the last term of the command signal accumulation in Eq. 7.2. Neural integrators are found in many nervous system including our oculomotor system. This term corresponds to a neural integrator in the torque level.

7.5 Principles in Synergetic Learning Control

The difference from a typical FEL configuration is first the point where the motor-command error is created by the mapping between the task space force and the joint space

torque. In FEL, the optimized desired trajectory of position and velocity in joint space should be prepared in advance by optimizing some criteria specifically for the arm with redundant degrees of freedom [Schweighofer et al., 1998]. Here, the necessary joint position and velocity are unknown, and the task to follow the moving target is directly given keeping joint redundancy. Even if we use the Jacobian information, we do not perform inverse kinematic (IK) computation explicitly. The pseudo-inverse of Jacobian is not computed in this method differently from the typical methods in the robotics approach. Thus, the dimension reduction is not explicitly performed. The Jacobian itself can be obtained with the knowledge of the FK model. Thus, only FK information is assumed in this method, and the IK and ID models are unknown, here how to take the dynamics into account should be learned by the repetitive interactions with the environment. In the proposed method, the optimality can also be addressed by tacit learning with command signal accumulations to minimize the total energy consumption. Thus, along with the adaptivity originating from the FEL architecture, the optimal solution manageability can be a significant contribution of this method without using explicit model-based structure.

As for the mechanism on how motor performance can be optimized over time, the motor command accumulation part serves as an energy feedback with task space directional information. Simply, in general error feedback control, when the error is feedback, the error can be minimized. Similarly, the integrated torque command contains an energy measure since it accumulates the past torque generation history during cyclic reaching task. This term works as directional energy feedback, then naturally the energy of total system can be minimized as it is in a feedback loop. Thus, tacit learning can induce energy minimization through the repetitive actions with the environment while minimizing the endpoint error toward a given target point in the task space. This energy feedback architecture is formed in modular configuration. Even the torque accumulation feedback is performed in each individual joint, the total system receives the all energy consumption information from the associated joints. Then, the modified joint torque is feed to the coupled link dynamics and results in the new joint coordination as a total system.

In human motor control, the usage of feedforward control is well known, and it is a key to arrive at energetically efficient solution. Feedforward movements are made without sensory feedback, which have predictive nature of the given dynamics. Feedback control, in contrast, involves modification of the current movement using information from sensory receptors and error detection. If we rely on the feedback control and to perform certain accurate motion, local joint feedback gain tends to high resulting in a high joint stiffness, which is a source of increased energy consumption. The phase shift between feedback control and feedforward control during motor learning is well justified by obtaining the internal model in the cerebellum in previous papers [Kawato, 1999],[Kitazawa et al., 1998]. Optimal movement control likely reflects a combination of both feedback and feedforward processes [Desmurget and Grafton, 2000].

7.6 Control Results

7.6.1 Energy and Error Minimization

To evaluate the performance of the proposed synergetic learning control, we compare the control results of vertical tracking for 2D ellipsoidal trajectory between (a) PD feedback controller and (b) SyLC controller. The task of vertical reaching is to drive the endpoint of the arm following the dynamically moving target while holding a load at its hand under the gravity. The hand load was in two conditions, 450g and 600g respectively. The cycle frequency f to draw an ellipse is given with $1/T$, where T is the time to draw one ellipse.

The moving target $\boldsymbol{r}(t)$ is given as follows:

$$\begin{aligned} \boldsymbol{p}_c &= \begin{bmatrix} 0.0 & -0.4 \end{bmatrix}^T, \\ \boldsymbol{r}(t) &= \boldsymbol{p}_c + \begin{bmatrix} -0.15sin(2\pi ft) & -0.075cos(2\pi ft) \end{bmatrix}^T. \end{aligned} \tag{7.3}$$

At the beginning, the arm is stopped with extended posture to the gravity direction with zero joint angle for all the joints as in Fig.7.1(b).

Fig. 7.3(a) represents a control result for endpoint transition only with feedback control. The target was moving in ellipsoildal orbit in 1/4 Hz with 0.45kg load at hand. Fig. 7.3(b) is the endpoint with SyLC controller. The feedback control gains are kept same for the both type of controllers. The time sequential transition is illustrated using color map which changes depending on the time progress. A cool color map is used for (a) PD feedback control, a jet color map is used for (b) SyLC. This colormap configuration is used also in the other following figures.

Fig. 7.3(a) shows that PD control is largely affected by the gravity and the interaction torques. There is no learning effect then the endpoint loop is unchanged after the initial dynamic transition from the stopped straight arm configuration to the dynamic motion phase. On the contrary, we can find that the trajectory is being corrected in time in the case of synergetic learning control minimizing the effect of the gravity and interaction torque. Initially the trajectory was similar to the one of (a), but improves the tracking performance as indicated in Fig. 7.3 (c), which shows the transition of endpoint error. The average endpoint error is calculated as the root-mean-square (RMS) error between the target point and current endpoint during one cycle.

Energy consumption in one cycle of reaching was measured as an average power, which is plotted in Fig. 7.3 (d). The target is moved in ellipsoidal orbit in the frequency 1/4Hz. Therefore, the energy consumption during every 4 second was calculated by summing up each joint energy consumption $\tau\dot{\theta}$ and computed as a temporal work rate scale (power). The transition of energy consumption in learning control can be observed as in Fig. 7.3 (d). In Eq. 7.2, the torque component of PD feedback was regarded as feedback (FB) controller, the integration term was regarded as FF controller. The energy consumption by each torque component is also visualized as in Fig. 7.3 (d). The energy rate is not much changed in the course of learning, but we should note that the tracking error is being improved. Considering the fact that more energy is naturally necessary to make the motion with less error to the target. The synergetic

controller is managing dual conflicting criteria. One is to minimize the error, the other is to minimize the energy. Balance of these two criteria can be potentially manageable to adjust the learning gain and the feedback gain. However, we employed a fixed gain in this first robot trial to verify the feasibility of the proposed method in the real robot. In addition, it was possible to observe the contribution ratio was switched between FB and FF controllers. Initially FB was mainly used, and with learning progress, the energy consumption with FB is minimized, while FF contribution is significantly increased.

Next, motor control result to track the moving target in ellipsoildal orbit in 1/4 Hz with 0.6kg load at hand is summarized in Fig. 7.4. The hand weight is increased with 33 percent. The added moment of inertia in respect to the hand weight concerning the shoulder joint should have been increased with 33 percent. This test is to verify the control performance in different dynamic conditions. As the proposed method doen't use the prior plant dynamics information, the exactly same controller is rerun including the control gains and learning gain. We have only changed the weight from 450g to 600g in a real world.

We can observe in Fig. 7.4 (a)(b) that endpoint only with feedback control is affected more by larger inertial effect caused by the added hand weight, in contrast the endpoint in synergetic learning control is converged in similar way to the case of 450g toward tracking ellipsoidal target by compensating the gravity and the interaction torques. The synergetic control case converged to very close endpoint error which is only the difference of 3mm compared to the case of 450g as observed in Fig.7.4 (c). It successfully deals with the different dynamic condition. Keeping average endpoint error for different loads with exactly same controller is already not trivial in conventional robotics, when the joints of the arm have high compliance. The fact of high compliance of the manipulator can be confirmed from the feedback case performance of Fig. 7.4 (a). As the feedback gain is low, the arm is largely influenced by the environment, it indicates that the feedback gain which is employed in this experiment is low then the joint is highly compliant. The energy consumption in each ellipsoidal cycle of reaching as an average power was similar transition to the case of 450g, while increasing the absolute power scale corresponding to 600g hand weight as in Fig. 7.4 (d).

7.6.2 Synergetic Joint Usage

Fig. 7.5 indicates a phase portrait between the shoulder and the elbow joint angles in different dynamic conditions (a) 0.45kg, 1/4Hz, (b) 0.6kg, 1/4Hz, (c) 0.6kg, 1/3Hz, and both in only feedback control and in SyLC. The task trajectory itself was same, the difference were the hand load and the cycle speed.

The line in the cool color map indicates the joint usage result with only feedback control, and the line in the jet color map is that for synergetic learning. We see the phase in synergetic learning converges into the consistent joint angle combinations regardless of different dynamic conditions. In contrast, the joint space usage in only feedback control are different each other as it is significantly influenced by the inertial effect variation due to the motion speed and the hand load changes.

It is interesting to see the phase form is similar for different load conditions in synergetic learning. The phase portrait is a plot without time dimension, thus it can be an optimal joint synergetic usage regardless of the motion speed for a target trajectory under the given dyna-

mic environment. Then, the unchanged joint space usage is somehow reasonable. As the joint combination usage is common for different dynamic conditions, we can expect that it should be robust also for the case where the robot needs to change the motion speed or hand weight in the course of the motor control. Since it is necessary to change just slightly the joint usage space for dynamical condition changes, this situation helps a lot also for the adaptivity to the time-variant unknown environmental dynamics. If we carefully check Fig. 7.5, we can also find that the very initial phase portrait of learning case is very close to the one of feedback case as it is initially fully driven by feedback component of the controller. In the course of the learning, the similar synergetic combination between neighboring joints was found under different dynamic conditions. It is interesting to see such consistent and reasonable solution is gradually found even with the dynamics-model-free and cost-function-free approach.

TABLE 7.1: Endpoint RMS Error (m) and Energy Consumption (W) in each Cycle of Ellipsoidal Tracking Task

	PD Feedback Control			Synergetic Learning Control				
Time	Error	Energy	E-E index	Error	Energy	FF	FB	E-E index
				0.45kg				
8s	0.078	8.0	1.60	0.075 (0.0069)	7.91 (2.20)	0.385 (0.682)	7.78 (2.36)	1.69
16s	0.074	7.73	1.75	0.051 (0.0025)	9.40 (1.01)	2.04 (0.974)	8.41 (0.30)	2.09
32s	0.075	8.05	1.66	0.039 (0.0015)	10.7 (0.16)	5.44 (0.614)	7.36 (0.707)	2.40
64s	0.073	8.0	1.71	0.032 (0.00052)	10.98 (0.30)	8.98 (0.335)	6.26 (0.20)	2.85
120s	0.073	8.05	1.70	0.032 (0.00064)	10.81 (0.28)	10.05 (0.108)	5.95 (0.166)	2.89
200s	-	-	-	0.029 (0.00021)	11.02 (0.07)	10.16 (0.13)	5.77 (0.091)	3.13
				0.6kg				
8s	0.087	9.73	1.18	0.084 (0.0147)	10.1 (4.10)	0.417 (0.896)	9.94 (4.20)	1.18
16s	0.086	9.73	1.20	0.065 (0.0087)	12.6 (0.90)	2.65(1.22)	10.5 (0.975)	1.22
32s	0.085	9.85	1.19	0.042 (0.0041)	12.3 (0.21)	6.21 (0.724)	8.06 (0.465)	1.94
64s	0.086	9.81	1.19	0.034 (0.00034)	12.3 (0.24)	9.54 (0.307)	6.44 (0.05)	2.39
120s	0.085	9.73	1.21	0.033 (0.00055)	12.5 (0.10)	11.1 (0.050)	6.18 (0.231)	2.42
200s	-	-	-	0.032 (0.00025)	12.4 (0.14)	11.4 (0.25)	6.10 (0.045)	2.52

*The figures in parentheses indicate the cycle-to-cycle variability to evaluate the convergence of synergetic learning control. Between PD feedback and synergetic learning control, the same gain k of the task space propotional feedback is used as well as local joint PD gains.

7.6.3 Error-Energy index

As it is previously stated, human motor control employs multiple criteria. If it is industrial robot, only thinking about the endpoint accuracy may be enough. However, human motor control takes into account also the energy efficiency [Izawa et al., 2008]. Thus, if we look into only the endpoint accuracy of human motor control, it is not necessarily with high precision. For instance, the casual hand move from right to left in front of your body is not that straight, a little curved around the shoulder with the compromised choice of motor command which is easily taken from the given body dynamics. In vice-versa, if we evaluate only the energy criteria ignoring motion accuracy, the choice of no motion can be best. However, we still want the subject or the robot to perform the specific task. Then, we propose here the simplest criterion to evaluate the both of error and energy for a reaching task. We name it as E-E index, which is simply 1/Error/Energy. 1/Error means the accuracy of the tracking, then 1/Error/Energy represents normalized accuracy per unit energy. Here, we have used power (W) as a unit energy.

Then 1/Error/Energy represents normalized accuracy per power. It can represent the motion accuracy rate produced with the unit energy. We have introduced this E-E index to evaluate the motor control performance in reaching with dual criteria of error and energy. As the proposed controller is not with optimization process, this index itself is not used during the control process, it was used only for a posterior evaluation of the performance generated by the learning controller.

The endpoint error and the energy consumption transition along with the time progress is summarized in Table 7.1 for two hand load conditions. In PD feedback control, there is no improvement for both error and energy. The variation in the initial phase is due to the fact that the robot changes from stopped status (with extended posture to the gravity direction with zero joint torque) to the dynamic motion status. This effect can be seen also in the initial phase of SyLC. Differently from simulation, the real robot has some frictions in the joint, then some minor value fluctuation can be also observed after the steady-state status.

We can notice that the energy consumption in SyLC is not being minimized, however the endpoint error is minimized to improve the target tracking accuracy during learning control while keeping the energy consumption. The energy consumption ratio by FF controller is being augmented while the one of FB controller is being decreased. The figures in parentheses in Table 7.1 indicate the cycle-to-cycle variability to evaluate the convergence of tacit learning. We can confirm that the error, the energy and the contributions of FF and FB are all converged in the course of the learning process in SyLC.

To take into account the Error-Energy balance, the above mentioned E-E index is computed as in the right column of Table 7.1. In this index, we can observe the clear advantage of SyLC over sole feedback control. From 16s, all the E-E indexes are larger than the case of feedback control, it went into nearly 3. E-E index represents the motion accuracy rate produced with the unit energy. Then, it can measure the motion accuracy in the cost of the energy consumption. In the case of 0.6kg, E-E index was converged even into double of the one in sole feedback control.

7.6.4 Adaptivity for different motion speed

At last, we demonstrate the adaptive nature of the synergetic learning controller. Differently from the previous tests, we changed the moving target speed suddenly in the course of the robot control.

Fig. 7.6 shows the motor control result with 0.6kg load at hand, with task speed changes in the order of 1/4Hz, 1/3Hz and 1/2.5Hz. The change is made in a step manner. Simply, the f in Eq. 7.3 is modified at a time instant. Fig. 7.6 (a) is endpoint transition with synergetic learning control. From (a), we can confirm that synergetic learning control manages well to track moving target even when the target moves suddenly faster. The slight endpoint trajectory change can be observed. Fig. 7.6 (b) plots elbow joint angle-angular velocity phase portrait, different elbow angular velocity realization can be confirmed by keeping the same elbow joint angle space. Fig. 7.6 (c) is the transition of endpoint error, we observe slight end-point error changes with 2.8mm increase from 1/4Hz to 1/3Hz, with 2.9mm increase from 1/3Hz to 1/2.5Hz. Especially in 1/2.5Hz, the robot has to manage to follow in a fast speed for an ellipsoid in average speed of 144deg/s while holding 0.6kg weight. In Fig. 7.6 (d), energy consumption rate can be confirmed. It increases steadily according to the increased motion speed. The contribution

ratio between FB and FF controllers is maintained to follow a moving target in higher speed. Thanks to this nature, motor commands are quickly found for new dynamic condition. It is demonstrating adaptivity nature of the synergetic learning controller.

7.7 Discussion

We have applied a bioinspired motor learning control paradigm to the control of redundant manipulators in a real world. First, it is challenging to manage both adaptability and optimality without using model-based approaches and without prior knowledge of the given dynamics. In fact, the current robotics approach has a separated configuration on motor control and learning. This article demonstrated a way to bridge the gap between learning and control. Synergetic Learning Control (SyLC) is firstly published to systematically induce the motor synergy emergence in reaching task [Hayashibe and Shimoda, 2014]. Please refer to this article for the further information in the case of other reaching task. There, vertical point-to-point reaching task is investigated with Open Dynamics Engine platform. The multidirectional reaching is also performed. The basic control nature of this method was common between the simulation result and the real world robot. However, we could observe some differences as well. First, in a real robot, even if it has backdrivability, there is a joint friction and the internal gear inertia. In contrast, there is completely no joint friction and gear inertia in simulation. After the learning, FB component ratio against the total energy consumption was less than 20 percent in simulation. However, FB component ratio in the real robot is stayed still around 50 percent against total energy as we can see it in at the right bottom of Fig. 7.3,7.4,7.6. Of course, it is advantageous if the dependency on FB could be further decreased in terms of energy minimization, but we believe that the geared joint inertia and friction covered the environmental dynamics information for the learning process. Thus, the unknown gear dynamics in the robot had to be dealt with FB component.

Motor learning is a process which develops Feed Forward (FF) controller minimizing the contributions from Feedback controller. The torque integration term in tacit learning can be considered as FF controller which anticipates the environmental interactions during reaching. During the learning, the contribution from FF was increased and the torque from FF was converged into certain pattern. This effect matches well the neurological learning process. We could have this human-like learning phenomenon in real redundant robot control with the proposed synergetic learning control scheme. The obtained result also gives us an insight to understand the human motor control, and the FB and FF component can not be measured in human, but the role of them in relationship to energy efficiency could be quantified from the robot experiment as in the table 7.1.

To evaluate the control performance in the dual criteria: endpoint error minimization and energy consumption, we have introduced a new index: Error-Energy index which can measure the motion accuracy rate in the cost of unit energy. We have introduced this new index just for evaluation after learning control. However, it could be a useful cost function also in the conventional model-based optimization. Previous popular cost function is considering the torque changes or energy consumption without being coupled with the corresponding motion accuracy. However, if we look into actual human control which is not necessarily accurate depending

on the subject engagement, these conflicting criteria is quite a coupled issue. Evaluating the motion accuracy rate in the cost of unit energy with the proposed E-E index in human reaching study should be also an interesting topic.

The vertical reaching task under the gravity involves much complex interaction torques. When the conflicting torques between coupled joint dynamics could be minimized, it can result in energy effective motion. To reduce the conflicts, naturally joints should be synergetically used. The joint angle acceleration in the shoulder involves all the arm segments from upper arm, forearm to the hand. The elbow is nice to be synchronously drived then the forearm is well accelerated by the shoulder. The component of forearm acceleration to be made by the elbow, will be naturally minimized. This phenomenon is well observed in Fig. 7.5. The shoulder-elbow phase portrait turned into similar circular form for different dynamic task conditions in synergetic learning. As the joint combination usage is common for different dynamic conditions, we can expect that it should be robust also for the case where the robot needs to change the motion speed or hand weight in the course of the motor control. Indeed, our method demonstrated the great adaptive nature for the different task speed condition as in Fig.7.6. As it is similar task except the motion speed, the robot already knows the effective synergetic joint usage for the given task then the necessary motor commands are quickly found almost without the learning process for a new dynamic condition. Please note that the robot is holding 600g weight, which induces certain amount of inertia. The endpoint accuracy is degraded only slightly. It is demonstrating adaptivity nature of the synergetic learning controller along with Error-Energy optimality.

7.8 Conclusion

In this chapter, we have verified a novel computational control paradigm named Synergetic Learning Control in redundant manipulator. From the control result, we claim that the proposed method is valid for acquiring synergetic motor usage in the system with actuation redundancy. We should highlight that the SyLC brings computational adaptability and optimality with dynamic model-free and cost-function-free approach differently from previous studies. Energy efficient solutions could be obtained by the emergence of motor synergy in the redundant actuation space.

Increasing the contribution of FF controller which corresponds to so-called internal model development also matches well the nature of computational motor learning in human being as an infant can improve his motor control ability by repetitions without thinking of something complex. The result demonstrated in this paper is also concerning to the Bernstein's DOF problem. Bernstein problem is an issue regarding how Central Nervous System (CNS) finds the optimal solution in the actuation redundancy. The usage of motor synergy was pointed out by Bernstein, but a fundamental motor control principal which can generate motor synergy has not yet been reported in neuroscience except so-called optimization approach. The proposed SyLC paradigm firstly managed to generate dual aspects of adaptivity and optimality by a modular computational principle for redundant robot, which should be also beneficial for future neuroprosthetic control.

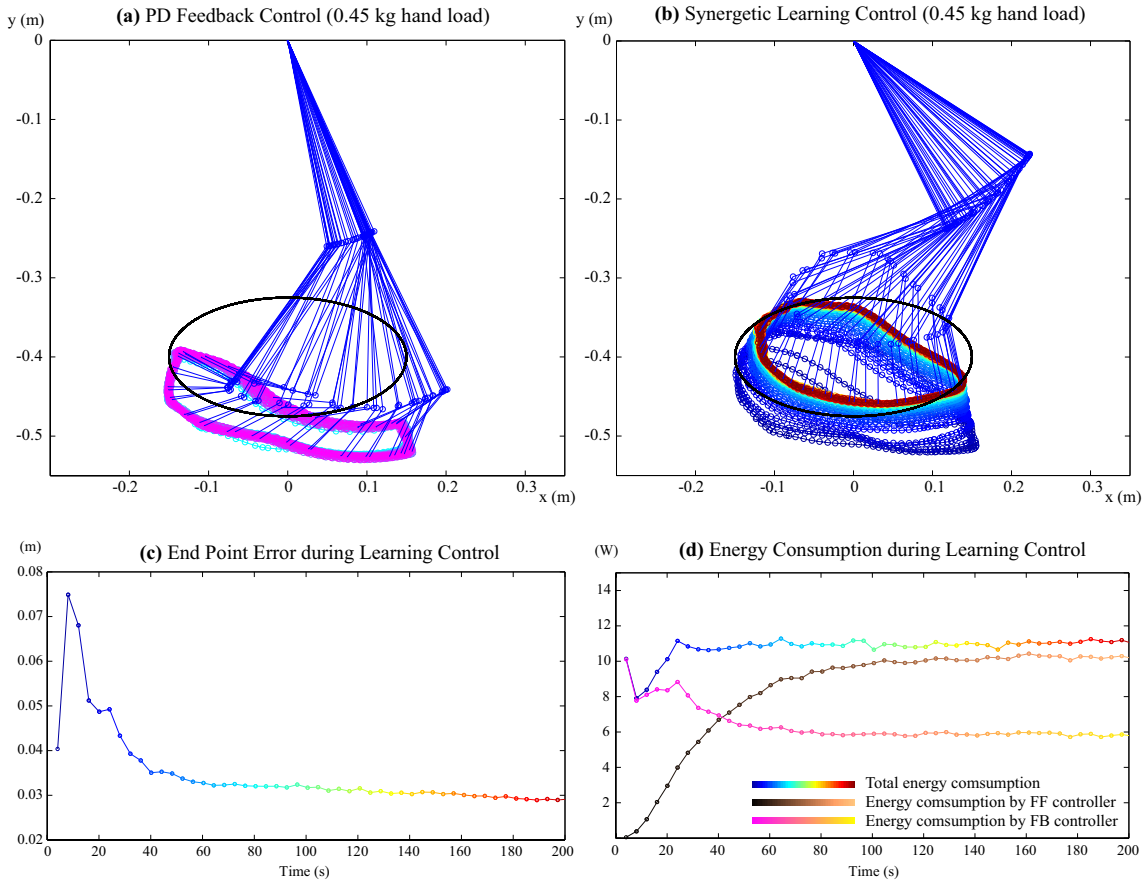

FIGURE 7.3: Motor control result to track the moving target in ellipsoildal orbit in 1/4 Hz (0.45kg load at hand). (a) Endpoint transition only with feedback control and (b) with synergetic learning control. (c) The transition of endpoint error and (d) the energy consumption in each ellipsoidal cycle of reaching as an average power. Not only improving the target tracking accuracy, but synergetic learning solutions result in efficient total energy consumption in respect to the tracking accuracy. In addition, it was possible to observe the contribution ratio was switched between FB and FF controllers. Initially FB was mainly used, and with learning progress, the energy consumption with FB is minimized, while FF contribution is increased.

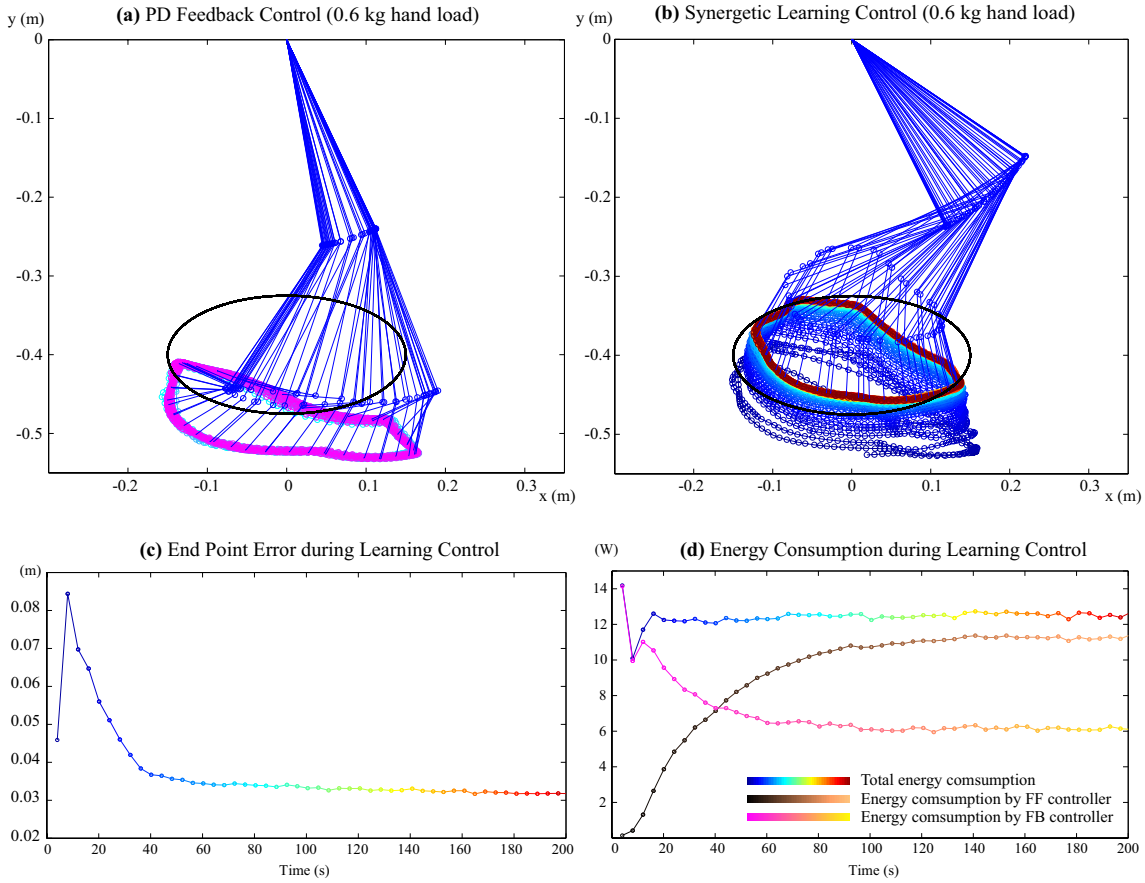

FIGURE 7.4: Motor control result to track the moving target in ellipsoidal orbit in 1/4 Hz (0.6kg load at hand). (a) Endpoint transition only with feedback control and (b) with synergetic learning control. (c) The transition of endpoint error and (d) the energy consumption in each ellipsoidal cycle of reaching as an average power. By added load, larger tracking error is observed in feedback control case caused by larger inertial effect in this dynamic motion. In contrast, synergetic control converged to endpoint error which is only the difference of 3mm compared to the case of 450g. It successfully deals with the different dynamic condition.

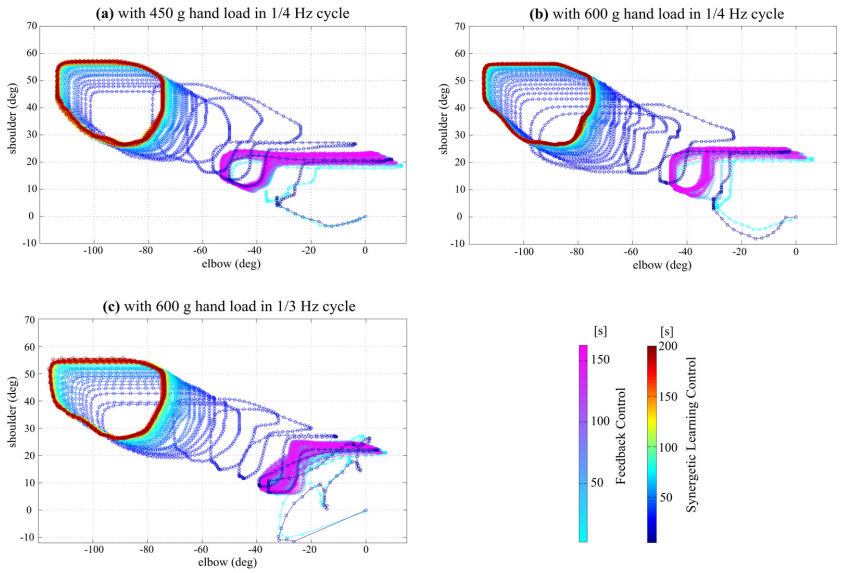

FIGURE 7.5: Phase portrait between the shoulder and the elbow joint angle in different dynamic conditions (a) 0.45kg,1/4Hz, (b) 0.6kg,1/4Hz, (c) 0.6kg,1/3Hz, and both in only feedback and in synergetic learning control. The line in the cool color map indicates the joint usage result with only feedback control, and the line in the jet color map is that for synergetic learning. We see the phase in synergetic learning converges into the consistent joint angle combination space regardless of different dynamic conditions. In contrast, the joint space usage in only feedback control are different each other as it is significantly influenced by the inertial effect variation.

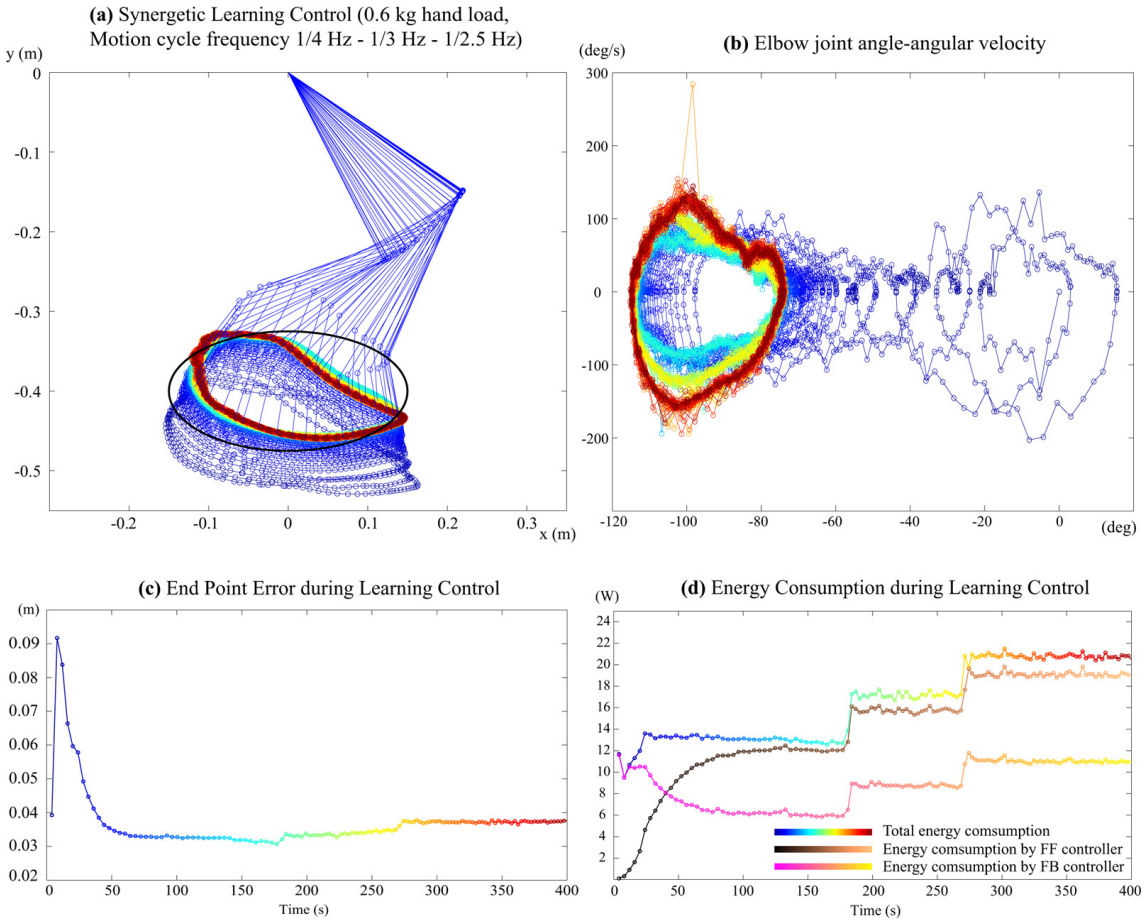

FIGURE 7.6: Motor control result to track the moving target in ellipsoidal orbit with 0.6kg load at hand, with task speed changes in the order of 1/4Hz, 1/3Hz and 1/2.5Hz. (a) Endpoint transition with synergetic learning control and (b) Elbow joint angle-angular velocity phase portrait. (c) The transition of endpoint error and (d) the energy consumption in each ellipsoidal cycle of reaching as an average power. From (a), we can confirm that synergetic learning control manages well to track moving target with slight end-point error changes seen in (c). Especially in 1/2.5Hz, the robot has to manage to follow in a fast speed for an ellipsoid in average speed of 144deg/s while holding 0.6kg weight. From (b), different elbow angular velocity realization can be confirmed. In (d), the contribution ratio between FB and FF controllers is maintained for higher speed tracking. Thanks to this nature, motor commands are quickly found for new dynamic condition.

CHAPTER 8

Conclusion and Perspective

FES and Neuroprosthetics are one of existing rehabilitation techniques to restore lost motor functions for motor-impaired subjects. The stimulator generates electrical pulses to drive artificial contractions of the paralysed muscles, through activating intact motor units. Nowadays, FES-based rehabilitation solutions have been investigated in laboratory environments to help the paralyzed patients to evoke their motor abilities. FES can be employed to assist kinds of specific movements, such as balance support, locomotion, grasping/holding/releasing, or drop foot correction. Besides, it can also be beneficial to muscle capability training, such as reducing muscle atrophy, preventing muscle spasms, and facilitating muscle rehabilitation. However, many limitations still remain when transferring current FES systems which are developed in laboratories to realistic clinical environments, due to the subject-specific and inaccurately-predicted performances. The time-varying muscle fatigue and subject-specific properties complicate the prediction of torque variations with fatigue and the subsequent control of joint torque. To resolve these problems, this HDR thesis mainly contributed regarding personalized modeling on evoked muscle response, and its usage for personalized neuroprosthetic muscle control. Toward real-time online implementation of closed-loop FES systems, the developped algorithm is embedded together with wireless portable stimulator. The results in this HDR thesis show its promising performance with experiment performed with SCIs. I continue the work toward further computational development to contribute neuroprosthetic domain.

In parallel to this direction, I continue to work on other modeling and motor learning control activities. One important work is muscle modeling. Hill muscle model is a still standard for long time, it works reasonable for wide areas. However, there exists researcher who points out its limitations especially when it is used for different physiological conditions. One direction is going for more physiologically reliable muscle modeling as Hill model is a phenomenological model. The other is for more dimensionally detailed modeling as Hill model is a wire model. There is an important work going on regarding volumetric muscle model.

- Y. Berranen, M. Hayashibe, D. Guiraud, B. Gilles, Real-time Muscle Deformation via Decoupled Modeling of Solid and Muscle Fiber Mechanics", Medical Image Computing and Computer-Assisted Intervention -MICCAI2014, Lecture Notes in Computer Science, Vol. 8674, pp.65-72, 2014.
  `http://www.lirmm.fr/~hayashibe/Miccai2014/miccaiSohusim.avi`

This work presents a novel approach for simulating 3D muscle deformations with complex architectures. The approach consists in choosing the best model formulation in terms of computation cost and accuracy, that mixes a volumetric tissue model based on finite element method (3D FEM), a muscle fiber model (Hill contractile 1D element) and a membrane model accounting for aponeurosis tissue (2D FEM). The separate models are mechanically binded using barycentric embeddings. Our approach allows the computation of several fiber directions in one coarse finite element, and thus, strongly decreases the required finite element resolution to predict muscle deformation during contraction. Using surface registration, fibers tracks of specific architecture can be transferred from a template to subject morphology, and then si-

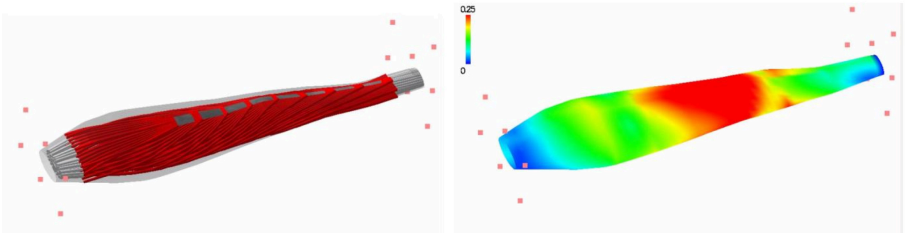

FIGURE 8.1: Left: Hybrid volumetric muscle model of bipennate fiber architecture, right: internal stress during isometric contraction.

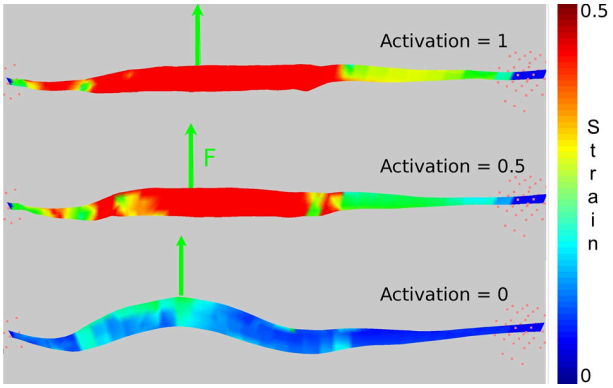

FIGURE 8.2: Rectus femoris deformations during pulling in the transversal direction of the line of muscle force action, for activation levels of respectively 0, 0.5 and 1. Color bar shows the maximum principal strain on a sagittal plane inside the muscle. The stiffness in transversal direction increased according to muscle contraction.

mulated. As a case study, three different fiber architectures sharing same volumetric space are simulated and compared to their equivalent one-dimensional Hill wire models. We continue to improve both physiologically detailed muscle modeling while challenging purely computationally advanced technical development toward fast multiple volumetric muscle modeling.

Regarding personalized whole-body center of mass adaptive identification, it allows to determine a personalized measurement of human balance that is adapted to low-cost sensors and that can be used in the home environment for a wide range of motions. This method could be used by therapist to evaluate a patients progress during a physical reha- bilitation program, or be used by the patient to receive visual feedback while performing rehabilitation exercises during self- guided exercise sessions at home. The developed software PersoBalance is registered at the french Agence de Protection des Programmes (APP). The collaborative work is being scheduled, one is with French startup company NaturalPad to embed our new personalized balance measure in their rehabilitative video game they developped for general motor training in hospitals and homes. The other is under INRIA equipe-associe program NeuroPhys4NeuroRehab"(PI: Anirban Dutta). This project seeks development of neurophysiological test setup for customizing and monitoring patient-specific non-invasive electrical stimulation-facilitated neurorehabilitation. PersoBalance will be integrated with their system

to study specifically visiomotor functions in relation to postural stability in post-stroke subjects.

At last, synergetic learning control paradigm in collaboration with RIKEN Brain Science Institute is also important activity to reveal the fundamental learning/control mechanisms which is embedded in central nervous system. Understanding the genuine learning control mechanism is quite meaningful to develop enhanced rehabilitation paradigms for spinal cord injured patients and post-stroke subjects. The rehabilitation is indeed re-learning process under the given constraints. I expect to apply this control paradigm for enhanced neuroprosthetics by being aware of motor learning nature in the long-term perspective.

List of Acronyms

ARX	Autoregressive with External Input
ASIA	American Spinal Injury Association
EFPC	EMG-Feedback Predictive Control
CNS	Central Nervous System
EMG	Electromyography
eEMG	evoked Electromyography
FES	Functional Electrical Stimulation
GPC	Generalized Predictive Control
GM	Gastrocnemius
KF	Kalman Filter
LS	Least Squares
MUAP	Motor Unit Action Potential
MAV	Mean Absolute Value
MDF	Median Frequency
MDL	Rissanen's Minimum Description Length
NGPC	Nonlinear Generalized Predictive Control
NRMS	Normalized Root Mean Squares
NPE	Normalized Peak Error
OLS	Ordinary Least Squares
PNS	Peripheral Nervous System
PW	Pulse Width
PHM	Polynomial Hammerstein Model
RF	Radio Frequency
RMS	Root Mean Squares
SCI	Spinal Cord Injury
SNR	Signal to Noise Ratio
TA	Tibialis Anterior

BIBLIOGRAPHY

[Aboy et al., 2005] Aboy, M., Marquez O. W., McNames, J., Hornero, R., Trong T., and Goldstein, B. (2005). Adaptive modeling and spectral estimation of nonstationary biomedical signals based on Kalman filtering. *IEEE Transactions on Biomedical Engineering*, 52:1485–1489.

[Ajoudani and Erfanian, 2009] Ajoudani, A. and Erfanian, A. (2009). A Neuro-Sliding-Mode Control With Adaptive Modeling of Uncertainty for Control of Movement in Paralyzed Limbs Using Functional Electrical Stimulation. *IEEE Transactions on Biomedical Engineering*, 56(7):1771–1780.

[Alexander, 1997] Alexander, R. M. (1997). A minimum energy cost hypothesis for human arm trajectories. *Biological Cybernetics*, 76(2):97–105.

[Arimoto and Sekimoto, 2006] Arimoto, S. and Sekimoto, M. (2006). Human-like movements of robotic arms with redundant DOFs: virtual spring-damper hypothesis to tackle the Bernstein problem. *Proceedings 2006 IEEE International Conference on Robotics and Automation, 2006. ICRA 2006.*, (May):1860–1866.

[Ayusawa et al., 2013] Ayusawa, K., Venture, G., and Nakamura, Y. (2013). Identifiability and Identification of Inertial Parameters Using the Underactuated Base-Link Dynamics for Legged Multibody Systems. *The International Journal of Robotics Research*, 33(3):446–468.

[Bastian et al., 1996] Bastian, A. J., Martin, T. A., Keating, J. G., and Thach, W. T. (1996). Cerebellar ataxia: abnormal control of interaction torques across multiple joints. *Journal of Neurophysiology*, 76(1):492–509.

[Bernotas et al., 1986] Bernotas, L. A., Crago, P. E., and Chizeck, H. J. (1986). A discrete-time model of electrically stimulated muscle. *IEEE Transactions on Biomedical Engineering*, BME-33:829–838.

[Bernstein, 1967] Bernstein, N. (1967). *The Co-ordination and Regulation of Movements*. Pergamon Press, Oxford, UK.

[Bestel and Sorine, 2000] Bestel, J. and Sorine, M. (2000). A differential model of muscle contraction and applications. In *Schloessmann Seminar on Mathematical Models in Biology, Chemistry and Physics, Max Plank Society*, Bad Lausick, Germany.

[Binder-Macleod and Snyder-Mackler, 1993] Binder-Macleod, S. and Snyder-Mackler, L. (1993). Muscle fatigue: clinical implications for fatigue assessment and neuromuscular electrical stimulation. *Physical Therapy*, 73(12):902–910.

[Bizzi et al., 1991] Bizzi, E., Mussa-Ivaldi, F. A., and Giszter, S. (1991). Computations underlying the execution of movement: a biological perspective. *Science*, 253(5017):287–291.

[Borton et al., 2013] Borton, D., Micera, S., Millán, J. d. R., and Courtine, G. (2013). Personalized neuroprosthetics. *Science translational medicine*, 5(210):210rv2—-210rv2.

[Braun et al., 2009] Braun, D., Aertsen, A., Wolpert, D. M., and Mehring, C. (2009). Learning optimal adaptation strategies in unpredictable motor tasks. *The Journal of neuroscience : the official journal of the Society for Neuroscience*, 29(20):6472–8.

[Breen et al., 2006] Breen, P., O'Keeffe, D., Conway, R., and Lyons, G. M. (2006). A system for the delivery of programmable, adaptive stimulation intensity envelopes for drop foot correction applications. *Medical Engineering and Physics*, 28:177–186.

[Cai et al., 2010] Cai, Z. J., Bai, E.-w., and Shields, R. K. (2010). Fatigue and non-fatigue mathematical muscle models during functional electrical stimulation of paralyzed muscle. *Biomedical Signal Processing and Control*, 5:87–93.

[Camacho and Bordons, 1999] Camacho, E. F. and Bordons, C. (1999). *Model Predictive Control*. Springer.

[Chen and Yu, 1997] Chen, J. J. and Yu, N. Y. (1997). The validity of stimulus-evoked EMG for studying muscle fatigue characteristics of paraplegic subjects during dynamic cycling movement. *IEEE Transactions on Rehabilitation Engineering*, 5(2):170–178.

[Chen et al., 2001] Chen, Y. L., Li, Y. C., Kuo, T. S., and Lai, J. S. (2001). The development of a closed-loop controlled functional electrical stimulation (FES) in gait training. *Journal of Medical Engineering Technology*, 25(2):41–48.

[Chesler and Durfee, 1997] Chesler, N. C. and Durfee, W. K. (1997). Surface EMG as a fatigue indicator during FES-induced isometric muscle contractions. *Journal of Electromyography and Kinesiology*, 7(1):27–37.

[Chia et al., 1991] Chia, T. L., Chow, P. C., and Chizeck, H. J. (1991). Recursive parameters identification of constrained systems: an appliction to electrically stimulated muscle. *IEEE Transactions on Biomedical Engineering*, 38:429–442.

[Cifrek et al., 2009] Cifrek, M., Medved, V., Tonkovic, S., and Ostojic, S. (2009). Surface EMG based muscle fatigue evaluation in biomechanics. *Clinical Biomechanics*, 24:327–340.

[Clancy et al., 2012] Clancy, E. A., Liu, L., Liu, P., and Moyer, D. V. Z. (2012). Identification of Constant-Posture EMG-Torque Relationship About the Elbow Using Nonlinear Dynamic Models. *Biomedical Engineering, IEEE Transactions on*, 59(1):205–212.

[Cotton et al., 2009] Cotton, S., Murray, A. P., and Fraisse, P. (2009). Estimation of the Center of Mass: From Humanoid Robots to Human Beings. *IEEE/ASME Transactions on Mechatronics*, 14(6):707–712.

[Cotton et al., 2011] Cotton, S., Vanoncini, M., Fraisse, P., Ramdani, N., Demircan, E., Murray, A. P., and Keller, T. (2011). Estimation of the centre of mass from motion capture and force plate recordings : a study on the elderly. *Applied Bionics and Biomechanics*, 8(1):67–84.

[Courtine et al., 2009] Courtine, G., Gerasimenko, Y., van den Brand, R., Yew, A., Musienko, P., Zhong, H., Song, B., Ao, Y., Ichiyama, R. M., Lavrov, I., Roy, R. R., Sofroniew, M. V., and

Edgerton, V. R. (2009). Transformation of nonfunctional spinal circuits into functional states after the loss of brain input. *Nature neuroscience*, 12:1333–1342.

[Czerwosz et al., 2009] Czerwosz, L., Blaszczyk, J., Mraz, M., and Curzytek, M. (2009). Application of virtual reality in postural stability rehabilitation. In *In Proc. of the Virtual Rehabilitation International Conference*, page 214, Haifa, Israel.

[D'Avella et al., 2003] D'Avella, A., Saltiel, P., and Bizzi, E. (2003). Combinations of muscle synergies in the construction of a natural motor behavior. *Nat Neurosci*, 6(3):300.

[de Leva, 1996] de Leva, P. (1996). Adjustments to Zatsiorsky-Seluyanov's segment inertia parameters. *Journal of Biomechanics*, 29(9):1223–1230.

[Dempsey and Westwick, 2004] Dempsey, E. J. and Westwick, D. T. (2004). Identification of Hammerstein Models With Cubic Spline Nonlinearities. *IEEE Transactions on Biomedical Engineering*, 51:237–245.

[Desmurget and Grafton, 2000] Desmurget, M. and Grafton, S. (2000). Forward modeling allows feedback control for fast reaching movements. *Trends Cogn Sci*, 4(11):423–431.

[Deutsch et al., 2009] Deutsch, J. E., Robbins, D., Morrison, J., and Guarrera Bowlby, P. (2009). Wii-based compared to standard of care balance and mobility rehabilitation for two individuals post-stroke. In *In Proc. of the International Conference on Virtual Rehabilitation*, pages 117–120, Haifa, Israel.

[Donaldson et al., 1997] Donaldson, N. D., Perkins, T. A., and Worley, A. C. (1997). Lumbar root stimulation for restoring leg function: stimulator and measurement of muscle actions. *Artificial organs*, 21(3):247–249.

[Dowling et al., 2014] Dowling, A. V., Barzilay, O., Lombrozo, Y., and Wolf, A. (2014). An Adaptive Home-Use Robotic Rehabilitation System for the Upper Body. *IEEE Journal of Translational Engineering in Health and Medicine*, 2:1–10.

[Durfee, 1993] Durfee, W. K. (1993). Control of standing and gait using electrical stimulation: influence of muscle model complexity on control strategy. *Progress in brain research*, 97:369–381.

[Durfee and MacLean, 1989] Durfee, W. K. and MacLean, K. E. (1989). Methods for estimating isometric recruitment curves of electrically stimulated muscle. *IEEE transactions on biomedical engineering*, 36(7):654–667.

[Dutta et al., 2008] Dutta, A., Kobetic, R., and Triolo, R. J. (2008). Ambulation After Incomplete Spinal Cord Injury With EMG-Triggered Functional Electrical Stimulation. *IEEE Transactions on Biomedical Engineering*, 55(2):791–794.

[Edwards, 1981] Edwards, R. H. (1981). Human muscle function and fatigue. *Ciba Foundation symposium*, 82:1–18.

[El Makssoud, 2005] El Makssoud, H. (2005). *Modelisation et identification des muscles squelettiques sous stimulation electrique fonctionnelle*. PhD thesis, University of Montpellier II.

[El Makssoud et al., 2011] El Makssoud, H., Guiraud, D., Poignet, P., Hayashibe, M., Wieber, P. B., Yoshida, K., and Azevedo-Coste, C. (2011). Multiscale modeling of skeletal muscle properties and experimental validations in isometric conditions. *Biological Cybernetics*, 105(2):121–138.

[Erbatur et al., 2009] Erbatur, K., Koca, O., Taskiran, E., Yilmaz, M., and Seven, U. (2009). ZMP Based Reference Generation for Biped Walking Robots. *World Academy of Science, Engineering and Technology*, 3(10):929–936.

[Erfanian et al., 1994] Erfanian, A., Chizeck, H. J., and Hashemi, R. M. (1994). A characterization of changes in the dynamics of muscle contraction during prolonged electrical stimulation. *Proceedings of the 16th Annual International Conference of the IEEE Engineering in Medicine and Biology Society (EMBC94), Baltimore, MD*, pages 343–344.

[Erfanian et al., 1996] Erfanian, A., Chizeck, H. J., and Hashemi, R. M. (1996). Excitation-contraction fatigue during sustained electrical stimulation of paralyzed muscle. *Proceedings of the 18th Annual International Conference of the IEEE Engineering in Medicine and Biology Society (EMBC96), Amsterdam, Netherlands*, 4:1460–1461.

[Erfanian et al., 1998] Erfanian, A., Chizeck, H. J., and Hashemi, R. M. (1998). Using evoked EMG as a synthetic force sensor of isometric electrically stimulated muscle. *IEEE Transactions on Biomedical Engineering*, 45(2):188–202.

[Farahat and Herr, 2005] Farahat, W. and Herr, H. (2005). A Method for Identification of Electrically Stimulated Muscle. In *Proceedings of the 27th Annual Conference of the IEEE Engineering in Medicine and Biology Society (EMBC05), Shanghai, China*.

[Farina and Roberto, 2000] Farina, D. and Roberto, M. (2000). Comparison of algorithms for estimation of EMG variables during voluntary isometric contractions. *Journal of Electromyography and Kinesiology*, 10(5):337–349.

[Farnsworth et al., 2008] Farnsworth, B. D., Triolo, R. J., and Young, D. J. (2008). Wireless Implantable EMG Sensing Microsystem. *Proceedings of the 7th IEEE Conference on Sensors, Lecce, Italy*, pages 1245–1248.

[Ferrarin et al., 2001] Ferrarin, M., Palazzo, F., Riener, R., and Quintern, J. (2001). Model-based control of FES induced single joint movements. *IEEE Transactions on Neural Systems and Rehabilitation Engineering*, 9(3):245–257.

[Floor-Westerdijk et al., 2012] Floor-Westerdijk, M. J., Schepers, H. M., Veltink, P. H., van Asseldonk, E. H. F., and Buurke, J. H. (2012). Use of Inertial Sensors for Ambulatory Assessment of Center of Mass Displacements During Walking. *IEEE Transactions on Biomedical Engineering*, 59(7):2080–2084.

[Frigo et al., 2000] Frigo, C., Ferrarin, M., Frasson, W., Pavan, E., and Thorsen, R. (2000). EMG signals detection and processing for on-line control of functional electrical stimulation. *Journal of Electromyography and Kinesiology*, 10(5):351–360.

[Fujita et al., 2005] Fujita, T., Nakamura, S., Ohue, M., Fujii, Y., Miyauchi, A., Takagi, Y., and Tsugeno, H. (2005). Effect of age on body sway assessed by computerized posturography. *Journal of Bone and Mineral Metabolism*, 23(2):152–156.

[Fung and Perez, 2011] Fung, J. and Perez, C. F. (2011). Sensorimotor enhancement with a mixed reality system for balance and mobility rehabilitation. In *In Proc. of the Annual International Conference IEEE Engineering in Medicine and Biology Society (IEEE/EMBC)*, volume 2011, pages 6753–6757, Boston, MA, USA.

[Gandevia et al., 1995] Gandevia, S., Enoka, R. M., McComas, A. J., Stuart, D. G., and Thomas, C. K., editors (1995). *Fatigue: neural and muscular mechanisms*. Plenum press, NY.

[Giuffrida and Crago, 2005] Giuffrida, J. P. and Crago, P. E. (2005). Functional restoration of elbow extension after spinal-cord injury using a neural network-based synergistic FES controller. *Neural Systems and Rehabilitation Engineering, IEEE Transactions on*, 13(2):147–152.

[González et al., 2014] González, A., Hayashibe, M., Bonnet, V., and Fraisse, P. (2014). Whole Body Center of Mass Estimation with Portable Sensors: Using the Statically Equivalent Serial Chain and a Kinect. *Sensors*, 14(9):16955–16971.

[González et al., 2012] González, A., Hayashibe, M., and Fraisse, P. (2012). Estimation of the Center of Mass with Kinect and Wii balance board. In *In Proc. of the IEEE/RSJ International Conference on Intelligent Robots and Systems (IROS)*, pages 1023–1028, Vilamoura, Alagarve, Portugal.

[Goswami, 1999] Goswami, A. (1999). Postural Stability of Biped Robots and the Foot-Rotation Indicator (FRI) Point. *The International Journal of Robotics Research*, 18(6):523–533.

[Goswami and Kallem, 2004] Goswami, A. and Kallem, V. (2004). Rate of Change of Angular Momentum and Balance Maintenance of Biped Robots. In *In Proc. of the IEEE International Conference on Robotics and Automation (ICRA)*, pages 3785–3790, New Orleans, LA, USA.

[Guigon et al., 2007] Guigon, E., Baraduc, P., and Desmurget, M. (2007). Computational motor control: redundancy and invariance. *Journal of neurophysiology*, 97(1):331–47.

[Guiraud et al., 2006] Guiraud, D., Stieglitz, T., Koch, K. P., Divoux, J.-L., and Rabischong, P. (2006). An implantable neuroprosthesis for standing and walking in paraplegia: 5-year patient follow-up.

[Hamada et al., 2004] Hamada, T., Kimura Tetsuya, and Moritani, T. (2004). Selective fatigue of fast motor units after electrically elicited muscle contractions. *Journal of Electromyography and Kinesiology*, 14:531–538.

[Harris and Wolpert, 1998] Harris, C. and Wolpert, D. (1998). Signal-dependent noise determines motor planning. *Nature*, 394(August):780–784.

[Hatze, 1977] Hatze, H. (1977). A myocybernetic control model of skeletal muscle. *Biological cybernetics*, 25(2):103–119.

[Hayashibe et al., 2010] Hayashibe, M., Benoussaad, M., Guiraud, D., Poignet, P., and Fattal, C. (2010). Nonlinear identification method corresponding to muscle property variation in FES - Experiments in paraplegic patients. In *2010 3rd IEEE RAS and EMBS International Conference on Biomedical Robotics and Biomechatronics, BioRob 2010*, pages 401–406.

[Hayashibe et al., 2008] Hayashibe, M., Poignet, P., Guiraud, D., and El Makssoud, H. (2008). Nonlinear identification of skeletal muscle dynamics with Sigma-Point Kalman Filter for model-based FES. In *Proceedings - IEEE International Conference on Robotics and Automation*, pages 2049–2054.

[Hayashibe and Shimoda, 2014] Hayashibe, M. and Shimoda, S. (2014). Synergetic motor control paradigm for optimizing energy efficiency of multijoint reaching via tacit learning. *Frontiers in computational neuroscience*, 8(February):21.

[Hayashibe et al., 2011a] Hayashibe, M., Venture, G., Ayusawa, K., and Nakamura, Y. (2011a). Muscle strength and Mass Distribution Identification toward subject-specific musculoskeletal modeling. In *In Proc. of the IEEE/RSJ International Conference on Intelligent Robots and Systems (IROS)*, pages 3701–3707, San Francisco, CA, USA.

[Hayashibe et al., 2011b] Hayashibe, M., Zhang, Q., Guiraud, D., and Fattal, C. (2011b). Evoked EMG-based torque prediction under muscle fatigue in implanted neural stimulation.

[Hayashibe et al., 2011c] Hayashibe, M., Zhang, Q., Guiraud, D., and Fattal, C. (2011c). Evoked EMG-based torque prediction under muscle fatigue in implanted neural stimulation. *Journal of Neural Engineering*, 8:064001.

[Heasman et al., 2000] Heasman, J. M., Scott, T. R. D., Vare, V. A., Flynn, R. Y., Gschwind, C. R., Middleton, J. W., and Butkowski, S. B. (2000). Detection of fatigue in the isometric electrical activation of paralyzed hand muscles of persons with tetraplegia. *IEEE Transactions on [see also IEEE Trans. on Neural Systems and Rehabilitation] Rehabilitation Engineering*, 8(3):286–296.

[Hill, 1938] Hill, A. V. (1938). The Heat of Shortening and the Dynamic Constants of Muscle.

[Holobar et al., 2009] Holobar, A., Farina, D., Gazzoni, M., Merletti, R., and Damjan, Z. (2009). Estimating motor unit discharge patterns from high-density surface electromyogram. *Clinical Neurophysiology*, 120:551–562.

[Huxley, 1957] Huxley, A. F. (1957). Muscle structure and theories of contraction. *Progress in Biophysics and Biophysical Chemistry*, 7:255–318.

[Ijspeert et al., 2007] Ijspeert, A. J., Crespi, A., Ryczko, D., and Cabelguen, J.-M. (2007). From swimming to walking with a salamander robot driven by a spinal cord model. *Science (New York, N.Y.)*, 315(5817):1416–1420.

[Izawa et al., 2008] Izawa, J., Rane, T., Donchin, O., and Shadmehr, R. (2008). Motor adaptation as a process of reoptimization. *The Journal of neuroscience : the official journal of the Society for Neuroscience*, 28:2883–2891.

[Jezernik et al., 2004] Jezernik, S., Wassink, G. V., and Keller, T. (2004). Sliding Mode Closed-Loop Control of FES: controlling the Shank Movement. *IEEE Transactions on Biomedical Engineering*, 51(2):263–272.

[Johnson and Fuglevand, 2011] Johnson, L. A. and Fuglevand, A. J. (2011). Mimicking muscle activity with electrical stimulation. *Journal of Neural Engineering*, 8:1–15.

[Julier and Uhlmann, 1997] Julier, S. and Uhlmann, J. (1997). A New Extension of the Kalman Filter to Nonlinear Systems. *Int Symp AerospaceDefense Sensing Simul and Controls*, 3(2):26.

[Julier and Uhlmann, 2004] Julier, S. J. and Uhlmann, J. K. (2004). Unscented filtering and nonlinear estimation. In *Proceedings of the IEEE*, volume 92, pages 401–422.

[Kajita et al., 2009] Kajita, S., Hirukawa, H., Harada, K., and Yokoi, K. (2009). *Introduction à la commande des robots humanoïdes*. Springer-Verlag France, Paris, France.

[Kamieth et al., 2010] Kamieth, F., Dähne, P., Wichert, R., Villalar, J. L., Jimenez-Mixco, V., Arca, A., and Arredondo, M. T. (2010). *Exploring the Potential of Virtual Reality for the Elderly and People with Disabilities*. InTech.

[Kawato, 1999] Kawato, M. (1999). Internal models for motor control and trajectory planning. *Current Opinion in Neurobiology*, 9(6):718–727.

[Kawato and Gomi, 1992] Kawato, M. and Gomi, H. (1992). A computational model of four regions of the cerebellum based on feedback-error learning. *Biological cybernetics*, 68(2):95–103.

[Kennedy et al., 2011] Kennedy, M. W., Schmiedeler, J. P., Crowell, C. R., Villano, M., Striegel, A. D., and Kuitse, J. (2011). Enhanced feedback in balance rehabilitation using the Nintendo Wii Balance Board. In *In Proc. of the IEEE International Conference on e-Health Networking, Applications and Services*, pages 162–168, Columbia, MO, USA.

[Kitazawa et al., 1998] Kitazawa, S., Kimura, T., and Yin, P. B. (1998). Cerebellar complex spikes encode both destinations and errors in arm movements. *Nature*, 392(6675):494–497.

[Kobetic et al., 1997] Kobetic, R., Triolo, R. J., and Marsolais, E. B. (1997). Muscle selection and walking performance of multichannel FES systems for ambulation in paraplegia. *IEEE Transactions on Rehabilitation Engineering*, 5(1):23–29.

[Kobetic et al., 1999] Kobetic, R., Triolo, R. J., Uhlir, J. P., Bieri, C., Wibowo, M., Polando, G., Marsolais, E. B., Davis J.A., J., Ferguson, K. A., and Sharma, M. (1999). Implanted functional electrical stimulation system for mobility in paraplegia: A follow-up case report. *IEEE Transactions on Rehabilitation Engineering*, 7(4):390–398.

[Lafond et al., 2004] Lafond, D., Duarte, M., and Prince, F. (2004). Comparison of three methods to estimate the center of mass during balance assessment. *Journal of Biomechanics*, 37(9):1421–1426.

[Lange et al., 2011] Lange, B., Chang, C.-Y., Suma, E., Newman, B., Rizzo, A. S., and Bolas, M. (2011). Development and evaluation of low cost game-based balance rehabilitation tool using the Microsoft Kinect sensor. In *In Proc. of the Annual International Conference IEEE Engineering in Medicine and Biology Society (IEEE/EMBC)*, pages 1831–1834, Boston, MA, USA.

[Langley and Mackintosh, 2007] Langley, F. A. and Mackintosh, S. F. H. (2007). Functional balance assessment of older community dwelling adults: a systematic review of the literature. *Internet Journal of Allied Health Sciences and Practice*, 5(4).

[Levin and Mizrahi, 1999] Levin, O. and Mizrahi, J. (1999). EMG and metabolite-based prediction of force in paralyzed quadriceps muscle under interrupted stimulation. *IEEE Transactions on Rehabilitation Engineering*, 7(3):301–314.

[Li et al., 2013a] Li, Z., Hayashibe, M., and Guiraud, D. (2013a). Inverse estimation of multiple muscle activations under isokinetic condition. In *Converging Clinical and Engineering Research on Neurorehabilitation*, pages 347–351. Springer.

[Li et al., 2013b] Li, Z., Hayashibe, M., and Guiraud, D. (2013b). Inverse estimation of muscle activations from joint torque via local multiple regression. In *Engineering in Medicine and Biology Society (EMBC), 2013 35th Annual International Conference of the IEEE*, pages 6639–6642. IEEE.

[Lim et al., 2000] Lim, J. K., Nam, M. H., and Khang, G. (2000). Model of Activation Dynamics for FES-Induced Muscle Fatigue. *Proceedings of the 22nd Annual International Conference of the IEEE Engineering in Medicine and Biology Society (EMBC00), Chicago, IL., USA*, pages 2251–2253.

[Ljung, 1999] Ljung, L. (1999). *System identification: theory for the user (2nd edition)*. New Jersey, USA: Prentice-Hall.

[Lyons et al., 2002] Lyons, G. M., Sinkjæ r, T., Burridge, J. H., and Wilcox, D. J. (2002). A Review of Portable FES-Based Neural Orthoses for the Correction of Drop Foot. *IEEE Transactions on Neural systems and Rehabilitation Engineering*, 10(4):260–279.

[Malek and Vaillancourt, 1995] Malek, F. and Vaillancourt, R. (1995). A Composite Polynomial Zerofinding Matrix Algorithm. *Computers Mathematics Application*, 30:37–47.

[Merletti et al., 2008] Merletti, R., Holobar, A., and Farina, D. (2008). Analysis of motor units with high-density surface electromyography. *Journal of Electromyography and Kinesiology*, 18:879–890.

[Mizrahi et al., 1994a] Mizrahi, J., Isakov, E., and Suzak, Z. (1994a). Myoelectric and force characteristics in transcutaneous isometric FES. *Basic and Applied Myology*, 4(2):147–154.

[Mizrahi et al., 1997a] Mizrahi, J., Levin, O., Aviram, A., Isakov, E., and Susak, Z. (1997a). Muscle fatigue in interrupted stimulation: effect of partial recovery on force and EMG dynamics. *Journal of Electromyography and Kinesiology*, 7(1):51–65.

[Mizrahi et al., 1994b] Mizrahi, J., Levy, M., Ring, H., Isakov, E., and Liberson, A. (1994b). EMG as an indicator of fatigue in isometrically FES-activated paralyzed muscles. *IEEE Transactions on Neural Systems and Rehabilitation*, 2(2):57–65.

[Mizrahi et al., 1997b] Mizrahi, J., Seelenfreund, D., Isakov, E., and Susak, Z. (1997b). Predicted and measured muscle forces after recoveries of differing durations following fatigue in functional electrical stimulation. *Artificial organs*, 21:236–239.

[Mooring et al., 1991] Mooring, B. W., Roth, Z. S., and Driels, M. R. (1991). *Fundamentals of Manipulator Calibration*. John Wiley & Sons, Inc, New York, USA.

[Nakamura, 1991] Nakamura, Y. (1991). *Advanced Robotics: Redundancy and Optimization*. Series in electrical and computer engineering. Addison-Wesley.

[Nakanishi et al., 2008] Nakanishi, J., Cory, R., Mistry, M., Peters, J., and Schaal, S. (2008). Operational Space Control: A Theoretical and Empirical Comparison. *The International Journal of Robotics Research*, 27(6):737–757.

[Nakanishi and Schaal, 2004] Nakanishi, J. and Schaal, S. (2004). Feedback error learning and nonlinear adaptive control. *Neural networks : the official journal of the International Neural Network Society*, 17(10):1453–1465.

[Nielsen et al., 1994] Nielsen, J., Sinkjæ r, T., Toft, E., and Kagamihara, Y. (1994). Segmental reflexes and ankle joint stiffness during co-contraction of antagonistic ankle muscles in man. *Experimental brain research*, 102(2):350–358.

[O'Keeffe et al., 2003] O'Keeffe, D. T., Donnelly, A. E., and Lyons, G. M. (2003). The development of a potential optimized stimulation intensity envelope for drop foot applications. *IEEE Transactions on Neural Systems and Rehabilitation Engineering*, 11(3):249–256.

[Painter et al., 2009] Painter, J. A., Elliott, S. J., and Hudson, S. (2009). Falls in community-dwelling adults aged 50 years and older: prevalence and contributing factors. *Journal of Allied Health*, 38(4):201–207.

[Patel et al., 2012] Patel, S., Park, H., Bonato, P., Chan, L., and Rodgers, M. (2012). A review of wearable sensors and systems with application in rehabilitation. *Journal of NeuroEngineering and Rehabilitation*, 9:21:1—-21:17.

[Pavlik,] Pavlik, R. WiiUse: Main page.

[Pelletier and Hicks, 2011] Pelletier, C. and Hicks, A. L. (2011). Muscle fatigue characteristics in paralyzed muscle after spinal cord injury. *Spinal Cord (2011)*, 49:125–130.

[Perreault et al., 2003] Perreault, E. J., Heckman, C. J., and Sandercock, T. G. (2003). Hill muscle model errors during movement are greatest within the physiologically relevant range of motor unit firing rates. *Journal of Biomechanics*, 36(2):211–218.

[Peters and Schaal, 2008] Peters, J. and Schaal, S. (2008). Learning to Control in Operational Space. *The International Journal of Robotics Research*, 27(2):197–212.

[Popović and Sinkjæ r, 2000] Popović, D. and Sinkjæ r, T. (2000). *Control of movement for the physically disabled (first edition)*. Springer.

[PrimeSense Inc.,] PrimeSense Inc. Open-sourse SDK for 3D sensors - OpenNI.

[Rendon et al., 2012] Rendon, A. A., Lohman, E. B., Thorpe, D., Johnson, E. G., Medina, E., and Bradley, B. (2012). The effect of virtual reality gaming on dynamic balance in older adults. *Age and Ageing*, 41(4):549–552.

[Riener, 1999] Riener, R. (1999). Model-based development of neuroprosthesis for paraplegic patients. *Philosophical transactions of the Royal Society of London. Series B, Biological sciences*, 354(1385):877–894.

[Riener et al., 2000] Riener, R., Ferrarin, M., Pavan, E. E., and Frigo, C. A. (2000). Patient-driven control of FES-supported standing up and sitting down: Experimental results. *IEEE Transactions on Rehabilitation Engineering*, 8(4):523–529.

[Riener and Quintern, 1997] Riener, R. and Quintern, J. (1997). A physiologically based model of muscle activation verified by electrical stimulation. In *Bioelectrochemistry and Bioenergetics*, volume 43, pages 257–264.

[Riener et al., 1996] Riener, R., Quintern, J., and Schmidt, G. (1996). Biomechanical model of the human knee evaluated by neuromuscular stimulation. *Journal of Biomechanics*, 29(9):1157–1167.

[Rissanen, 1978] Rissanen, J. (1978). Modeling by Shortest Data Description. *Automatica*, 14:465–471.

[Sardain and Bessonnet, 2004] Sardain, P. and Bessonnet, G. (2004). Forces Acting on a Biped Robot. Center of Pressure - Zero Moment Point. *IEEE Transactions on Systems, Man, and Cybernetics - Part A: Systems and Humans*, 34(5):630–637.

[Schepers et al., 2009] Schepers, H. M., van Asseldonk, E. H. F., Buurke, J. H., and Veltink, P. H. (2009). Ambulatory estimation of center of mass displacement during walking. *IEEE Transactions on Biomedical Engineering*, 56(4):1189–1195.

[Schweighofer et al., 1998] Schweighofer, N., Spoelstra, J., Arbib, M. A., and Kawato, M. (1998). Role of the cerebellum in reaching movements in humans. II. A neural model of the intermediate cerebellum. *European Journal of Neuroscience*, 10(1):95–105.

[Sennels et al., 1997] Sennels, S., Biering-sorensen, F., Andersen, O. T., and Hansen, S. D. (1997). Functional neuromuscular stimulation controlled by surface electromyographic signals produced by volitional activation of the same muscle: adaptive removal of the muscle response from the recorded {EMG}-signal. *IEEE Transactions on Rehabilitation Engineering*, 5(2):195–206.

[Shadmehr and Mussa-Ivaldi, 1994] Shadmehr, R. and Mussa-Ivaldi, F. A. (1994). Adaptive representation of dynamics during learning of a motor task. *Journal of Neuroscience*, 14(5 Pt 2):3208–3224.

[Shadmehr and Wise, 2005] Shadmehr, R. and Wise, S. P. (2005). *The computational neurobiology of reaching and pointing: a foundation for motor learning*. MIT Press.

[Shimoda and Kimura, 2010] Shimoda, S. and Kimura, H. (2010). Biomimetic Approach to Tacit Learning Based on Compound Control. *Systems, Man, and Cybernetics, Part B: Cybernetics, IEEE Transactions on*, 40(1):77–90.

[Shimoda et al., 2013] Shimoda, S., Yoshihara, Y., and Kimura, H. (2013). Adaptability of Tacit Learning in Bipedal Locomotion. In *Autonomous Mental Development, IEEE Transactions on*, volume 5, pages 152–161.

[Simon, 2006] Simon, D. (2006). *Optimal State Estimation: Kalman H Infinity, and Non Linear Approaches.* John Wiley & Sons, Inc.

[Sinkjæ r et al., 1993] Sinkjæ r, T., Toft, E., Larsen, K., and Andreassen, S. (1993). EMG-Torque dynamics at different contraction levels in human ankle muscles. *Journal of Electromyography and Kinesiology*, 3(2):67–77.

[Solomonow et al., 1995] Solomonow, M., Baratta, R. V., Zhou B.H., Bernardi, M., and Aciemo, S. (1995). ANALYSIS OF EMG CROSSTALK IN NEIGHBORING AND ANTAGONIST CAT MUSCLES. *Proceeding of the 17th Annual Conference of IEEE Engineering in Medicine and Biology Society (EMBC95), Montreal, Que., Canada*, 2:1353–1354.

[Song et al., 2004] Song, C. G., Kim, J. Y., and Kim, N. G. (2004). A New Postural Balance Control System for Rehabilitation Training Based on Virtual Cycling. *IEEE Transactions on Information Technology in Biomedicine*, 8(2):200–207.

[Stone and Skubic, 2011] Stone, E. E. and Skubic, M. (2011). Evaluation of an inexpensive depth camera for passive in-home fall risk assessment. In *In Proc. of the International Conference on Pervasive Computing Technologies for Healthcare (PervasiveHealth)*, pages 71–77, Dublin, Ireland.

[Tagliabue and McIntyre, 2014] Tagliabue, M. and McIntyre, J. (2014). A modular theory of multisensory integration for motor control. *Frontiers in computational neuroscience*, 8:1.

[Tepavac and Schwirtlich, 1997] Tepavac, D. and Schwirtlich, L. (1997). Detection and prediction of FES-induced fatigue. *Journal of Electromyography and Kinesiology*, 7(1):0–39.

[Todorov, 2004] Todorov, E. (2004). Optimality principles in sensorimotor control. *Nature neuroscience*, 7(9):907–15.

[Todorov and Jordan, 2002] Todorov, E. and Jordan, M. I. (2002). Optimal feedback control as a theory of motor coordination. *Nature neuroscience*, 5(11):1226–35.

[Toussaint et al., 2010] Toussaint, M., Andreuy, D., Fraisse, P., and Guiraudy, D. (2010). Wireless distributed architecture for therapeutic functional electrical Stimulation: a technology to design network-based muscle control. In *Engineering in Medicine and Biology Society (EMBC), 2010 Annual International Conference of the IEEE*, pages 6218–6221. IEEE.

[Uno et al., 1989] Uno, Y., Kawato, M., and Suzuki, R. (1989). Formation and control of optimal trajectory in human multijoint arm movement. Minimum torque-change model. *Biological cybernetics*, 61:89–101.

[van der Merwe and Wan, 2003] van der Merwe, R. and Wan, E. (2003). Gaussian mixture sigma-point particle filters for sequential probabilistic inference in dynamic state-space models. *2003 IEEE International Conference on Acoustics, Speech, and Signal Processing, 2003. Proceedings. (ICASSP '03).*, 6.

[Venture et al., 2009] Venture, G., Ayusawa, K., and Nakamura, Y. (2009). Real-time identification and visualization of human segment parameters. In *In Proc. of the Annual International Conference IEEE Engineering in Medicine and Biology Society (IEEE/EMBC)*, pages 3983–3986, Minneapolis, MN, USA.

[Vukobratovic and Borovac, 2004] Vukobratovic, M. and Borovac, B. (2004). Zero-moment point - thirty five years of its life. *International Journal of Humanoid Robotics*, 1(1):157–173.

[Waltz, 2013] Waltz, E. (2013). An electrifying awakening electrical stimulation of the spinal cord could let paralyzed people move again. *IEEE Spectrum*, 50(11):46–52.

[Winter, 1990] Winter, D. a. (1990). Biomechanics and Motor Control of Human Movement. *Processing*, 2nd(Book, Whole):277.

[Wu et al., 2002] Wu, H.-C., Young, S.-T., and Kuo, T.-S. (2002). A versatile multichannel direct-synthesized electrical stimulator for FES applications. *Instrumentation and Measurement, IEEE Transactions on*, 51(1):2–9.

[Zahalak, 1981] Zahalak, G. I. (1981). A Distribution-Moment Approximation for KineticTheories of Muscular Contraction. *MATHEMATICAL BIOSCIENCES*, 55(1):89–114.

[Zajac, 1989] Zajac, F. E. (1989). Muscle and tendon: properties, models, scaling, and application to biomechanics and motor control. *Critical reviews in biomedical engineering*, 17(4):359–411.

[Zhu et al., 1991] Zhu, Q. M., Warwick, K., and Douce, J. L. (1991). Adaptive general predictive controller for nonlinear systems. *IEEE proceedings-D*, 138(1):33–40.

[Ziai and Menon, 2011] Ziai, A. and Menon, C. (2011). Comparison of regression models for estimation of isometric wrist joint torques using surface electromyography. *Journal of NeuroEngineering and Rehabilitation*, 8(1):56.